WARSAW UNIVERSITY OF TECHNOLOGY

DISCIPLINE OF SCIENCE: PHYSICAL SCIENCE
FIELD OF SCIENCE: NATURAL SCIENCE

Ph.D Thesis

Le Xuan The Tai, Ms.c

Controlling energy transfer in high-index contrast multicore soft-glass fibers

Supervisor
prof dr hab. Marek Trippenbach

Additional supervisor
dr. Nguyen Viet Hung

Warsaw, October 2023

Acknowledgments

I would like to express my gratitude to everyone who contributed to the conclusion of my Ph.D. studies and the realization of this dissertation. First, I would like to express my sincere gratitude to my supervisor, prof. dr hab. Marek Trippenbach, for patient guidance and many insights during my PhD studies and preparation of this thesis. I would like to thank him for his constant support, motivation, and fruitful advice.

I am particularly thankful to my assistant supervisor, dr Nguyen Viet Hung, whose constant assistance was absolutely fundamental for the realization of this work. I greatly appreciate the knowledge and skills that he taught me about numerical methods in the early years of my Ph.D. study.

My gratitude extends to several senior scientists from around the world, including Professor Boris Malomed (Israel), Dr. Ignác Bugár (Austria/Slovakia), Professor Dr. Hab. Inż. Ryszard Buczyński and Dr. Mattia Longobucco (Singapore), and their respective research groups. Their scientific expertise and mentorship significantly expanded my knowledge in my field of interest and beyond.

I would like to express my gratitude also to prof. dr hab. Cao Long Van for inspiring my interest in science and for helping to arrange the meeting with my supervisor, which made this Ph.D. program possible.

I also wish to express my thanks to my parents, Le Xuan Hoang and Le Thi Thuy Yen, for their unwavering support throughout my Ph.D. journey, even from afar, and for instilling in me the importance of upholding our family traditions.

This dissertation has been supported by the TEAM NET program of the Foundation for Polish Science co-financed by the European Union under the European Regional Development Fund, project POIR.04.04.00-00-1644/18, and by the Vietnam Ministry of Education and Training (MOET) under Grant Number B2022-BKA-14.

Abstract

The research program contained in the Ph. D thesis refers to the all-optical couplers realized in the two-core high-index contrast soft glass fibers. It is directly related to the experimental program focused on effective switching performance between cores even if cores are asymmetrical, due to the difference in effective refractive index. Three different experiments were performed, in the in-house manufactured soft-glass waveguides. In the first two, there were only signal pulses propagated, first in symmetrical dual-core fiber and then in asymmetrical dual-core fiber. The outcomes of the experiment are considered with different signal pulse energy, width, and in the case of asymmetrical fiber choice of the excited core. In the last one, to compensate for refractive index asymmetry, there was a strong control pulse added in one of the channels. Effects of the fiber length, control pulse energy, and time delay between the control and signal pulses were under investigation and used to optimize the switching performance. We used the simple model based on coupled nonlinear Schrödinger equations and obtained fair agreement with experimental results. Using this model, we could explain the effect of asymmetry and how this asymmetry can be compensated by the reference pulse. In the last part, we propose an experimental study for a PT-symmetric photonic crystal fiber (PCF) that we designed and analyzed using the same straightforward model of coupled nonlinear Schrödinger equations.

Keywords— All-optical couplers, soft-glass fiber, dual-core fiber, coupled nonlinear Schrodinger equations, PT-symmetric photonic crystal fiber, switching.

Streszczenie

Kontrola transferu energii w wielordzeniowych włóknach z miękkiego szkła o wysokim kontraście wskaźnika załamania

Program badawczy zawarty w rozprawie doktorskiej odnosi się do całkowicie optycznych sprzęgaczy zrealizowanych w dwurdzeniowych włóknach o wysokim kontraście wskaźników załamania w miękkim szkle. Bezpośrednio wiąże się z programem eksperymentalnym skupionym na efektywności przełączania między rdzeniami, nawet jeśli rdzenie są niesymetryczne z powodu różnicy w efektywnym współczynniku załamania. Przeprowadzono trzy różne eksperymenty, w włóknach o miękkim szkle wytwarzanych w naszym laboratorium. W dwóch pierwszych przesyłano tylko impulsy sygnałowe, najpierw w symetrycznym dwurdzeniowym włóknie, a następnie w niesymetrycznym dwurdzeniowym włóknie. Wyniki eksperymentów były analizowane pod kątem różnej energii impulsów sygnałowych, ich szerokości i w przypadku włókna niesymetrycznego, wyboru pobudzonego rdzenia. W trzecim eksperymencie, w celu zrównoważenia nierówności współczynnika załamania, wprowadzono silny impuls kontrolny do jednego z kanałów. Badano wpływ długości włókna, energii impulsu kontrolnego i opóźnienia między impulsami kontrolnym a sygnałowymi w celu zoptymalizowania efektywności przełączania. Wykorzystano prosty model oparty na sprzężonych równaniach nieliniowych Schrödingera i uzyskano zgodność z wynikami eksperymentalnymi. Dzięki temu modelowi mogliśmy wyjaśnić efekt asymetrii i sposób, w jaki można ją zrekompensować przy użyciu impulsu referencyjnego. W ostatniej części proponujemy badania eksperymentalne dla fotonicznego włókna kryształowego typu swiatlowod fotoniczny o symetrii PT (PCF), które zaprojektowaliśmy i przeanalizowaliśmy, korzystając z tego samego prostego modelu opartego na sprzężonych równaniach nieliniowych Schrödingera.

Keywords— Sprzęgacze calkowicie optyczne, światłowód ze szkiel miekkich, swiatlowody dwurdzeniowe, sprzężenie nieliniowe rownanie Schrödingera, światłowód fotoniczny o symetrii PT, przełączanie

Contents

Introduction

Numerous contemporary technologies, such as those in telecommunications, laser technology, analytical instruments, and imaging systems, find their roots in the principles of nonlinear optics. As a result, the study of optical nonlinear phenomena remains a prominent area of investigation in the field of physics. Among these phenomena, the examination of third-order nonlinearity, described by Nonlinear Schrödinger Equations (NLSE), is a particularly well-explored topic. In certain situations, nonlinear materials allow different components of a system to interact, with the most basic form, involving just two components, known as a nonlinear directional coupler. A notable example of this setup is the dual-core fiber (DCF), which has the potential to serve as an all-optical signal switching device. The analysis of DCF behavior primarily relies on Coupled Nonlinear Schrödinger Equations (CNLSE). While CNLSE is widely applicable, this thesis focuses on a detailed investigation of how nonlinearity, coupling strength, and core dissimilarity affect the dynamics of soliton-like pulse propagation within DCF.

The concept of using dual-core fibers (DCFs) for all-optical switching was initially introduced in theoretical discussions during the early 1980s. Since then, substantial efforts have been dedicated to comprehending and optimizing the performance of these devices. However, achieving straightforward all-optical switching has remained a significant challenge in the field of nonlinear fiber optics. The primary challenges in achieving ultrafast nonlinear switching in traditional nonlinear couplers arise from the high power levels required for signal redirection and the resulting disruption in the temporal domain. To address these challenges, a novel approach was proposed, advocating the use of DCFs made of highly nonlinear lead silicate glass, PBG-08. This study predominantly focuses on assessing the performance of a highly nonlinear DCF configuration with two cores composed of soft glass materials. Incorporating PBG-08 glass introduces a significant degree of nonlinearity, replacing the complex air–glass PCF structure with low-index glass. The substantial difference in refractive index between the core and cladding in this setup underscores the efficiency of the proposed switching mechanism

This thesis contains a comprehensive review of nonlinear pulse propagation physics, propagation in a photonic crystal, and other structured fibers. We describe all three experiments in separate chapters (Each of them was a subject of separate publication). Furthermore, we employ numerical solutions to draw a comparative analysis, contrasting our model's predictions based on CNLSE with the actual experimental outcomes.

In the opening chapter titled "Linear and Nonlinear Light Transmission in Waveguides," we revisit the foundational concepts of light propagation within linear and nonlinear mediums, with a particular focus on optical fibers. We establish the propagation equation from its fundamental principles, taking into account significant nonlinear phenomena and providing brief explanations of their underlying mechanisms. Subsequently, we deduce the coupled mode equations for optical couplers by introducing the concept of a coupling parameter. We explore various linearized scenarios of these coupled mode equations and engage in a discussion of their implications, aiming to gain a fundamental grasp of how each parameter influences pulse propagation within the optical fiber.

In the second chapter called "Optical switching in symmetrical dual-core highly nonlinear optical fibers", we investigate the switching mechanism (optical coupler) in the dual-core photonic-crystal fiber. We focus the input beam on one of the channels, to study the stability of the transmission and identify a threshold between switching and self-trapping in either channel. A model that includes the two coupled channels with intrinsic dispersion and nonlinearity provides surprisingly good agreement with the experimental findings.

In the third chapter called "Self-trapping and switching in asymmetrical dual-core highly nonlinear fibers", we investigate experimentally and theoretically the effects of the inter-core propagation mismatch on nonlinear switching in dual-core high-index-contrast soft-glass optical fibers. Incident femtosecond pulses are fed into a single ("straight") core, to identify transitions between different dynamical regimes, viz., inter-core oscillations, self-trapping in the cross core, and retaining the pulse in the straight core. The transitions that have solitonic character, are controlled by the pulse's energy. A model based on the system of coupled nonlinear Schrodinger equations reveals the effect of the mismatch parameter and pulse duration on the diagram of the various energy-dependent dynamical regimes. Optimal values of the mismatch and pulse width, which ensure stable performance of the nonlinear switching, are identified.

In the fourth chapter called "Control of dual-wavelength switching in asymmetric dual-core fiber", we present a complex experimental and theoretical analysis of dual-wavelength switching of 1560 nm, 75 fs pulses (labeled as signal) driven by 1030 nm, 270 fs pulses (labeled as control) using a dual-core fiber. The fiber was specially developed for this aim having high refractive index contrast and moderate asymmetry of the phase and group refraction index comparing the two guiding channels. The experimental work involved the study of effects on the switching performance as fiber length, control pulse energy, and time delay between the control and signal pulses. We demonstrated the highest switching contrast of 41.6 dB at 14 mm fiber length with a broadband character in the 1450-1650 nm spectral range. A numerical model of three coupled pulse propagation equations was used to enlighten the physical processes behind the advantageous switching performance. The theoretical results revealed the role of both the phase and group refractive index asymmetry and confirmed our preliminary switching concept: nonlinear balancing of dual-core asymmetry. Furthermore, the numerical outcomes brought comparable dependence of the switching extinction ratio on the pulse energy and delay. The most important advantage of the presented approach is the moderate nonlinear interaction between the control and signal pulses transforming the signal field slightly. The numerical results also support this concept predicting moderate transformations of the signal spectra and unveiling its non-trivial dependence on the pulse delay.

The fifth chapter is a proposal for the experiment with additional gain (generated by the additional external pulse) to study the propagation in the vicinity of the exceptional point (as in so-called PT-symmetric systems). In this context, we investigate the properties of a soft glass dual-core fiber for application in multicore waveguiding with balanced gain and loss. Its base material is a phosphate glass in a P2O5-Al2O3-Yb2O3-BaO-ZnO-MgO-Na2O oxide system. The separated gain and loss channels can realized with two cores with ytterbium and copper doping of the base phosphate glass. We perform a feasibility study of such an experimental realization, including the possible use of the exceptional point for stabilization of the pulse propagation.

The Appendix presents the Fast Fourier Transform (FFT) algorithm, which serves as our primary tool for addressing the Nonlinear Schrödinger Equations (NLSEs) to analyze pulse propagation. Furthermore, we look into the numerical stability of our computational methods and determine the criteria for achieving precision in simulations.

Chapter 1

Linear and nonlinear light propagation in waveguides

1.1 Fundamentals of nonlinear optical processes

The nonlinear responses of the material of optical fibers create new dynamics of the optical fields propagated in them. Therefore, in this section, we are going to review several important nonlinear effects in nonrestrictive media, without sacrificing crucial characteristics.

1.1.1 The linear wave equation for the slowly varying envelope

Maxwell's equations in an isotropic linear medium are written as:

$$\nabla \times \mathbf{H}(\mathbf{r}, t) = \frac{\partial}{\partial t}\mathbf{D}(\mathbf{r}, t), \tag{1.1a}$$

$$\nabla \times \mathbf{E}(\mathbf{r}, t) = -\frac{\partial}{\partial t}\mathbf{B}(\mathbf{r}, t), \tag{1.1b}$$

$$\nabla \cdot \mathbf{B}(\mathbf{r}, t) = 0, \tag{1.1c}$$

$$\nabla \cdot \mathbf{D}(\mathbf{r}, t) = 0, \tag{1.1d}$$

where **E**, **H** are electric and magnetic field, respectively, and **D** and **B** are corresponding electric and magnetic flux densities. The relations of flux densities **B** and**D** with electric and magnetic field $\mathbf{E}$ and $\mathbf{H}$ are given by:

$$\mathbf{B} = \mu_0 \mathbf{H}, \tag{1.2a}$$

$$\mathbf{D} = \varepsilon_0 \varepsilon \mathbf{E} = \varepsilon_0 \mathbf{E} + \mathbf{P}. \tag{1.2b}$$

where ε_0 is the vacuum permittivity, μ_0 is the vacuum permeability, and $\mathbf{P}$ is the induced electric polarization. For nondispersive medium, induced electric $\mathbf{P} = \varepsilon_0 \chi \mathbf{E}$, where χ is constant

$$\mathbf{D} = \varepsilon_0 \mathbf{E} + \mathbf{P} = \varepsilon_0 (1 + \chi) \mathbf{E} \tag{1.3}$$

We perform curl in both sides of equation (1.1b), use equation (1.2a) and relation $\boldsymbol{\nabla} \times \boldsymbol{\nabla} \times \mathbf{E} = \boldsymbol{\nabla} \cdot (\boldsymbol{\nabla} \cdot \mathbf{E}) - \Delta \mathbf{E}$, in the scalar approximation $\mathbf{E} = E \hat{\mathbf{e}}_x$, $\boldsymbol{\nabla} \cdot \mathbf{E} = 0$, to obtain the wave equation

$$\Delta \mathbf{E} = \frac{1}{c^2} \frac{\partial^2}{\partial t^2} \mathbf{E} + \mu_0 \frac{\partial^2}{\partial t^2} \mathbf{P} \,. \tag{1.4}$$

Here we used the relation $\mu_0 \varepsilon_0 = 1/c^2$ where c is the speed of light. For the dispersive medium χ is functional. The polarization is given by convolution of functions χ and $\mathbf{E}$ as follow:

$$\mathbf{P}_L(\mathbf{r}, t) = \int_{-\infty}^{t} \mathrm{d}t' \varepsilon_0 \chi(t - t') \mathbf{E}(\mathbf{r}, t') \,. \tag{1.5}$$

We see that polarization in a given time t can depend on the intensity of the electric field in moments t' earlier than t. If we assume that $\chi(s) = 0$ for$s < 0$, then the upper integral limit can be prolonged to infinity.

Instead of using convolution (1.5), we transform the problem to Fourier space, by defining the Fourier transform and its inverse for electric field $\mathbf{E}(t)$ as

$$\tilde{\mathbf{E}}(\omega) = \int_{-\infty}^{+\infty} \mathrm{e}^{i\omega t} \mathbf{E}(t) \,, \quad \mathbf{E}(t) = \frac{1}{2\pi} \int_{-\infty}^{+\infty} \mathrm{e}^{-i\omega t} \tilde{\mathbf{E}}(\omega) \mathrm{d}\omega \,. \tag{1.6}$$

In a similar way we define transforms for functions $\mathbf{P}$, $\mathbf{D}$, and χ. It follows from (1.5) that

$$\tilde{\mathbf{P}}(\omega) = \varepsilon_0 \tilde{\chi}(\omega) \tilde{\mathbf{E}}(\omega) = \varepsilon_0 \left(\varepsilon_r(\omega) - 1 \right) \tilde{\mathbf{E}}(\omega) \,, \tag{1.7}$$

where we define the functional $\varepsilon_r = 1 + \chi$. One can analogically define the transformation in space-time

$$\tilde{\mathbf{E}}(\mathbf{k},\omega) = \int_{-\infty}^{+\infty} \mathrm{d}t \int_{\mathbb{R}^3} \mathrm{d}^3\mathbf{r}\ \mathrm{e}^{-i\mathbf{kr}+i\omega t}\mathbf{E}(\mathbf{r},t)\,. \tag{1.8}$$

We consider now the case of plane wave

$$\mathbf{E}(\mathbf{r},t) = E_0 e^{i(k_0 z-\omega_0 t)} \tag{1.9}$$

It follows from (1.4) and (1.7) that electric field satisfies the equation

$$\Delta\mathbf{E} = \frac{1}{c^2}\varepsilon_r(\omega_0)\frac{\partial^2\mathbf{E}}{\partial t^2} = \left(\frac{n(\omega_0)}{c}\right)^2\frac{\partial^2\mathbf{E}}{\partial t^2}\,, \tag{1.10}$$

where $n(\omega_0) = \sqrt{\varepsilon_r(\omega_0)}$ is refractive index of the medium at frequency ω_0. Substituting (1.9) and replace differentiation with respect to the variable z with the multiplication by ik, we obtain the relation between $k = |\mathbf{k}|$ and ω i.e. the dispersion relation

$$k(\omega) = \frac{n(\omega)\omega}{c}\,. \tag{1.11}$$

We assume that propagating light waves have a sufficiently narrow spectrum and one propagation direction (for example a laser pulse moving in a given direction). This means that one can choose a central frequency ω_0 and wave vector $\mathbf{k}_0$ in such a way that the function $\tilde{\mathbf{E}}(\mathbf{k},\omega)$ is negligibly small outside vicinity of this point. Then electric field could be presented as a product of the plane wave and the pulse envelope $\mathbf{A}(\mathbf{r},t)$

$$\mathbf{E}(\mathbf{r},t) = \mathbf{A}(\mathbf{r},t)\mathrm{e}^{i(k_0 z-\omega_0 t)}\,, \tag{1.12}$$

where the z axis is chosen such that $\mathbf{k}_0 = k_0\hat{\mathbf{e}}_z$. In the function $\mathbf{A}$ the oscillations with high frequency ω_0 and in the space k_0 have been separated, therefore it is named the Slow-Varying Envelope. From (1.8) we have

$$\tilde{\mathbf{E}}(\mathbf{k},\omega) = \int \mathrm{d}t \int \mathrm{d}^3\mathbf{r}\ \mathrm{e}^{-i(\mathbf{k}-\mathbf{k}_0)\mathbf{r}+i(\omega-\omega_0)t}\mathbf{A}(\mathbf{r},t) = \tilde{\mathbf{A}}(\mathbf{k}-\mathbf{k}_0,\omega-\omega_0)\,. \tag{1.13}$$

In our approximation, every solution of the system of Maxwell's equations is a superposition of plane waves and every plane wave satisfies its dispersion relation. Thus, for a given pair $(\mathbf{k},\omega)$ function $\tilde{\mathbf{E}}(\mathbf{k},\omega)$ does not vanish only for $|\mathbf{k}| = k(\omega)$. One can write this fact as the following equation

$$\left[\mathbf{k}^2 - k^2(\omega)\right]\tilde{\mathbf{E}}(\mathbf{k},\omega) = 0\,, \tag{1.14}$$

where $k(\omega)$ is the function of ω and *does not depend* on $\mathbf{k}$ for isotropic media. Of course this relation is satisfied also if we redefine $\mathbf{k}$ and ω as follows

$$\left[(\mathbf{k}+\mathbf{k}_0)^2 - k^2(\omega+\omega_0)\right]\tilde{\mathbf{E}}(\mathbf{k}+\mathbf{k}_0,\omega+\omega_0) = 0\,. \tag{1.15}$$

In the further $\mathbf{k}$ and ω are small in comparison with $\mathbf{k}_0$ and ω_0, by our assumptions that we consider only small vicinity of the point $(\mathbf{k}_0,\omega_0)$. Further calculations will be performed with accuracy to the second order of these variables. Using (1.13) we obtain

$$\left[(\mathbf{k}+\mathbf{k}_0)^2 - k^2(\omega+\omega_0)\right]\tilde{\mathbf{A}}(\mathbf{k},\omega) = 0\,. \tag{1.16}$$

We expand now the dispersion relation into the Taylor series around ω_0

$$k(\omega_0+\omega) = k(\omega_0) + \frac{1}{1!}\beta_1\omega + \frac{1}{2!}\beta_2\omega^2 + \dots\,, \tag{1.17}$$

where we assume that ω_0 is chosen in such a way that $k_0 = k(\omega_0)$. Substituting this expansion to the equation (1.16)

$$\left[k_x^2 + k_y^2 + k_z^2 + 2k_0k_z + k_0^2 - \Big(\underbrace{k_0 + \frac{1}{1!}\beta_1\omega + \frac{1}{2!}\beta_2\omega^2 + \dots}_{D}\Big)^2\right]\tilde{\mathbf{A}}(\mathbf{k},\omega) = 0\,, \tag{1.18}$$

$$\Bigg(k_z^2 + 2k_0k_z + \underbrace{k_x^2 + k_y^2 + k_0^2 - D^2}_{L}\Bigg)\tilde{\mathbf{A}}(\mathbf{k},\omega) = 0\,. \tag{1.19}$$

We see that $D \approx k_0$, so $L \ll k_0$. For every point $(\mathbf{k},\omega)$ which $\tilde{\mathbf{A}}(\mathbf{k},\omega) \neq 0$ the expression inside the parenthesizes is equal to zeros. This approximation gives us a quadratic equation for

k_z. Thus we have two solutions, and we choose one of them by assumptions $k_z \ll k_0$

$$\begin{aligned}
k_z &= -k_0 + s\sqrt{k_0^2 - L} = k_0\left(\sqrt{1 - L/k_0} - 1\right) \simeq -\frac{1}{2k_0}L - \frac{1}{8k_0^2}L^2 = \\
&= \frac{1}{2k_0}\left[k_x^2 + k_y^2 + k_0^2 - \left(k_0 + \beta_1\omega + \frac{\beta_2}{2}\omega^2 + \ldots\right)^2\right] - \frac{1}{8k_0^2}\left[\ldots\right]^2 = \\
&= \frac{1}{2k_0}\left[k_x^2 + k_y^2 - 2\beta_1 k_0\omega - \beta_2 k_0\omega^2 - \beta_1^2\omega^2 + \ldots\right] - \frac{1}{8k_0^2}\left[\ldots\right]^2 = \\
&= -\frac{k_x^2}{2k_0} - \frac{k_y^2}{2k_0} + \beta_1\omega + \frac{\beta_2}{2}\omega^2 + O\left[(k_x, k_y, \omega)^3\right] , \qquad (1.20)
\end{aligned}$$

Then we have

$$\left(k_z + \frac{k_x^2}{2k_0} + \frac{k_y^2}{2k_0} - \beta_1\omega - \frac{\beta_2}{2}\omega^2\right)\tilde{\mathbf{A}}(\mathbf{k}, \omega) = 0\,, \qquad (1.21)$$

We transform the resulting equation to the real space to obtain a linear propagation equation for slowly varying envelope as:

$$\frac{\partial \mathbf{A}}{\partial z} = \frac{i}{2k_0}\Delta_\perp \mathbf{A} - \beta_1\frac{\partial \mathbf{A}}{\partial t} - i\frac{\beta_2}{2}\frac{\partial^2 \mathbf{A}}{\partial t^2}\,, \qquad (1.22)$$

where $\Delta_\perp = \frac{\partial^2}{\partial x^2} + \frac{\partial^2}{\partial y^2}$.

1.1.2 Nonlinear polarization of optical media

In equation (1.5), only the first term in an expansion of the polarization as a function of the electric field is mentioned. As the field strength $\tilde{\mathbf{E}}(\omega, \mathbf{k})$ increases, nonlinear contributions of electric field strength to the polarization can become important. Thus, the polarization of the optical medium must consist nonlinear part

$$\begin{aligned}
\mathbf{P}(\mathbf{r}, t) &= \mathbf{P}_L(\mathbf{r}, t) + \mathbf{P}_{NL}(\mathbf{r}, t), \qquad (1.23) \\
\mathbf{P}(\mathbf{r}, \omega) &= \mathbf{P}_L(\mathbf{r}, \omega) + \mathbf{P}_{NL}(\mathbf{r}, \omega). \qquad (1.24)
\end{aligned}$$

Here, $\mathbf{P}_L$ and $\mathbf{P}_{NL}$ are the linear and nonlinear parts of the polarization. The wave equation (1.4) then must consider the nonlinear part of polarization then become:

$$\Delta \mathbf{E} = \left(\frac{n(\omega)}{c}\right)^2 \frac{\partial^2}{\partial t^2}\mathbf{E} + \mu_0\frac{\partial^2}{\partial t^2}\mathbf{P}_{NL}, \qquad (1.25)$$

or

$$\Delta\mathbf{E}(\omega,\mathbf{r}) = \frac{\omega^2\varepsilon_r}{c^2}\mathbf{E}(\omega,\mathbf{r}) + \mu_0\omega^2\mathbf{P}_{NL}(\omega,\mathbf{r}). \tag{1.26}$$

The nonlinear polarization is given by

$$\begin{aligned}\mathbf{P}_{NL}(\mathbf{r},t) &= \int_{-\infty}^{t}\int_{-\infty}^{t}\chi^{(2)}(t-t_1,t-t_2):\mathbf{E}(t_1)\mathbf{E}(t_2)dt_1dt_2 \\ &+ \int_{-\infty}^{t}\int_{-\infty}^{t}\int_{-\infty}^{t}\chi^{(3)}(t-t_1,t-t_2,t-t_3) \\ &\vdots\ \mathbf{E}(t_1)\mathbf{E}(t_2)\mathbf{E}(t_3)dt_1dt_2dt_3 + ..., \end{aligned} \tag{1.27}$$

where $\chi^{(2)}$ and $\chi^{(3)}$ are the second and third-order nonlinear susceptibilities. We take the Fourier transform of (1.27)

$$\begin{aligned}\mathbf{P}_{NL}(\omega,\mathbf{k}) &= \chi^{(2)}(\omega,\mathbf{k};\omega_i,\mathbf{k}_i,\omega_j,\mathbf{k}_j)\mathbf{E}(\omega_i,\mathbf{k}_i)\mathbf{E}(\omega_j,\mathbf{k}_j) \\ &+ \chi^{(3)}(\omega,\mathbf{k};\omega_i,\mathbf{k}_i,\omega_j,\mathbf{k}_j,\omega_l,\mathbf{k}_l) \\ &\times \mathbf{E}(\omega_i,\mathbf{k}_i)\mathbf{E}(\omega_j,\mathbf{k}_j)\mathbf{E}(\omega_l,\mathbf{k}_l) + ... \end{aligned} \tag{1.28}$$

where $\chi^{(2)}(\omega,\mathbf{k};\omega_i,\mathbf{k}_i,\omega_j,\mathbf{k}_j)$ and $\chi^{(3)}(\omega,\mathbf{k};\omega_i,\mathbf{k}_i,\omega_j,\mathbf{k}_j,\omega_l,\mathbf{k}_l))$ are the second and third order nonlinear susceptibilities, respectively.

The second-order nonlinear polarization gives rise to three-wave mixing processes. In particular, if $\omega_i = \omega_j$ in the second-order polarization, the second-order nonlinear polarization describes second-harmonic generation. For SHG, we could have $\mathbf{k}_1 = \mathbf{k}_2$, or $\mathbf{k}_1 \neq \mathbf{k}_2$, depending upon whether the momenta of the two destroyed photons are the same (e.g. the two photons are from the same beam) or not (two different beams entering the crystal in different directions). In the more general case, where $\omega_i \neq \omega_j$, the second order nonlinear polarization can describe SFG $\omega = \omega_i + \omega_j$, $\mathbf{k} = \mathbf{k}_i + \mathbf{k}_j$ or DFG $\omega = \omega_i - \omega_j$, $\mathbf{k} = \mathbf{k}_i - \mathbf{k}_j$.

The third-order nonlinear polarization is responsible for the four-wave mixing process (FWM). For the particular case, where $\omega_i = \omega_j = \omega_l$, a photon with $\omega = 3\omega_i$ and $\mathbf{k} = \mathbf{k}_i + \mathbf{k}_j + \mathbf{k}_l$ is generated then the process corresponds to third harmonic generation. More specific FWM process related to third third-order nonlinear polarization, requiring $\omega_i = \omega_j = \omega_l$ and $\mathbf{k}_i = \mathbf{k}_j = \mathbf{k}_l$ generates a photon with frequency $\omega = \omega_i - \omega_j + \omega_l$ and wave number $\mathbf{k} = \mathbf{k}_i - \mathbf{k}_j + \mathbf{k}_l$. Such processes are so-called self-focusing and self-phase modulation. These and other basic nonlinear-optical processes will be considered in greater detail in the following sections.

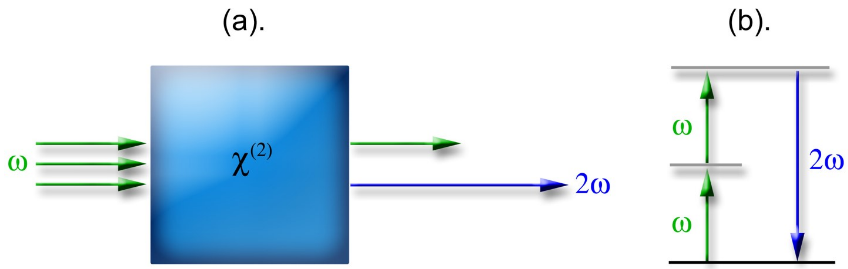

Fig. 1.1: *(a) Schematic diagram of SHG. (b) Energy level scheme of SHG process.*

1.1.3 Second order Processes

Second-harmonic generation can be visualized by considering the interaction in terms of the exchange of photons between the various frequency components of the field. In this case, the process of SHG occurs via multiple steps. A schematic energy-level diagram describing SHG is shown in Fig. 1.1. In the first step, one photon of frequency ω is annihilated while a molecule of the medium leaves its initial state to an intermediate state. In the second step, there is the annihilation of another photon of frequency ω while the excited molecule jumps to another intermediate state. In the final step, this excited molecule returns to its initial state while creating a new photon of frequency 2ω. Since the molecule stays in each intermediate state for an extremely short time, the three steps mentioned above occur instantaneously and simultaneously. We can obtain the analytic solution of SHG by using the semi-classical description of the optical field. Assuming both the incident fundamental field $E(\omega)$ and the frequency-doubled field $E(2\omega)$ are linearly-polarized monochromatic plane waves propagating along z-axis and can be described as

$$\mathbf{E}_1(\omega) = \mathbf{e}_1 A_1(z) e^{ik_1 z}, \tag{1.29}$$

$$\mathbf{E}_2(2\omega) = \mathbf{e}_2 A_2(z) e^{ik_2 z}. \tag{1.30}$$

Here, $A_1(z)$ and $A_2(z)$ are the amplitude functions, $\mathbf{e}_1$ and $\mathbf{e}_2$ are the unit vectors along the light polarization direction, and k_2 and k_2 are the absolute values of wavevectors for these two waves, respectively. Thus, the polarization of two waves should be

$$\begin{aligned} \mathbf{P}^{(2)}(\omega) &= \varepsilon_0 \chi^{(2)}(2\omega, -\omega)\mathbf{E}_2\mathbf{E}_1^* \\ &= \varepsilon_0 \chi^{(2)}(2\omega, -\omega)\mathbf{e}_1\mathbf{e}_2 A_2(z) A_1^*(z) e^{i(\mathbf{k}_2 - k_1)z}, \end{aligned} \tag{1.31}$$

$$\mathbf{P}^{(2)}(2\omega) = \varepsilon_0 \chi^{(2)}(\omega\omega)\mathbf{E}_1\mathbf{E}_1 = \varepsilon_0 \chi^{(2)}(\omega, \omega)\mathbf{e}_1\mathbf{e}_1 A_1^2(z) e^{2ik_1 z}. \tag{1.32}$$

We can now substitute the electric fields in terms of the slowly-varying envelope using equations (1.29) and (1.30) into (1.26). We then get the following identities

$$\Delta \mathbf{E} = (k^2 + 2i\mathbf{k} \cdot \nabla + \Delta)A(z)e^{i\mathbf{kz}}.$$

Because A is slowly varying in space and time $\Delta A \gg \mathbf{k} \cdot \nabla A$, we can drop the Δ term. Then, we use the dispersive relation (1.11): $k^2 = n^2\omega^2/c^2 = \varepsilon_r \omega^2/c^2$, to obtain:

$$\frac{\partial A_1}{\partial z} = i\frac{\mu_0 \omega^2}{2k_1}\mathbf{e}_1 \mathbf{P}^{(2)}(\omega)e^{-ik_1 z}, \tag{1.33}$$

$$\frac{\partial A_2}{\partial z} = i\frac{\mu_0 \omega^2}{2k_2}\mathbf{e}_2 \mathbf{P}^{(2)}(2\omega)e^{-ik_2 z}. \tag{1.34}$$

Substituting the second order polarization in (1.31) and (1.32) into equations (1.33) and (1.34), we obtain the equations governing phase-matching SHG for the slowly varying envelopes of the pump and second-harmonic fields $A_1(z)$ and $A_2(z)$ as following:

$$\begin{aligned} \frac{\partial A_1}{\partial z} &= i\frac{\omega^2}{2c^2 k_1}\mathbf{e}_1 \chi^{(2)}(2\omega, -\omega)\mathbf{e}_2 \mathbf{e}_1 A_1^* A_2 e^{-i(2k_1 - k_2)z}, \\ &= i\frac{\varepsilon_0 k_1}{2\varepsilon_r(\omega)}\mathbf{e}_1 \chi^{(2)}(2\omega, -\omega)\mathbf{e}_2 \mathbf{e}_1 A_1^* A_2 e^{-i(2k_1 - k_2)z}, \end{aligned} \tag{1.35}$$

$$\begin{aligned} \frac{\partial A_2}{\partial z} &= i\frac{\omega^2}{2c^2 k_1}\mathbf{e}_2 \chi^{(2)}(\omega, \omega)\mathbf{e}_1 \mathbf{e}_1 A_1^2 e^{i(2k_1 - k_2)z}, \\ &= i\frac{\varepsilon_0 k_2}{2\varepsilon_r(2\omega)}e_2 \chi^{(2)}(\omega, \omega)\mathbf{e}_1 \mathbf{e}_1 A_1^2 e^{i(2k_1 - k_2)z}. \end{aligned} \tag{1.36}$$

Noticing that for the SHG process, we have $\mathbf{e}_1 \chi^{(2)}(2\omega, -\omega)\mathbf{e}_2 \mathbf{e}_1 = 2\mathbf{e}_2 \chi^{(2)}(\omega, \omega)\mathbf{e}_1 \mathbf{e}_1 = 2\chi_e^{(2)}$, where $\chi_e^{(2)}$ is termed the effective second-order susceptibility value for SHG, then Eq. (1.35) can be simplified as

$$\frac{\partial A_1}{\partial z} = i\frac{2\pi}{\lambda_1 n_1}\chi_e^{(2)} A_2 A_1^* e^{-i(2k_1 - k_2)z}, \tag{1.37}$$

$$\frac{\partial A_2}{\partial z} = i\frac{2\pi}{\lambda_1 n_2}\chi_e^{(2)} A_1^2 e^{i(2k_1 - k_2)z}. \tag{1.38}$$

where n_1, n_2 are the indexes of refraction of the medium at ω, 2ω, and λ_1 are the wavelength of ω. Thus, the analytic solution for real $\chi^{(2)}$ and real input field envelope $A_1(0, t)$ when $A_2(0, t) =$

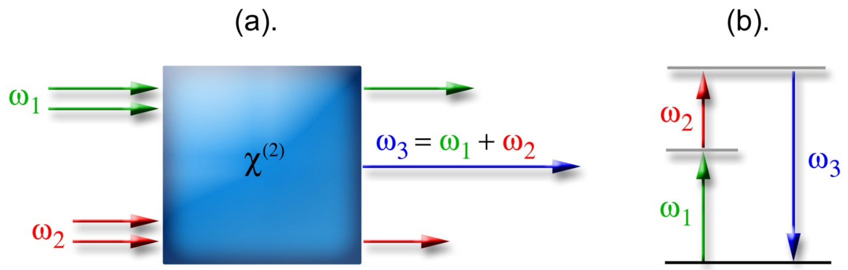

Fig. 1.2: *(a) Schematic diagram of SFG. (b) Energy level scheme of SFG process.*

0 are

$$A_1(z) = A_1(0)\text{sech}\left[\frac{2\pi}{\lambda_1 n_2}\chi_e^{(2)}A_1(0)z\right], \tag{1.39}$$

$$A_2(z) = iA_1(0)\text{tanh}\left[\frac{2\pi}{\lambda_1 n_2}\chi_e^{(2)}A_1(0)z\right]. \tag{1.40}$$

Recalling that $d/dz\,\tanh(z) = \text{sech}^2(z)$ and $d/dz\,\text{sech}(z) = -\text{sech}(z)\tanh(z)$, we obtain the is the intensity of the fundamental and second-harmonic wave:

$$I_1(z,\tau) = I_1(0)\text{sech}^2\left[\frac{2\pi}{\lambda_1 n_2}\chi_e^{(2)}A_1(0)z\right], \tag{1.41}$$

$$I_2(z,\tau) = I_1(0)\text{tanh}^2\left[\frac{2\pi}{\lambda_1 n_2}\chi_e^{(2)}A_1(0)z\right]. \tag{1.42}$$

These solutions are appropriate even when the fundamental field has multi-frequency components, as long as the input field is real, and provided the fundamental field remains within the phase-matching bandwidth throughout propagation in the crystal. When the envelope $A_1(0)$ is not real, Eq. (1.40) and (1.40)must be numerically solved.

We also can find analytical solutions to the dynamical equations for phase-matched SFG and DFG ($\Delta\mathbf{k} = \mathbf{k}_3 - \mathbf{k}_1 - \mathbf{k}_2 = 0$) for input pulses that are not too short (so that group velocity mismatch broadening is negligible). These analytic solutions assist in understanding the nature of the dynamics of SFG and DFG. The dynamic equations governing SFG of phase-matched plane waves are given in the slowly varying envelope approximation as

$$\frac{\partial A_1(z,\tau)}{\partial z} = i\frac{2\pi}{\lambda_1 n_1}\chi_e^{(2)}A_3A_2^*e^{-i(k_1+k_2-k_3)z}, \tag{1.43}$$

$$\frac{\partial A_2(z,\tau)}{\partial z} = i\frac{2\pi}{\lambda_2 n_2}\chi_e^{(2)}A_3A_1^*e^{-i(k_1+k_2-k_3)z}, \tag{1.44}$$

$$\frac{\partial A_3(z,\tau)}{\partial z} = i\frac{2\pi}{\lambda_3 n_3}\chi_e^{(2)}A_1A_2e^{i(k_1+k_2-k_3)z}. \tag{1.45}$$

We consider the case in which one of the applied fields (taken to be at frequency ω_2) is strong, but the other field (at frequency ω_1) is weak. This situation would apply to the conversion of a weak infrared signal of frequency ω_1 to a visible frequency ω_3 by mixing with an intense laser beam of frequency ω_2. This process is known as upconversion because in this process the information-bearing beam is converted to a higher frequency. Usually, optical-frequency waves are easier to detect with good sensitivity than infrared waves. Since we can assume that the amplitude A_2 of the field at frequency ω_2 is unaffected by the interaction, we can take A_2 as a constant in the coupled-amplitude equations (1.43-1.45), which then reduce to the simpler set

$$\frac{\partial A_1(z,\tau)}{\partial z} = K_1 A_3 e^{-i(k_1+k_2-k_3)z}. \tag{1.46}$$

$$\frac{\partial A_3(z,\tau)}{\partial z} = K_1 A_1 e^{i(k_1+k_2-k_3)z}, \tag{1.47}$$

where we have introduced the quantities:

$$K_1 = i\frac{2\pi}{\lambda_1 n_1}\chi_e^{(2)} A_2^*, \quad K_2 = i\frac{2\pi}{\lambda_3 n_3}\chi_e^{(2)} A_2, \tag{1.48}$$

we introduce the positive coupling coefficient κ^2 defined by:

$$\kappa^2 \equiv -K_1 K_2 = \frac{4\pi^2[\chi_e^{(2)}]^2|A_2|^2}{\lambda_1\lambda_3 n_1 n_3}. \tag{1.49}$$

The general solution to Eq. (1.46 - 1.47) is:

$$A_1(z) = A_1(0)\cos(\kappa z), \tag{1.50}$$

$$A_3(z) = -A_1(0)\frac{\kappa}{K_1}\sin(\kappa z). \tag{1.51}$$

To simplify the form of this equation we express the ratio κ/K_1 as follows:

$$\frac{\kappa}{K_1} = -i\sqrt{\frac{n_1\lambda_1}{n_3\lambda_3}}\frac{A_2}{|A_2|}. \tag{1.52}$$

The ratio $A_2/|A_2|$ can be represented as $e^{i\phi_2}$ where phi_2 denotes the phase of A_2. We hence find that

$$A_3(z) = i\sqrt{\frac{n_1\lambda_1}{n_3\lambda_3}}\frac{A_2}{|A_2|}A_1(0)e^{i\phi_2}. \tag{1.53}$$

The principle of optical difference-frequency generation is essentially the same as that of

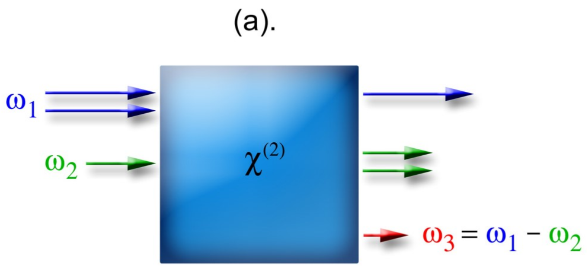

Fig. 1.3: *(a) Schematic diagram of DFG. (b) Energy level scheme of DFG process.*

optical parametric amplification except that, for the former the key issue is the generation of a difference-frequency wave. Still, for the latter, the key issue is the amplification of a low-frequency incident wave. We assume three waves are linearly polarised and propagating along $z-$axis

$$E(\omega_1, z) = \mathbf{a}_1 A_1(z) e^{ik_1 z}, \tag{1.54}$$

$$E(\omega_2, z) = \mathbf{a}_2 A_2(z) e^{ik_2 z}, \tag{1.55}$$

$$E(\omega_3 = \omega_1 - \omega_2, z) = \mathbf{a}_3 A_3(z) e^{ik_3 z}. \tag{1.56}$$

Accordingly, the nonlinear polarization sources of these waves can be expressed as the following forms

$$P^{(2)}(\omega_1, z) = \varepsilon_0 \chi^{(2)}(\omega_2, \omega_3) \mathbf{a}_2 \mathbf{a}_3 A_2(z) A_3(z) e^{i(k_2+k_3)z}, \tag{1.57}$$

$$P^{(2)}(\omega_2, z) = \varepsilon_0 \chi^{(2)}(\omega_1, -\omega_3) \mathbf{a}_1 \mathbf{a}_3 A_1(z) A_3^*(z) e^{i(k_1-k_3)z}, \tag{1.58}$$

$$P^{(2)}(\omega_3, z) = \varepsilon_0 \chi^{(2)}(\omega_1, -\omega_2) \mathbf{a}_1 \mathbf{a}_2 A_1(z) A_2^*(z) e^{i(k_1+k_2)z}.. \tag{1.59}$$

Due to permutation and time reversal symmetry of susceptibility, the following relation holds $\chi_e^{(2)} = \mathbf{a}_1 \chi^{(2)}(\omega_2, \omega_3) \mathbf{a}_2 \mathbf{a}_3 = \mathbf{a}_1 \chi^{(2)}(\omega_1, -\omega_3) \mathbf{a}_1 \mathbf{a}_3 = \mathbf{a}_1 \chi^{(2)}(\omega_1, -\omega_2) \mathbf{a}_1 \mathbf{a}_2$, where $\chi_e^{(2)}$ is the effective nonlinear susceptibility value of the crystal for this process. Substituting Eq. (1.57-1.59) into the nonlinear wave equations of Eq. (1.26) leads to

$$\frac{\partial A_1(z)}{\partial z} = \frac{ik_1}{2n_1^2} \chi_e^{(2)} A_2(0) A_3(0), \tag{1.60}$$

$$\frac{\partial A_2(z)}{\partial z} = \frac{ik_2}{2n_2^2} \chi_e^{(2)} A_3(0)^* A_1(0), \tag{1.61}$$

$$\frac{\partial A_3(z)}{\partial z} = \frac{ik_3}{2n_3^2} \chi_e^{(2)} A_1(0) A_2^*(0). \tag{1.62}$$

Assuming the phase-matching condition of $\Delta k = 0$ is satisfied, the initial boundary conditions of the three waves are $A_2(0) \ll A_1(0)$ and $A_3(0) = 0$. The solutions of equations (1.60-1.62) which satisfy the boundary condition

$$A_2(z) = A_2(0) \cosh \left[\frac{\pi \chi_e^{(2)}}{\sqrt{\lambda_2 \lambda_3 n_2 n3}} A_1(0) z \right], \tag{1.63}$$

$$A_2(z) = i A_2(0) \sqrt{\frac{\lambda_2 n_2}{\lambda_3 n_3}} \sinh \left[\frac{\pi \chi_e^{(2)}}{\sqrt{\lambda_2 \lambda_3 n_2 n3}} A_1(0) z \right]. \tag{1.64}$$

From the above solution, we can see that under the condition of the weak input signal and neglecting depletion of the strong pump wave, both the signal wave and the idle wave experience exponential gain, the gain coefficient is proportional to $\chi_e^{(2)}$ and initial amplitude $A_1(0)$ of the pump wave.

1.1.4 Third order processes. Kerr effect

In section 1.1.3, we have described the elementary mechanism of various three-wave mixing processes. In those cases, three-photon parametric interaction takes place in a second-order nonlinear medium. We now consider various four-wave mixing processes in a third-order nonlinear medium. The common feature of these processes is the parametric interaction between four photons in a third-order nonlinear medium that is transparent at the frequencies of the interacting four photons. For the general-type FWM $\omega_4 = \omega_1 + \omega_2 + \omega_3$, we represent the pump fields as

$$E_j = \mathbf{a}_j A_j e^{i(k_j z - \omega_j t)}, \tag{1.65}$$

where $j = 1, 2, 3$ and k_j are the complex wave vectors of the pump fields. The FWM field is written as

$$E_4 = \mathbf{a}_4 A_4 e^{i(k_4 z - \omega_4 t)}, \tag{1.66}$$

where k_4 is the complex wavevector of the FWM fields. The third-order nonlinear polarization responsible for the considered FWM process is

$$\mathbf{P}^{(3)}(\omega_4) = \epsilon_0 \chi^{(3)}(\omega_1, \omega_2, \omega_3) E_1 E_2 E_3. \tag{1.67}$$

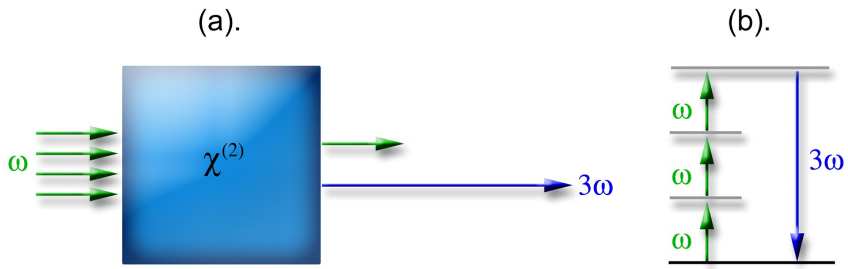

Fig. 1.4: *(a) Schematic diagram of third harmonic generation. (b) Energy level scheme of the third harmonic generation process.*

With no depletion of the pump fields, the SVEA equations give the following expression for the envelope of the i-th Cartesian component of the FWM field

$$\frac{\partial A_4(z)}{\partial z} = \frac{ik_4\varepsilon_0}{\varepsilon_4}\mathbf{a}_4\chi^{(3)}(\omega_1,\omega_2,\omega_3)\mathbf{a}_1\mathbf{a}_2\mathbf{a}_3 A_1A_2A_3 e^{i\Delta\mathbf{k}z}. \tag{1.68}$$

Here $\Delta\mathbf{k} = 3\mathbf{k}_1 - \mathbf{k}_2$ and $\chi^{(3)}$ is the susceptibility for the four-wave mixing processes As an example, Fig. 1.4 depicts the third harmonic generation, i.e., three waves of the same frequency of ω interact with a nonlinear medium to generate a new wave at the frequency 3ω. First, an incident photon of frequency ω is annihilated while a molecule undergoes a transition from its initial state to an intermediate state. The second and third steps are the sequential transitions of this molecule to intermediate states, accompanied by the annihilation of another incident photon of the same frequency. Finally, without any delay, the molecule returns to the initial state while there is the generation of a new photon with the sum-frequency of 3ω. As the time in which the molecule stays in each intermediate state is extremely short, these multiple-step processes occur simultaneously. We can also say that the above-mentioned process is a single-step process with the annihilation of three incident photons and the simultaneous creation of a new sum-frequency photon. In this case the THG field is $E_2 = \mathbf{a}_2A_2e^{i(k_2z-\omega_2t)}$. The dynamic equations governing third harmonic generation (THG) for plane waves are given in the slowly varying envelop approximation by

$$\begin{aligned}\frac{\partial A_2(z)}{\partial z} &= \frac{ik_2\varepsilon_0}{\varepsilon_2}\mathbf{a}_2\chi^{(3)}(\omega,\omega,\omega)\mathbf{a}_1\mathbf{a}_1\mathbf{a}_1 A_1^3 e^{i\Delta\mathbf{k}z}\\ &= \frac{ik_2\varepsilon_0}{\varepsilon_2}\chi^{(3)}A_1^3e^{i\Delta\mathbf{k}z}.\end{aligned} \tag{1.69}$$

These equations are similar in form to Eq. (1.35) and (1.36) for SHG. Now, let us first consider the situation in phase-mismatched condition, i.e., $\Delta k = 3k_1 - k_2 \neq 0$. In that case, the energy from $E_1(\omega, z)$ wave cannot transfer to $E_2(2\omega, z)$ wave effectively. In this case, we can assume that for the fundamental wave, $E_1(\omega, z)$ the amplitude change along the z-axis can be nearly neglected. Under this condition, Eq. (1.69) leads to a solution:

$$A_2(z) = \frac{\varepsilon_0 k_2}{2\Delta k \varepsilon_2} \chi_e^{(3)} A_1^3(0)(e^{i\Delta kz} - 1). \tag{1.70}$$

The intensity change of the third-harmonic wave along the z-direction is

$$I_2(z) \propto |\chi_e^{(3)}|^2 I_1^3(0) \left(\frac{\sin \frac{\Delta kz}{2}}{\frac{\Delta kz}{2}} \right)^2. \tag{1.71}$$

Eq. (1.71) shows a relationship where the intensity of the third harmonic is directly proportional to the cubic power of the fundamental wave's intensity. This intensity varies periodically along the z-axis similar to that for a second-harmonic generation under the condition of phase mismatch. The period of this intensity variation is $2\pi/\Delta k$. A larger Δk leads to smaller peak intensity and more rapid variation.

In order to significantly increase the conversion efficiency, it is necessary to fulfill the phase matching requirement, which entails achieving $\Delta k \to 0$ or $n(\omega) \to n(3\omega)$. For most transparent media the normal dispersion effect makes $n(\omega) > n(3\omega)$. Nevertheless, in specific situations, specialized techniques can be employed to achieve the necessary phase-matching

It is worth noting that, in general, the third-order nonlinear susceptibility is much smaller than the second-order susceptibility even with the phase-matching condition of $\Delta k \to 0$. Consequently, the power transfer efficiency from the fundamental wave to the third harmonic typically ranges from less than 10^-2 to 10^-1 in practical scenarios. Therefore, the undepleted fundamental wave approximation can be applied to a phase-matched case.

For our discussion of SPM of light, let us first consider the case where the propagation of a laser pulse in an isotropic medium can be described by the equation for the slowly varying envelope $A(t, z)$ in a medium with a Kerr-type nonlinearity

$$\frac{\partial A}{\partial z} = \frac{i\mu_0 \omega_0^2}{2k_0} \chi^{(3)} |A|^2 A. \tag{1.72}$$

As usual, the electric field can be expressed in terms of A as $E = Ae^{ik_0 z - i\omega_0 t}$. Letting $A =$

$A_0 e^{i\phi}$, from the above equation, we obtain

$$\frac{\partial A_0}{\partial z} = 0, \tag{1.73}$$

$$\frac{\partial \phi}{\partial z} = \frac{\mu_0 \omega_0^2}{2k_0} \chi^{(3)} |A|^2. \tag{1.74}$$

They yield the solution

$$A_0 = A_0(t), \tag{1.75}$$

$$\phi(z,t) = \phi_0 + \frac{\mu_0 \omega_0^2}{2k_0 c^2} \chi^{(3)} |A|^2 z. \tag{1.76}$$

Equation (1.75) implies that the laser pulse propagates in the medium without any distortion of the pulse shape, while Eq. (1.76) shows that the induced phase change $\Delta\phi(t) = \phi(z,t) - \phi_0$ is simply the additional phase shift experienced by the wave in its propagation from 0 to z due to the presence of the induced refractive index change

$$\Delta n = \frac{1}{2n_0} \chi^{(3)} |A|^2. \tag{1.77}$$

The additional phase shift is given by

$$\Delta\phi = \frac{\omega}{c} \int_0^z \Delta n dz. \tag{1.78}$$

Since the frequency of the wave is $\omega = \omega_o(\partial\Delta\phi/\partial t)$, the phase modulation $\Delta\phi(t)$ leads to a frequency modulation

$$\begin{aligned} \Delta\omega(t) &= -\frac{\partial \Delta\phi}{\partial t} \\ &= -\frac{\mu_0 \omega_0^2}{2k_0 c^2} \chi^{(3)} \frac{\partial |A|^2}{\partial t} z. \end{aligned} \tag{1.79}$$

The spectrum of the self-phase-modulated field is, therefore, expected to be broadened. It can be calculated from the Fourier transformation

$$|E(\omega)| = \frac{1}{2\pi} \int_{-\infty}^{\infty} [A(t) e^{-i\omega_0 t}] e^{i\omega t} dz. \tag{1.80}$$

Cross-phase modulation (XPM) has a similar origin to SPM, which is a result of the nonlinear optical interaction of at least two physically distinguishable light pulses (i.e., pulses with different frequencies, polarizations, mode structures, etc.). The phase modulation of one of the pulses is due to the change in the refractive index of the medium induced by another pulse. We shall consider light pulse possesses two discrete frequency components. In this case, the electric field of the input light pulse with a linear polarization status can be expressed as

$$E = A_1(t)e^{-i\omega_1 t} + A_1(t)e^{-i\omega_2 t}, \tag{1.81}$$

where ω_1 and ω_2 are the central frequencies of these two spectral components, and A_1 and A_2 are their time-dependent amplitude functions. Assuming $A_1 = A_2 = A_0$ the above expression can be simplified as

$$E = A_0 e^{-i(\omega_2+\omega_1)t} = A(t)e^{-i\omega_1 t}, \tag{1.82}$$

where

$$A(t) = A_0(1 + e^{-i(\omega_2-\omega_1)t}) \tag{1.83}$$

The complex field function of the output pulse after passing through the nonlinear medium is

$$A'(t) = A(t)e^{i\Delta\phi(t)} = A_0 e^{-i(\omega_2+\omega_1)t} e^{i\Delta\phi(t)}. \tag{1.84}$$

The cross-action of a pump pulse with a frequency ω_1 on a probe pulse with a frequency ω_2 gives rise to a phase shift of the probe pulse, which can be written as

$$\begin{aligned}
\Delta\phi(z,t) &= \frac{\omega}{c}\int_0^z \Delta n dz \\
&= \frac{\omega}{2n_0 c}\chi^{(3)}|A(t)|^2 z \\
&= \frac{\omega}{2n_0 c}\chi^{(3)} 2A_0^2[1 + cos(\omega_2 - \omega_1)t]z,
\end{aligned} \tag{1.85}$$

where $\omega = (\omega_1 + \omega_2)/2$ is the average frequency of the light pulse. The spectral broadening behavior of the ω_1 line is determined by the Fourier transform:

$$E(\omega) = \frac{1}{2\pi}\int_{-\infty}^{\infty} [A(t)e^{-i\omega_1 t}]e^{-i\omega t} dt. \tag{1.86}$$

Cross-phase modulation also opens the ways to study the dynamics of ultra-fast nonlinear processes, including multi-photon ionization, and to characterize ultrashort light pulses through phase measurements on a short probe pulse.

1.2 Propagation of light pulses in a single waveguide

1.2.1 Nonlinear Schrödinger equation in single waveguide

We have derived the nonlinear Schrödinger to describe the propagation of SVE in a medium without applying any boundary condition. It is convenient for the introduction and discussion of linear and nonlinear phenomenons. Propagation of optical mode in a single waveguide is described by the nonlinear Schrödinger equation. The wave equation can be written in the following form

$$\Delta \mathbf{E} - \frac{1}{c^2}\frac{\partial^2 \mathbf{E}}{\partial t^2} = \mu_0 \frac{\partial^2 \mathbf{P}_L}{\partial t^2} + \mu_0 \frac{\partial^2 \mathbf{P}_{NL}}{\partial t^2}. \tag{1.87}$$

where linear and nonlinear polarization $\mathbf{P}_L$, $\mathbf{P}_{NL}$ are defined as:

$$\mathbf{P}_L(\mathbf{r}, t) = \epsilon_0 \int_{-\infty}^{\infty} \chi^{(1)}(t - t')\mathbf{E}(\mathbf{r}, t')dt', , \tag{1.88}$$

$$\mathbf{P}_{NL}(\mathbf{r}, t) = \epsilon_0 \int_{-\infty}^{\infty} \chi^{(3)}(t - t')\mathbf{E}(\mathbf{r}, t_1)\mathbf{E}(\mathbf{r}t_2)\mathbf{E}(\mathbf{r}, t_3)dt_1 dt_2 dt_3. \tag{1.89}$$

The study of nonlinear effects in optical fibers involves the use of short pulses with widths ranging from 10 ns to 10 fs. Thus, we assume the optical field to be monochromatic and has a spectrum centered at ω_0, so electric field $\mathbf{E}$ has form [1]:

$$\mathbf{E}(\mathbf{r}, t) = \frac{1}{2}\hat{e}[E(\mathbf{r}, t)e^{-i\omega_0 t} + c.c.]. \tag{1.90}$$

Similarly, The polarization $\mathbf{P}_{NL}$ can be written as:

$$\mathbf{P}_{NL}(\mathbf{r}, t) = \frac{1}{2}\hat{e}[P_{NL}(\mathbf{r}, t)e^{-i\omega_0 t} + c.c.], \tag{1.91}$$

where $\hat{e}$ is is polarization unit vector of the optical field. If the nonlinear response is assumed to be spontaneous so that the time-dependent $\chi^{(3)}$ is given by the product of three delta function $\delta(t - t_i)$, then the equation reduces to:

$$\mathbf{P}_{NL}(\mathbf{r}, t) = \epsilon_0 \chi^{(3)}(\mathbf{E}(\mathbf{r}, t)\mathbf{E}(\mathbf{r}, t))\mathbf{E}(\mathbf{r}, t). \tag{1.92}$$

When the electric field in Eq.(1.90) is substituted into polarization Eq. (1.91) $\mathbf{P}_{NL}$ is found to have term oscillating at ω_0 and another term oscillating at the third harmonic frequency $3\omega_0$.

The latter term is generally negligible in optical fibers. Combine with Eq. (1.91), $\mathbf{P}_{NL}$ is found that:

$$P_{NL}(\mathbf{r}, t) = \epsilon_0 \epsilon_{NL} E(\mathbf{r}, t). \tag{1.93}$$

Where the nonlinear dielectric constant is defined as:

$$\epsilon_{NL} = \frac{3}{4}\chi_{(3)}|E(\mathbf{r}, t)|^2. \tag{1.94}$$

Because of the perturbative nature of P_{NL} and the slowly varying envelope approximation, ϵ_{NL} is treated as a constant during the derivation of the propagation equation. The wave equation for the Fourier transform of the slowly varying amplitude $E(\mathbf{r}, t)$ is found to be:

$$\Delta\tilde{E}(\mathbf{r}, \omega) + \epsilon^2(\omega)k_0^2\tilde{E}(\mathbf{r}, \omega) = 0. \tag{1.95}$$

Where $k_0 = \omega/c$, $\epsilon(\omega) = 1 + \tilde{\chi}_1(\omega) + \epsilon_{NL}$ and the Fourier transform of $\tilde{E}$ is defined as:

$$\tilde{E}(\mathbf{r}, \omega - \omega_0) = \int_{-\infty}^{\infty} E_{\mathbf{r},t}e^{-i(\omega-\omega_0)t}dt. \tag{1.96}$$

In our perturbative approach the dielectric constant$\epsilon(\omega)$ is approximately assumed as:

$$\epsilon \approx n^2 + 2n\delta n. \tag{1.97}$$

δn is a small perturbation given by:

$$\delta n = \tilde{n}|E|^2 + \frac{i\tilde{\alpha}}{2k_0} \tag{1.98}$$

where $\tilde{n}$ is measure of fiber nonlinearity and α is fiber absorption. Eq. (1.95) can be solved using the method of separation variables. We assume the solution of the form:

$$\tilde{E}(\mathbf{r}, \omega - \omega_0) = \tilde{A}(z, \omega - \omega_0)F(x, y)e^{i\beta_0 z} \tag{1.99}$$

Where $\tilde{A}$ is a slowly varying function of z and β_0 the wave number. Eq. (1.95) leads:

$$\frac{\partial^2 F}{\partial x^2}\tilde{A} + \frac{\partial^2 F}{\partial y^2}\tilde{A} + F\frac{\partial^2 \tilde{A}}{\partial z^2} + 2i\beta_0 F\frac{\partial \tilde{A}}{\partial z} - \beta_0^2 F\tilde{A} + \epsilon(\omega)k_0 F\tilde{A} = 0. \tag{1.100}$$

Because $\tilde{A}_1(z,\omega)$ is assumed to be a slowly varying function of z, we can neglect the second derivative term. The we obtain the two following equation of F and $\tilde{A}$:

$$\frac{\partial^2 F}{\partial x^2} + \frac{\partial^2 F}{\partial y^2} + [\epsilon(\omega)k_0^2 - \tilde{\beta}^2]F = 0, \tag{1.101}$$

$$2i\beta_0 \frac{\partial \tilde{A}}{\partial z} + [\tilde{\beta}^2 - \beta_0^2]\tilde{A} = 0, \tag{1.102}$$

where we introduce the coefficient $\tilde{\beta}$, which is determined by solving eigenvalue equation (1.101) as

$$\tilde{\beta}(\omega) = \beta(\omega) + \Delta\beta, \tag{1.103}$$

where

$$\Delta\beta = \frac{k_0 \iint_{\infty}^{\infty} \delta n |F(x,y)|^2 dxdy}{\iint_{\infty}^{\infty} |F(x,y)|^2 dxdy}. \tag{1.104}$$

We use the approximated $\tilde{\beta}^2 - \beta_0^2$ by $2\beta_0(\tilde{\beta} - \beta_0)$, Eq.(1.102) then becomes:

$$\frac{\partial \tilde{A}}{\partial z} = i[\beta(\omega) + \Delta\beta - \beta_0]\tilde{A}. \tag{1.105}$$

Combining Eq. (1.90) and Eq.(1.99), the electric field can be written as:

$$\mathbf{E}(\mathbf{r},t) = \frac{1}{2}\hat{e}[F(x,y)A(z,t)e^{i\beta_0 z - i\omega_0 t} + c.c], \tag{1.106}$$

where $A(z,t)$ is the slowly varying pulse envelope. The function $\beta(\omega)$ can be expanded in a Taylor series about carrier frequency ω_0 as:

$$\beta(\omega) = \beta_0 + (\omega - \omega_0)\beta_1 + \frac{1}{2}(\omega - \omega_0)^2\beta_2 + ... \tag{1.107}$$

where :

$$\beta_m = \left(\frac{d^m\beta}{d\omega^m}\right)_{\omega=\omega_0}. \tag{1.108}$$

We assumed the field to be quasi-monochromatic in our approach so the cubic and higher-order terms in this expansion are generally negligible. Substitute Eq.(1.106) into Eq.(1.105), we obtain:

$$\frac{\partial \tilde{A}}{\partial z} = i[(\omega - \omega_0)\beta_1 + \frac{1}{2}(\omega - \omega_0)^2\beta_2 + \Delta\beta]\tilde{A}. \tag{1.109}$$

We take the inverse Fourier transform to go back to the time domain and replace $\omega - \omega_0$ with time differential operator $i\partial/\partial t$. The equation for $A(z,t)$ becomes

$$\frac{\partial A}{\partial z} = -\beta_1 \frac{\partial A}{\partial t} - \frac{i\beta_2}{2}\frac{\partial^2 A}{\partial t^2} + i\Delta\beta. \tag{1.110}$$

Substituting Eq. (1.94) into Eq. (1.111), we obtain that:

$$\Delta\beta = \frac{i\alpha}{2} + \frac{k_0 \tilde{n}|A|^2 \iint_{\infty}^{\infty} |F(x,y)|^2 dxdy}{\iint_{\infty}^{\infty} |F(x,y)|^4 dxdy}. \tag{1.111}$$

Finally, we obtain the nonlinear Schrödinger equation:

$$\frac{\partial A}{\partial z} = -\beta_1 \frac{\partial A}{\partial t} - \frac{i\beta_2}{2}\frac{\partial^2 A}{\partial t^2} - \alpha A + i\gamma|A|^2 A. \tag{1.112}$$

Where γ is the nonlinear parameter defined as:

$$\gamma = \frac{\tilde{n}k_0}{A_{eff}}, \tag{1.113}$$

and

$$A_{eff} = \frac{\iint_{\infty}^{\infty} |F(x,y)|^2 dxdy}{\iint_{\infty}^{\infty} |F(x,y)|^4 dxdy}. \tag{1.114}$$

1.2.2 Solitons

In mathematics and physics, a soliton is a self-sustaining solitary wave caused by nonlinear effects occurring in the material through which the wave propagates. Solitons accompany many physical phenomena and are also found as solutions to nonlinear partial differential equations. The phenomenon of soliton was first described by John Scott Russell, who observed a soliton wave in a water channel (Union Canal, Great Britain) and later reproduced this phenomenon in a specially prepared water tank. Russell named the observed wave "the wave of translation." It is difficult to precisely define what a soliton is. Drazin and Johnson (1989) defined a soliton as a solution to a system of nonlinear differential equations that:

1. Represents waves with an unchanged shape.

2. Is localized in such a way that it decays or reaches a constant value at infinity.

3. Can interact strongly with other solitons, but after the collision, it retains its unchanged

form, experiencing only a phase shift.

Many authors emphasize that solitons can periodically change their shape, and their distinguishing feature is the ability to undergo non-destructive collisions. Two and three-dimensional solitons are also known as "light bullets."

In optics, the term soliton is used to refer to any optical field that does not change during propagation because of a delicate balance between nonlinear and linear effects in the medium. (they are sometimes also called "solitary waves"). Many nonlinear partial differential equations have soliton solutions, e.g. the sine-Gordon equation $\psi_{zz} - \psi_{tt} = \sin(\psi)$ has a solution $\psi(z,t) = -4\tan^{-1}\exp((z-ct)/(1-c^2)^{1/2})$. So does the Kdv equation, $\psi_t + \psi_{zzz} + 6\psi\psi_z = 0$ studied by Korteweg and de Vries in the e nineteenth century as a water wave equation, which admits one-soliton solution $\psi(x,t) = -c/2\,\mathrm{sech}^2[\sqrt{c}/2\,(x-ct-a)]$.

Here we are mostly interested in the solutions to the nonlinear Schrödinger equation, as shown in equation (1.112). If we introduce the retarded time where $t_r = t - z\beta_1$, neglect the linear term α and rescale the equation by introducing time and field envelope so that $t_r = \tau/\sqrt{\beta_2}$, $\psi = \sqrt{\gamma}A$, the NLSE (1.112) can be written in the following standard form:

$$i\frac{\partial\psi}{\partial z} + \frac{1}{2}\frac{\partial^2\psi}{\partial\tau^2} + |\psi|^2\psi = 0. \tag{1.115}$$

Our objective is to find a solution for (1.115) with the given form:

$$\psi(z,\tau) = \Phi(t)e^{ikz}, \tag{1.116}$$

where $\Phi(\tau)$ satisfies the following equation:

$$-\frac{1}{2}\frac{d^2\Phi}{d\tau^2} + k\Phi - \Phi^3 = 0. \tag{1.117}$$

This equation can be integrated subject to the boundary condition that both Φ and its derivative $d\Phi/d\tau$ vanish as y approaches $\pm\infty$. To achieve this, we multiply (1.117) by $d\Phi/d\tau$ and arrive at the following statement:

$$\frac{d}{d\tau}\left[\frac{1}{4}\left(\frac{d\Phi}{d\tau}\right)^2 - \frac{1}{2}k\Phi^2 + \frac{1}{4}k\Phi^4\right] = 0. \tag{1.118}$$

Applying the boundary condition, we obtain:

$$\left(\frac{d\Phi}{d\tau}\right)^2 = \Phi^2(2k - \Phi^2), \tag{1.119}$$

which can be integrated as follows:

$$\int \frac{d\Phi}{\Phi\sqrt{2k - \Phi^2}} = \pm\tau. \tag{1.120}$$

This leads to the expression for Φ:

$$\Phi = \frac{\sqrt{2k}}{\cosh\left(\sqrt{2k}\tau\right)}. \tag{1.121}$$

As a result, we find a stable, localized pulse, known as a soliton, which emerges as the solution of the nonlinear Schrödinger equation:

$$\psi(z,\tau) = \frac{\sqrt{2k}}{\cosh\left(\sqrt{2k}\tau\right)} e^{ikz}. \tag{1.122}$$

In the rest of the thesis, we will use a as an amplitude of the pulse, so we set $a = \sqrt{2k}$. Hence, our "canonical" form of the fundamental soliton, $\psi(z,\tau) = a\,\mathrm{sech}(a\tau)e^{iz\,a^2/2}$.

Equation (1.112) has other kinds of soliton solutions. Dark soliton solutions, wherein a dip appears in a uniform background, exist for Eq. (1.112) for $\beta_2 > 0$. Specifically the equation

$$i\frac{\partial\psi}{\partial z} + \frac{1}{2}\frac{\partial^2\psi}{\partial t^2} + |\psi|^2\psi = 0 \tag{1.123}$$

has a solution of the form

$$\psi(z,\tau) = A\sqrt{B^{-2} - \mathrm{sech}^2(A\tau)}e^{i[\phi(\tau') + (A/B)^2 z}, \tag{1.124}$$

where $\tau' = A\tau + (A^2/B)\sqrt{1-B^2}z$ and

$$\phi(\tau') = \arcsin[B\tanh(\tau')/\sqrt{1 - B\mathrm{sech}^2(t')}]. \tag{1.125}$$

The parameter A is the background level, and $B(|B| \leq 1)$ is the dip depth. For $|B| = 1$, $|\psi(z,t)| = |A\mathrm{tanh}(At)|$, and the intensity of the dip vanishes at the center. This kind of dark soliton is called a black soliton because the intensity at the minimum vanishes.

The stability of solitons to perturbations can be systematically studied using inverse scattering methods. One important type of perturbation involves the case when the peak pulse power is not exactly matched to the required soliton power. It has been verified that, during propagation down the fiber, the pulse adjusts its width to evolve into a soliton; an auxiliary part of the pulse energy is dispersed away as this happens. The pulse evolves into a soliton whose order is an integer $\tilde{N}$ closest to the launched pulse order $N = \tilde{N} + \varepsilon, |\varepsilon < 1/2|$. For example, if the pulse energy is closest to the fundamental soliton, $\tilde{N} = 1$, the pulse width increases if $\varepsilon < 0$, decreases if $\varepsilon > 0$, and no soliton is formed is $N < 1/2$. Moreover, the exact shape of the input pulse is not critical to obtain a fundamental soliton. The width and peak power of the input pulse are not critical to obtain a fundamental soliton. The width and peak power of the input pulse can vary over a wide range and soliton formation will still occur. However, part of the pulse energy will disperse away during the formation process. Other types of perturbations have been studied, such as temporal fluctuations, frequency chirps, etc. We will not pause to enumerate the stability of solitons to various types of perturbations.

1.2.3 Higher order soliton and soliton breathers

The standard fundamental-soliton solution of Eq. (1.115), with arbitrary amplitude a, is

$$\psi_{\text{sol}} = a \exp\left(ia^2/2z\right) \operatorname{sech}(a\tau). \tag{1.126}$$

There is also a special class of solutions of the NLSE, called higher-order solitons, namely solutions whose initial form at $z = 0$ is given by $\psi(0, \tau) = N\text{sech}(\tau)$ with integer N. They have the property that their magnitude is periodic in z, for $N \geq 2$. For instance, when $N = 2$ we obtain

$$\psi(z, \tau) = \frac{\cosh(3\tau) + 3e^{4iz}\cosh(\tau)}{\cosh(4\tau) + 4\cosh(2\tau) + 3\cos(4z)}, \tag{1.127}$$

which has a magnitude that is periodic in z, with period $z_0 = \pi/2$.

There is also a known result of Satsuma-Yajima [2] which predicts that initial condition $\psi(0, \tau) = a\text{sech}(\eta\tau)$ (here a does not have to be an integer) generates a breather composed of

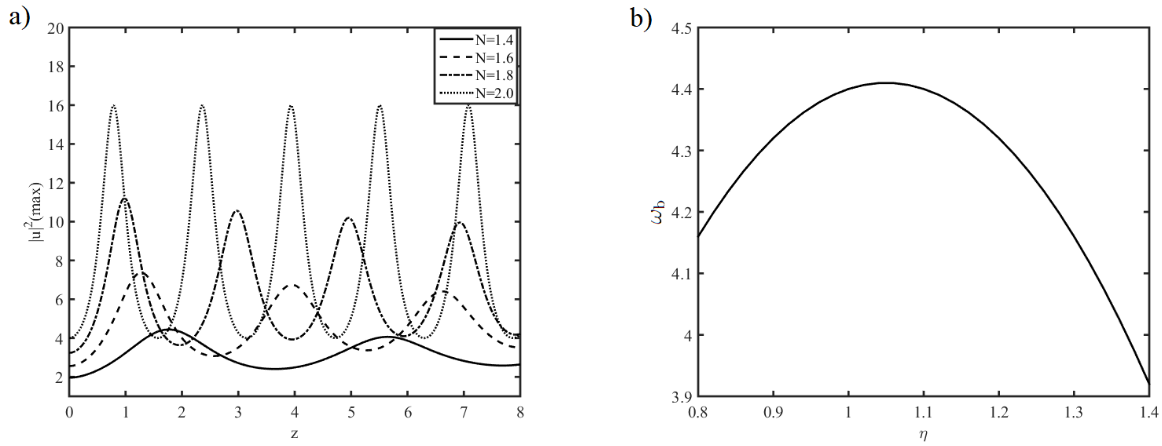

Fig. 1.5: a) *Peak power of high order solitons* $a\,\mathrm{sech}(\tau)$ *respect to propagation distance.* b) *Dependence* K_{beat} *for* $a = 2.1$.

two fundamental solitons in the parameter region

$$3/2 < a/\eta < 5/2. \tag{1.128}$$

Alternatively, this region can be written in the form of

$$2a/5 < \eta < 2a/3. \tag{1.129}$$

In this case, the breather is composed of two fundamental solitons with amplitudes

$$a_1 = 2a - \eta, a_2 = 2a - 3\eta. \tag{1.130}$$

Then, the (spatial) frequency of the internal oscillations of the breather is identified as the beat frequency produced by the superposition of the two fundamental solitons with amplitudes (1.130):

$$\omega_{\mathrm{b}} = \omega(a_1) - \omega(a_2) = 4\eta\,(a - \eta)\,. \tag{1.131}$$

In particular, in the case of $a = 2\eta$, Eq. (1.131) yields $\omega_{\mathrm{b}} = 4\eta^2$, which is a commonly known value for the exact 2-soliton (elementary breather). Periodic evolution of the peak power of breathers with non-integer a is shown in 1.5a If expression (1.131) is considered as a function of η, it attains a maximum at

$$\omega_{\max} = \omega_{\mathrm{b}}\left(\eta_{\max} \equiv a/2\right) = a^2. \tag{1.132}$$

This type of oscillation interplays with inter-core oscillation (will be introduced in section 1.3.4), creating an interesting switching behavior experimentally observed and analyzed in Chapter 2.

1.2.4 Soliton compression

Optical pulses at wavelengths exceeding 1.3 μm generally experience both SPM and anomalous GVD during their propagation in silica fibers. Thus, a single piece of fiber can act as a compressor by itself, without requiring an external grating pair, and such an approach has been used since 1983 for this purpose. The compression mechanism is related to a fundamental property of higher-order solitons. As discussed above, these solitons follow a periodic evolution pattern such that they undergo an initial narrowing phase at the beginning of each period. Because of this property, with an appropriate choice of fiber length, input pulses can be compressed by a factor that depends on the soliton order N. Such a compressor is referred to as the soliton-effect compressor to emphasize the role of solitons. We will refer to this effect in Chapter 3.

1.2.5 Generalized nonlinear Schrödinger equation

In section 1.2.1 we have derived the nonlinear Schrödinger equation with an approximation that the light field propagated in the waveguide is monochromatic. Therefore propagation constant β The nonlinear response has different contributions that behave differently in that respect: the response of the electrons of the medium is normally assumed to be virtually instantaneous. There are also contributions from vibrations of the crystal lattice, which can be excited by intense electric fields and influence the polarization of the medium. Such contributions to the nonlinear polarization occur on rather short timescales, but still long enough to be substantially non-instantaneous e.g. in the context of ultrashort pulses of light. Such a non-instantaneous response means that the induced nonlinear polarization at a certain time depends not only on the electric field intensity at that time but rather on that intensity during some time interval before. This can be described with a response function $R(t)$

$$P_{NL} = \varepsilon_0 \chi^{(3)} E(\mathbf{r}, t) \int_0^{\infty} R(t - t') dt'. \tag{1.133}$$

The response function is in principle defined for arbitrarily large time delays but essentially vanishes within a certain time, during which the system "forgets" any influences from that distant past. There are no contributions from negative time delays because those would violate the principle of causality.

An instantaneous response would simply be described with a response function which is a delta function. The above-mentioned combination of a virtually instantaneous electronic response and a delayed response related to lattice vibrations leads to a combination of a delta function with an oscillatory (but decaying) function $h(t')$:

$$R(t) = (1 - f_R)\delta(t') + f_R h(t'). \tag{1.134}$$

Here, the factor f_R quantifies how strong the contribution of the oscillatory function is; that function is normalized such that its integral over all non-negative time arguments is unity. In a situation where the nonlinear polarization is driven by a relatively long light pulse, the result will be approximately the same as if one would set $f_R = 0$. For shorter light pulses, however, the oscillatory term makes a difference.

The generalized nonlinear Schrödinger equation (GNSE) including effects like coupling coefficient dispersion, self-steepening nonlinearity, and its spectral dependence, stimulated Raman contribution, cross-phase modulation effect, and waveguide losses is expressed in the following form:

$$\frac{\partial A}{\partial z} = \frac{\alpha(\omega)}{2} A + i\beta(\omega) + i\gamma A(1 + is\frac{\partial}{\partial t}) \int_{-\infty}^{\infty} R(t - t')|A|^2 dt', \tag{1.135}$$

where $\beta(\omega)$ and $\gamma(\omega)$ is the nonlinear parameter as a function of frequency, s is the characteristic time of shock wave formation, R is the Raman response function

1.3 Coupled nonlinear Schrödinger equation in dual-core waveguides

In this section, we will discuss systems of two coupled waveguides. Fiber couplers or directional couplers are one such system that is used routinely for a variety of applications related to fiber optics. More specifically, A dual-core fiber, designed to have two cores close to each other throughout its length, can also act as a directional coupler. In order to describe such a system, we have to use the coupled nonlinear Schrödinger equations. In the subsections below, we will

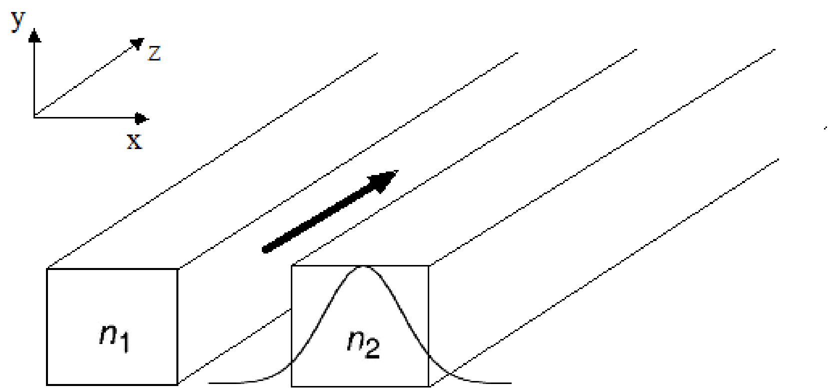

Fig. 1.6: *Schematic illustration of nonlinear switching in a fiber coupler.*

derive and discuss some of their solutions in special cases.

1.3.1 Coupled mode equations

In section 3.1 we derive the NLSE in the single-core waveguide. The same procedure can be applied to derive the coupled mode equation, which describes the wave propagation in couplers. We assume the distance between two cores is close enough to couple them, but does not change the fundamental modes in each core. Using the method of separation variable, the equation (1.95) has an approximated solution: [3]:

$$\tilde{\mathbf{E}}(\mathbf{r},\omega) \approx \hat{e}[\tilde{A}_1(z,\omega)F_1(x,y) + \tilde{A}_2(z,\omega)F_2(x,y)]e^{i\beta z}, \tag{1.136}$$

where $\tilde{A}_{1,2}(z,\omega)$ and $F_{1,2}$ are is a slowly varying functions of z and the modes in each channel, respectively. From the above assumption, each mode must satisfy:

$$\frac{\partial^2 F_m}{\partial x^2} + \frac{\partial^2 F_m}{\partial y^2} + [n_m^2 k_0^2 - \beta_m^2]F_m = 0, \tag{1.137}$$

where $m = 1,2$. We substitute equation (1.136) to equation (1.95) we obtain following equation:

$$\begin{aligned}\sum_m \Bigg\{ \tilde{A}_m \left[\frac{\partial^2 F_m}{\partial x^2} + \frac{\partial^2 F_m}{\partial y^2} + \right] \\ + F_m \left[\frac{\partial^2 \tilde{A}_m}{\partial z^2} + i\beta\frac{\partial \tilde{A}_m}{\partial z} - \beta^2 \tilde{A}_m + n^2(x,y)k_0^2 \tilde{A}_m\right]\Bigg\} = 0.\end{aligned} \tag{1.138}$$

We can rewrite the above equation as:

$$\sum_m \left\{ \tilde{A}_m \left[\frac{\partial^2 F_m}{\partial x^2} + \frac{\partial^2 F_m}{\partial y^2} + n_m(x,y)^2 k_0^2 F_m - \beta_m^2 F_m \right] \right. \\ \left. + F_m \left[i\beta \frac{\partial \tilde{A}_m}{\partial z} + [\beta_m^2 - \beta^2 + k_0^2 n^2(x,y) - k_0^2 n_m^2(x,y)]\tilde{A}_m \right] \right\} = 0. \tag{1.139}$$

The first term in equation (1.139) will vanish due to the (1.137) condition. Here, the second derivative $\partial^2 \tilde{A}_m/\partial z^2$ also vanished because of the slowly varying approximation. We multiply equation (1.139) with F_1^* or F_2 and integrate over the x-y plane, we obtain the coupled mode equations:

$$\begin{aligned} \frac{\partial \tilde{A}_1(z,\omega)}{\partial z} &= i(\beta_1 + \Delta\beta_1^{NL} - \beta)\tilde{A}_1 z, \omega - i\kappa_{12}\tilde{A}_1(z,\omega), \\ \frac{\partial \tilde{A}_2(z,\omega)}{\partial z} &= i(\beta_2 + \Delta\beta_2^{NL} - \beta)\tilde{A}_2 z, \omega - i\kappa_{32}\tilde{A}_2(z,\omega), \end{aligned} \tag{1.140}$$

where κ_{mp} and $\Delta\beta_1^{NL}$ are defined as:

$$\kappa_{mp} = \frac{k_0}{2\beta} \iint_{-\infty}^{\infty} (\tilde{n} - n_p^2) F_m^* F_p dxdy, \tag{1.141}$$

$$\Delta\beta_1^{NL} = \frac{(k_0)^2}{2\beta} \iint_{-\infty}^{\infty} (\tilde{n} - n_L^2) F_m^* F_n dxdy, \tag{1.142}$$

where n_L is the linear part of $\tilde{n}$ and modal distribution F_m are normalised such that $\iint_{\infty}^{\infty} |F_m|^2 dxdy$ $= 1$. By expanding $B_m(\omega)$ in a Taylor series around the carrier frequency ω_0 as:

$$\beta_m(\omega) = \beta_{0m} + (\omega - \omega_0)\beta_{1m} + \frac{1}{2}(\omega - \omega_0)^2 \beta_{2m} + ..., \tag{1.143}$$

keeping term up to second order and replacing $(\omega - \omega_0)$ by a time derivative while taking the inverse Fourier transform, we obtain the time domain coupled mode equation

$$\begin{aligned} &\frac{\partial A_1}{\partial z} + \beta_{11}\frac{\partial A_1}{\partial T} + \frac{i\beta_{21}}{2}\frac{\partial^2 A_1}{\partial T^2} \\ &\qquad = i\kappa_{12}A_2 + i\delta A_1 + i(\gamma_1|A_1|^2 + C_{12}|A_2|^2)A_1, \\ &\frac{\partial A_2}{\partial z} + \beta_{12}\frac{\partial A_2}{\partial t} + \frac{i\beta_{22}}{2}\frac{\partial^2 A_2}{\partial t^2} \\ &\qquad = i\kappa_{21}A_1 + i\delta A_2 + i(\gamma_2|A_2|^2 + C_{21}|A_1|^2)A_2, \end{aligned} \tag{1.144}$$

where $1/\beta_{1m}$ is group velocity and β_{2m} is group velocity dispersion (GVD) in the m-th core.

We introduce

$$\delta = \frac{1}{2}(\beta_{01} - \beta_{02}), \beta = \frac{1}{2}(\beta_{01} + \beta_{02}). \tag{1.145}$$

The parameter δ_1 is the mismatch between the two cores. The nonlinear parameters γ_m and C_{mn}, where $m, n = 1$ or 2 are defined as:

$$\gamma_m = n_2(k_0) \iint_{-\infty}^{\infty} |F_m|^4 dxdy, \tag{1.146}$$

$$C_{mn} = 2n_2(k_0) \iint_{-\infty}^{\infty} |F_m|^2 |F_n|^2 dxdy, \tag{1.147}$$

where the parameter γ_m corresponds to self-phase-modulation(SPM) and C_{mn} is corresponds to cross-phase-modulation(XPM).

The set of equations (1.144) are valid under quite general conditions and include both the linear and nonlinear coupling mechanisms between the optical fields propagating inside the two cores of an asymmetric fiber coupler. They simplify considerably for a symmetric coupler with two identical cores. Using $\delta a = 0$, $\kappa_{12} = \kappa_{21} \equiv \kappa$, and $C_{12} = C_{21} \equiv \gamma\Gamma$, the coupled-mode equations for symmetric couplers become

$$\begin{aligned} \frac{\partial A_1}{\partial z} + \beta_1 \frac{\partial A_1}{\partial t} + \frac{i\beta_2}{2} \frac{\partial^2 A_1}{\partial t^2} &= i\kappa A_2 + i\gamma(|A_1|^2 + \Gamma |A_2|^2) A_1, \\ \frac{\partial A_2}{\partial z} + \beta_1 \frac{\partial A_2}{\partial t} + \frac{i\beta_2}{2} \frac{\partial^2 A_2}{\partial t^2} &= i\kappa A_1 + i\gamma(|A_2|^2 + \Gamma |A_1|^2) A_2, \end{aligned} \tag{1.148}$$

where the subscript identifying a specific core has been dropped from the parameters β_1, β_2, and γ since they have the same values for both cores. The XPM parameter Γ is quite small in practice and can often be neglected altogether. The reason is related to the fact that the integral in Eq. (1.147) involves overlap between the mode intensities and is relatively small even when the two cores are close enough that κ (involving between the mode amplitudes) cannot be neglected.

The set of equations (1.148), if considered with only linear terms, can be solved analytically. In the following sections, we will derive solutions for most simple cases which will provide fundamentals of the explanations of complicated couplers.

1.3.2 Coupled nonlinear Schrödinger equation and analytic solutions.

In this section, we present a recapitulation of analytic results of linearly coupled NLSE, but standard, known in the literature, and the new solutions that we found and discussed in the

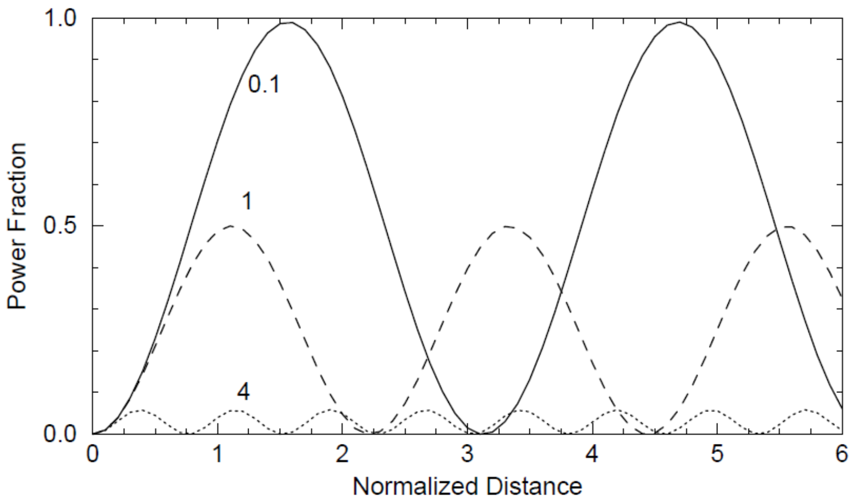

Fig. 1.7: *Energy in first and second cores for four values of σ when a CW beam is launched in one core at $z = 0$.*

papers published throughout my Ph.D. studies. In the following chapters, when I will analyze the series of experiments for various systems of all-optical switches, and present my numerical simulations, I will refer to these results.

1.3.3 Low-power CW beam in couplers

We start with considering the simplest case of the equations (1.148) for a low-power CW beam incident on one of the input ports of a fiber coupler. The time-dependent terms in (1.144) are set to zero. Due to the low energy of CW, the nonlinear terms are also negligible. First, we assume that the coupling is constant $\kappa(\omega) = \kappa_0$. Then, we define dimensionless parameters distance, amplitude, and mismatch between the two cores: $\zeta = z(2\kappa_0/\pi)$, and $\psi = \sqrt{\gamma/\kappa_0}A$, $\sigma = \delta/\kappa_0$ and cast remaining term of equations (1.144) in the following form

$$\frac{d\psi_1}{d\zeta} = i\psi_2 + \sigma\psi_1, \tag{1.149}$$

$$\frac{d\psi_2}{d\zeta} = i\psi_1 - \sigma\psi_2. \tag{1.150}$$

By differentiating Eq.(1.149) and eliminating $d\psi_2/d\zeta$ using Eq. (1.150), we obtain the following equation for ψ_1:

$$\frac{d^2\psi_1}{d\zeta^2} + \kappa_e^2\psi_1 = 0, \tag{1.151}$$

where the effective coupling coefficient κ_e is defined as

$$\kappa_e = \sqrt{1+\sigma^2}. \tag{1.152}$$

The same harmonic-oscillator-type equation is also satisfied by ψ_2. By using the boundary condition that a single CW beam is incident on one of the input ports such that $\psi_1(0) = \psi_0$ and $\psi_2(0) = 0$ where ψ_0 is an arbitrary constant amplitude, the solution of Eqs. (1.149) and (1.150) is given by

$$\psi_1(\zeta) = \psi_0[\cos(\kappa_e\zeta) + i(\sigma/\kappa_e)\sin(\kappa_e\zeta)], \tag{1.153}$$

$$\psi_2(\zeta) = \psi_0(i/\kappa_e)\sin(\kappa_e\zeta). \tag{1.154}$$

Thus, even though $\psi_2 = 0$ initially at $z = 0$, some power is transferred to the second core as light propagates inside the fiber coupler. Figure 1.7 shows the ratio $|\psi_2/\psi_0|^2$ as a function of ζ for several values of σ. In all cases, power transfer to the second core occurs periodically. The maximum power is transferred at distances such that $\kappa_e z = m\pi/2$, where m is an integer. The shortest distance at which maximum power is transferred to the second core for the first time is called the coupling length and is given by $L_c = \pi/(2\kappa_e)$.

In the case that the frequency dependence of the coupling coefficient κ cannot be ignored, it can be included by expanding $\kappa(\omega)$ in a Taylor series around the carrier frequency ω_0 so that:

$$\kappa(\omega) = \kappa_0 + (\omega-\omega_0)\kappa_1 + \frac{1}{2}(\omega-\omega_0)^2\kappa_2, \tag{1.155}$$

where $\kappa_m = d^m\kappa/d\omega_m$ is evaluated at $\omega = \omega_0$. The exact solutions of more complex couplers where the first-order time-derivative terms can also be obtained. We rescale the parameter for the first order coupling $\epsilon = \kappa_1/\sqrt{\kappa_0|\beta_2|}$. Equations (1.158) and (1.159) then become

$$i\frac{\partial\psi_1}{\partial\zeta} = -i\epsilon\frac{\partial\psi_2}{\partial\tau} - \sigma\psi_1 - \psi_2, \tag{1.156}$$

$$i\frac{\partial\psi_2}{\partial\zeta} = -i\epsilon\frac{\partial\psi_1}{\partial\tau} - (\alpha_2-\alpha_1)\frac{\partial\psi_2}{\partial\tau} + \sigma\psi_2 - \psi_1, \tag{1.157}$$

where $\alpha_1 = \beta_{11}/\sqrt{\kappa_0|\beta_{21}|}$, $\alpha_2 = \beta_{12}/\sqrt{\kappa_0|\beta_{21}|}$, $\tau = t_r\sqrt{\kappa_0/\beta_2}$ with retarded time $t_r = t - z\beta_1$.

The solution of equations (3.58) and (3.59) is

$$\begin{aligned} \psi_1(\zeta) &= \psi_0 \sin(K\zeta)\, e^{i(p\zeta-\Omega\tau)}, & (1.158)\\ \psi_2(\zeta) = &= \psi_0 \left[A\cos(K\zeta) + iB\sin(K\zeta)\right] e^{i(p\zeta-\Omega)}. & (1.159) \end{aligned}$$

Here Ω is an arbitrary frequency shift, which defines the family of the CW solutions. Further, p is the corresponding shift of the propagation constant, B is the relative amplitude of the waves in the two cores, and $2\pi/K$ is the period of the power switching between the cores. The latter parameters are expressed in terms of Ω as follows:

$$\begin{aligned} A &= -\left[\sigma + \frac{\Omega}{2}(\alpha_1-\alpha_2)\right]/(1+\epsilon\Omega), & (1.160)\\ B &= K/(1+\epsilon\Omega), & (1.161)\\ p &= -\frac{1}{2}\Omega^2 + \frac{\Omega}{2}(\alpha_1-\alpha_2), & (1.162)\\ K^2 &= (1+\epsilon\Omega)^2 + \left[\sigma + \frac{\Omega}{2}(\alpha_1-\alpha_2)\right]^2. & (1.163) \end{aligned}$$

This solution is tantamount to the previously known one [1]. The exact CW solution, given by Eqs. (1.158)-(1.163), is a novel finding. It can be obtained if the Doppler shift, $(\alpha_1-\alpha_2)\,\Omega$, is added to the phase-velocity mismatch, 2σ. The asymmetry of the solution is characterized by the ratio of the amplitudes:

$$\frac{\max\left(|\psi_2(\zeta)|\right)}{\max\left(|\psi_1(\zeta)|\right)} = \sqrt{B^2+K^2} \equiv \sqrt{1 + 2\left[\sigma + \frac{\Omega}{2}(\alpha_1-\alpha_2)\right]^2}, \qquad (1.164)$$

where index 2 represents the excited core. Note that the asymmetry is canceled at a specially chosen value of the frequency shift,

$$\Omega_0 = -2\sigma/(\alpha_1-\alpha_2). \qquad (1.165)$$

1.3.4 Low power pulses in couplers

In the case of low-energy optical pulses, nonlinear effects can be neglected but the effects of fiber dispersion should be included. Practically, the second-order term in coupling expansion is negligible for pulses as short as 0.1 ps. For symmetric couplers, the coupled mode equations, the set of Eqs.(1.148) become:

$$i\frac{\partial\psi_1}{\partial\zeta} = \frac{s}{2}\frac{\partial^2\psi_1}{\partial\tau^2} - i\epsilon\frac{\partial\psi_2}{\partial\tau} - \psi_2, \tag{1.166}$$

$$i\frac{\partial\psi_2}{\partial\zeta} = \frac{s}{2}\frac{\partial^2\psi_2}{\partial\tau^2} - i\epsilon\frac{\partial\psi_1}{\partial\tau} - \psi_1. \tag{1.167}$$

where $s = \mathrm{sgn}(\beta_2) = \pm 1$. Conventionally, dispersion length is defined as $L_D = T_0^2/\beta_2$, where T_0 is related to the pulse width. Moreover, the coupling length is defined as $L_c = \pi/(2\kappa)$. However, in the Eqs. (1.166)-(1.167) above, the dimensionless unit variables of time and distance are defined in such a way that the coupling and dispersion parameters are rescaled to 1. Thus, the dispersion is only characterised by pulse width $\eta = t_0/T_0^2$, where $t_0 = \sqrt{|\beta_2|/\kappa}$ is dimensionless units of time. GVD effects become significant only for ultrashort pulses with pulse width $T_0 < 0.1$ ps and for pulses with $T_0 > 1$ ps GVD effects are negligible since the coupling strength κ is typically much larger than 1. In the case that the GVD term in Eqs. (1.166)-(1.167) is neglected, e.g. picosecond optical pulses, the resulting equations become identical to those applicable for CW beams. Therefore, the energy is transferred to the neighboring core periodically when such pulses are incident on one of the input ports of a fiber coupler. The analytical solution of (1.166)-(1.167) yields

$$\begin{aligned}\psi_1(z,\tau) &= \frac{1}{2}[\psi_0(\tau-\epsilon\zeta)e^{i\zeta} + \psi_0(\tau+\epsilon\zeta)e^{-i\zeta}],\\ \psi_2(z,\tau) &= \frac{1}{2}[\psi_0(\tau-\epsilon\zeta)e^{i\zeta} - \psi_0(\tau+\epsilon\zeta)e^{-i\zeta}].\end{aligned} \tag{1.168}$$

When $\kappa_1 = 0$, the solution reduces to

$$\psi_1(z,\tau) = \psi_0(\tau)\cos(\zeta), \quad \psi_2(z,\tau) = \psi_0(\tau)\sin(\zeta). \tag{1.169}$$

The solution (1.169) shows that the pulse switches back and forth between the two cores while maintaining its shape when the frequency dependence of the coupling coefficient can be neglected. However, when ϵ is not negligible, Eq. (1.168) shows that the pulse will split into two sub-pulses after a few coupling lengths, and separation between the two would increase with propagation. This effect is referred to as inter-modal dispersion and is similar to polarization-mode dispersion occurring in birefringent fibers. Inter-modal dispersion was observed in a 1997 experiment by launching short optical pulses (width about 1 ps) in one core of a dual-core fiber with the center-to-center spacing $d \approx 4a$ [14]. The auto-correlation traces showed evidence of pulse splitting after 1.25 m, and the sub-pulses separated from each other at a rate of 1.13 ps/m. The coupling length was estimated to be about 4 mm. Inter-modal dispersion in fiber couplers becomes of concern only when the coupler length $L \gg L_c$ and pulse widths are approximately 1 ps or shorter.

We have found the solutions of NLSEs regarding mismatch and dispersive coupling separately, each with CWs or short pulses (> 1 ps). We now consider both of these effects, while including GVD, in the case of ultrashort pulses. The NLSE for the ultrashort pulse is written as:

$$i\frac{\partial\psi_1}{\partial\zeta} = \frac{s}{2}\frac{\partial^2\psi_1}{\partial\tau^2} - \epsilon\frac{\partial\psi_2}{\partial\tau} - \sigma\psi_1 - \psi_2, \tag{1.170}$$

$$i\frac{\partial\psi_2}{\partial\zeta} = \frac{s}{2}\frac{\partial^2\psi_2}{\partial\tau^2} - \epsilon\frac{\partial\psi_1}{\partial\tau} + \sigma\psi_2 - \psi_1. \tag{1.171}$$

The simplified form of the exact solution admits a more sophisticated exact solution. It is a two-component chirped Gaussian pulse, localized (and, in the general case, moving) along the temporal coordinate, with two components periodically oscillating between the cores. These solutions also contain an arbitrary frequency shift Ω, cf. Eqs. (1.158) and (1.159):

$$\begin{aligned}(\psi_1)_{\text{Gauss}} &= \Phi(\zeta)\sin\left(\sqrt{1+\sigma^2}\zeta\right)\\ &\quad\times\exp\left(-\frac{1}{2}\varphi(\zeta)\left(T+\Omega\zeta\right)^2 - i\Omega T - \frac{i}{2}\Omega^2\zeta\right),\end{aligned} \tag{1.172}$$

$$\begin{aligned}(\psi_2)_{\text{Gauss}} &= \Phi(\zeta)\left[-\sigma\cos\left(\sqrt{1+\sigma^2}\zeta\right) + i\sqrt{1+\sigma^2}\sin\left(\sqrt{1+\sigma^2}\zeta\right)\right]\\ &\quad\times\exp\left(-\frac{1}{2}\varphi(\zeta)\left(T+\Omega\zeta\right)^2 - i\Omega T - \frac{i}{2}\Omega^2\zeta\right),\end{aligned} \tag{1.173}$$

where $\varphi(\zeta)$ and $\Phi(z)$ are the following complex functions:

$$\varphi(\zeta) = \frac{1}{W^2+i\zeta}, \tag{1.174}$$

$$\Phi(\zeta) = \frac{W\psi_0}{\sqrt{W^2+i\zeta}}, \tag{1.175}$$

with an arbitrary parameter W which determines the width of the Gaussian. The oscillation period between the cores is determined by the ζ-dependence of the energies of components

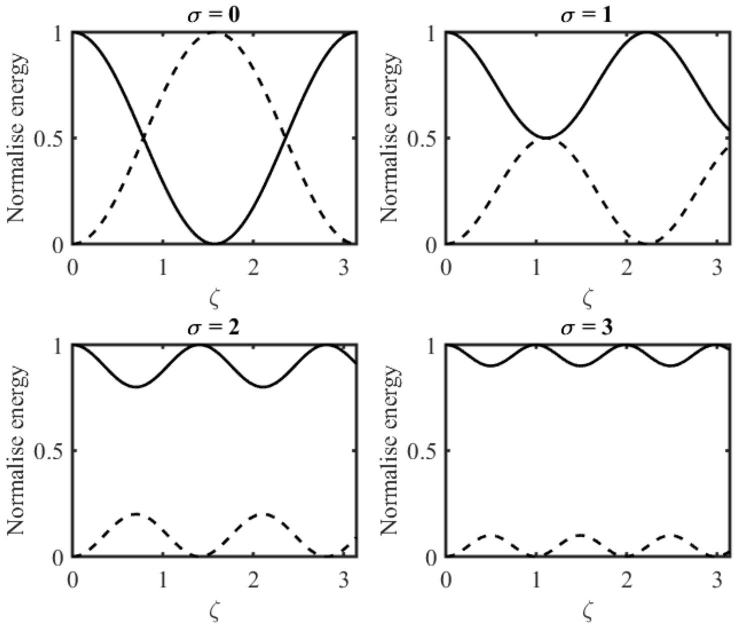

Fig. 1.8: *Energy in first and second cores for four values of σ when a pulse with initial form* $\mathrm{sech}(\eta\tau)$ *is launched in one core at $z = 0$.*

(1.172) and (1.173), cf. Fig. 3.11 below:

$$\left\{\begin{array}{c} E_1(\zeta) \\ E_2(\zeta) \end{array}\right\} = \sqrt{\pi}\,|\psi_0|^2\,W \left\{\begin{array}{c} \sin^2\left(\sqrt{1+\sigma^2}\zeta\right) \\ \sigma^2 + \cos^2\left(\sqrt{1+\sigma^2}\zeta\right) \end{array}\right\}. \tag{1.176}$$

Naturally, the total energy, $E_1(\zeta) + E_2(\zeta)$, stays constant in the course of the oscillations between the cores. As concerns the frequency shift, it is related to the experimentally controllable shift $\Delta\lambda$ of the carrier wavelength, λ_0. In physical units, the relation is

$$\Omega_{\mathrm{phys-units}} \approx -\frac{2\pi c_0}{n\lambda_0^2}\Delta\lambda, \tag{1.177}$$

where c_0 is the light speed in vacuum, and n is the refractive index. In the scaled form adopted above, the value is

$$\Omega = t_0\Omega_{\mathrm{phys-units}},$$

where t_0 is the time unit defined as $t_0 = \sqrt{|\beta_2|\kappa}$. Such a simple analytical approach allows us to evaluate the excitation wavelength effect on the coupling efficiency. It is predicted that decreasing the excitation wavelength will reduce the coupling efficiency. Due to that reason, we chose the excited wavelength accordingly with other parameters of the fiber in Chapter 3, to maximize the switching performance.

1.4 Photonic crystal fibers

1.4.1 Introduction

An optical fiber is a cylindrical dielectric waveguide (nonconducting waveguide) that transmits light along its axis through the process of total internal reflection. A fiber consists of a core surrounded by a cladding layer, both of which are made of dielectric materials. Photonic crystal fibers (PCF) are optical fibers with regular refractive index material structures in the background with a high refractive index. They operate on the same index-guiding principle as conventional optical fiber — however, they can have a much higher effective refractive index contrast between core and cladding and therefore can have much stronger confinement for applications in nonlinear optical devices, and polarization-maintaining fibers. One of the most important advantages offered by photonic crystal fibers (PCFs) is the high design flexibility. In fact, by changing the geometric characteristics of the fiber cross-section, such as the air-hole dimension or disposition, it is possible to obtain fibers with opposed optical properties [4]. Thus, they can also be made with much lower effective index contrast. Few optical parameters like birefringence, chromatic dispersion, effective mode area, loss of confinement, and non-linearity can be determined by PCF. Due to their unique geometric structure, PCF possesses special properties and capabilities that lead to an outstanding potential for supercontinuum generation and sensing applications.

There has been a lot of research on Photonic Crystal Fiber and the PCF technology has been modified by those researches. In 1978, the Bragg Fiber Idea revolutionized telecommunications with component sensors and filters, but there were the main disadvantages encountered were no large modes, their enormous size, and greater losses [5]. Later in 1992, the fiber design included the Total Internal Reflection method with good perforation in telecommunications except with a few problems such as limited choice of material, and restricted core diameter for single-mode operation [6].

In 1996, the photonic coated fiber was manufactured with additional characteristics of increased durability, high strength, and high-temperature resistance according to use in nuclear radiation, harsh chemical environments, medical applications, etc.

In 1997, single-mode PCF with no higher order modes regardless of optical wavelength, low non-linearity, and low confinement loss was used as filtering mode, sensors, interferometers, etc. [7]. In 1999, PCF with photonic band-gap air core was implemented as a different variety of wave-guide structures in the core of an array of air holes for various purposes [8].

In 2000, PCF was made of highly birefringent with different diameters of air holes along the two orthogonal axes or high data rates and fiber loop production due to uneven core design. In the same year, Supercontinuum generation was generated by high non-linear PCF and Zero Dispersion Wavelength applications in Pulse Compression, Laser Sour Spectroscopy, WDM, etc. [9]. Later in 2001 work of manufacture of Bragg fiber eventually found uses in optical sensors, fiber laser, and PCF laser with double cladding (Ytterbium-doped double-clad) provided high power was found by Fabry Perot specification. PCF with ultra-flattened dispersion was implemented in 2002 in which Zero Dispersion was acquired at a much broader wavelength range of 1-$1.6\mu m$ used primarily for supercontinuum generation. Bragg fiber with air core and silica was present in 2003, reducing the loss of non-linearity propagation and filling in as a model to consider the non-linear optical stage materials [10]. Chalcogenide Photonic Crystal Fibers (CPCF) were developed in 2004 and offered several unique optical properties such as a transmission window that extends far into the infrared spectral region and demonstrates an extraordinarily high nonlinear refractive-index coefficient.

In 2005, Kagome Lattice PCF was implemented with a gas-filled hypo-cycloid fiber containing three very strong band gaps overlapping to provide low loss at a very large wavelength range. The pressure and temperature of the gas can be observed as also the gas's significant contribution to the refractive index, which was used to design bright temporally coherent optical sources [5]. Furthermore, in the year of 2006, the creation of Hybrid Photonic Crystal Fiber, a type of PCF made up of air holes and germanium-silica rods prepared around an un-doped silica core which guides light inside a core by Total Internal Reflection (TIR) and anti-resonant reflection guidance. Later in 2007, Silicon Double Inversion was used to produce photonic crystal polymer templates that were an intermediate approach where silica was produced at room temperature via Atomic Level Deposition (ALD). Hollow Core Photonic Band Fiber (HC-PCF) which was free of surface modes was developed in 2009. Due to the complete elimination of surface modes, there will be a substantial increase in fiber bandwidth, and a reduction in dispersion may easily lead to more carrying capacity [11]. In 2013, the Double Cladding of Seven Photonic Crystal Fibers was implemented in which each core was made to transmit only the basic mode known as the super mode and offered great support in making a multi-core fiber with proper guiding properties for high-power supercontinuum generation [12]. Another very effective nano-displacement sensor, which can work directly for horizontal as well as vertical displacement, was acquired in 2014 as a PCF - based on a slightly different sensitivity nano-displacement sensor. different sensitivity. For mid-infrared supercontinuum generation, Photonic Crystal Fibers - with an equiangular 8 mm long PCF were intended in 2015. This would generate laser pulses with a high power of 500W [13]. The PCFs were later integrated into a Fiber Laser. For High Power Applications, a monolithic fiber with a 40μm core with Yb-do PCFs amplifier configuration generating up to 210 W average powers at 1064 nm was introduced. Helically twisted photonic crystal fibers (PCFs) were analyzed in 2016 based on the Helical Bloch theory. This twisted periodic 'space' causes spiral light across the fiber axis and will include dips in the transmission spectrum, and core-less PCF may have low loss guidance [14].

1.4.2 Types of photonic crystal fibers

Photonic Crystal Fiber can be illustrated as a structure comprised of a core and clad, ensuring the propagation law of total internal reflection as in usual fiber. Periodic nano-structures influence photon motion as this ionic lattice affects electrons in solids. It occurs naturally in the shape of coloring the structure. The core of this particular fiber is made of silica as a solitary material and can either be solid or hollow. The core is encompassed via air holes that experience the fiber so it is called 'holey' or' microstructured fiber and because of this structure the light is restricted and transferred through the core which goes about as a cavity. Photonic crystal fibers can be divided into two modes of operation, according to their mechanism for confinement: index guiding and photonic bandgap [15].

Index guiding photonic crystal fiber: In index guiding PCF light is centered by the total internal reflection between the solid core and various air gaps cladding. The solid core of file controlling PCF with a miniaturized scale basic exhibit of air gaps is encompassed by unadulterated silica cladding with a refractive index of 1.462. Because of the huge refractive index difference between air (1.000) and silica (1.462), the light is centered by total internal reflection which is an element of wavelength. Effective Refractive Index fundamentally measures the stage delay per unit length in PCF concerning stage delay in a vacuum.

Photonic band-gap fiber: Photonic band-gap fiber is obtained by the structure formed as if the core part of the air holes array is simply replaced by a much larger hole of much larger diameter in comparison to the surrounding holes. There is an adjustment in its optical properties because of the deformity of the broken structure of periodicity. No electromagnetic modes are permitted to have a recurrence in the hole. Its impact is displayed in photonic crystal band-gap fiber where the wavelength controls light in a low index core region. The light-controlling wonder in the fiber depends on the recurrence of the outside light if matches the band-gap recurrence, the light gets limited in the holes and like manner is guided all through the length of the fiber. So there is no prerequisite higher refractive index of the center.

1.4.3 Analysis of the optical properties

Birefringence is an important parameter in fiber optics and many detecting gadgets where light needs to hold a straight polarization area, regularly requiring high birefringence. Normally materials with uniaxial anisotropy - the hub of symmetry is called the optical pivot of a specific material and has no comparable hub in the plane opposite to it - display this optical phenomenon. Liner polarized light beams in parallel and opposite headings will express uneven effective refractive indices ne and no for unexpected and normal developing beams separately. At the point when an un-captivated light emission goes through the material with a nonzero intense edge to the optical hub, the oppositely spellbound segment may confront refraction at an edge according to the ordinary law of refraction and its contrary part at a non-standard point appeared by the distinction between the two compelling refractive records called as the birefringence extent.

Chromatic Dispersion: The total waveguide and material dispersion add to the chromatic dispersion or total dispersion. The material dispersion is trademark to the use of material to create the fiber though the waveguide dispersion can fluctuate by changing the plan parameter of the waveguide in this way all out scattering is permitted to be modified.

Confinement Loss: The occurrence of limited air holes in the center region causes the optical mode to leak from the inner core region to the outer air holes and this is inevitable, resulting in confinement losses. Fundamental mode is used to calculate confinement loss from the imaginary part of the complex effective index n_{eff}, using $L_c = (1/\lambda)(40\pi/ln(10))\,\mathrm{Im}(n_{eff})$. Confinement Loss is the leakage of light from the material of the core to the material of the external matrix. It can be changed according to the parameters like number of air holes, number of layers, air hole diameter, and pitch.

Zero Dispersion Wavelengths (ZDW): For optical fibers, ZDW is the wavelength where the group delay dispersion (second-order dispersion) is zero. For PCFs with small mode areas, which can execute particularly strong waveguide dispersion, the ZDW can be shifted into the visible spectral region, so that anomalous dispersion is obtained in the visible wavelength region, allowing for soliton transmission. PCFs as well as some other fiber designs can generate two or three different ZDW. SCG (Supercontinuum Generation) can lead to particularly broad optical spectra when the pump light has a wavelength near the ZDW.

Effective Mode Area: A_{eff} of the PCF is follows by the equations $A_{eff} = (\int\int |E|^2 dxdy)^2 / \big(\int\int |E|^4 dxdy\big)$, where E is the electric field amplitude. The integration is cross over the center zone, yet over the entire plane surface. A significant impact of a small effective mode area is that the optical intensities for a given power level are high, making nonlinearities important.

Non-linearity The non-linear coefficient of PCF represents a very significant parameter during SCG analysis. Nonlinear coefficient γ is directly corresponding to nonlinear refractive index (n_2) and contrarily proportional to the effective area (A_{eff}). The non-linear coefficient of PCF is defined, as $\gamma = 2\pi n_2/(\lambda A_{eff})$.

1.4.4 Applications of PCF

Applications of photonic crystal fibers include lasers, amplifiers, dispersion compensators, and nonlinear processing. Photonic crystal fiber structures are currently produced in many laboratories worldwide using a variety of different techniques. Below we list several specific applications.

- A highly nonlinearly designed PCF with 4 strands of air holes with different diameters can be accessed for broadband supercontinuum generation that is used in dermatology, ophthalmology, dental, and detection of dermatology.
- PCF-in-PCF structure shows ultra-flattened negative dispersion at a large range of wavelengths ranging from 1360 to 1690 nm and can be utilized for residual dispersion compensation in optical transmission
- Varying the diameters of the inner air opening can be utilized for supercontinuum generation and gives a flat dispersion profile formed-infrared range from 1- 10μm. A highly nonlinear photonic hexagonal crystal fiber with a structure of five rings can be used.
- Photonic crystal fiber with a central core region doped with GeO2, abutter fly lattice structure, and fiber Bragg grating (FBG) fetched in the core can be used as an optical fiber pressure sensor.

- A chalcogenide glass PCF with square lattice and hexagonal lattice structure with the pitch of $0.2\mu m$ can be used as dispersion compensating fibers. In comparison to silica, this fiber makes available high negative dispersion in the wavelength range 1.2– $1.6\mu m$.

Chapter 2

Optical switching in symmetrical dual-core highly nonlinear optical fibers

In this chapter, we investigate the switching mechanism (optical coupler) in the dual-core photonic-crystal fiber. We focus the input beam on one of the channels, to study the stability of the transmission and identify a threshold between switching and self-trapping in either channel. A model that includes the two coupled channels with intrinsic dispersion and nonlinearity provides surprisingly good agreement with the experimental findings.

The realization of all-optical switching in a simple format has long been a challenge for nonlinear fiber optics. The concept of nonlinear directional couplers based on dual-core fibers (DCFs) was introduced theoretically in the early 1980s [16–18]. Since then, considerable effort has been devoted to the characterization and optimization of the device performance [1, 19]. In particular, a promising demonstration of ultrafast nonlinear switching had been reported utilizing femtosecond pulses in the normal-group-velocity-dispersion (GVD) range of the silica fiber coupler [20]. The main limitations of ultrafast nonlinear switching in conventional nonlinear couplers are relatively high powers (100 kW) required for the signal redirection, and the ensuing breakup in the temporal domain [20, 21]. Additionally, the switching performance is compromised by the intra-channel and inter-modal GVD, which strongly affects pulses of width 100 fs. To avoid the degradation driven by these factors, it was proposed to exploit temporal solitons [22], taking advantage of their robustness. Numerous theoretical works [23–28] have reported diverse schemes of the soliton switching. Despite the theoretical advances, very few experimental studies have been performed for switching of temporal solitons in nonlinear couplers, with results remaining far behind the theoretical predictions. Experimental works exploiting the soliton propagation in dual-core photonic-crystal fibers (PCFs) [29, 30] were hampered by the fission of naturally emerging higher-order solitons, resulting in output distributed chaotically between the two channels [31]. Later, an extensive numerical study for an air–glass dual-core PCF made of a highly nonlinear lead silicate glass (PBG-08) revealed the possibility of self-trapping of higher-order solitons, following their self-compression [32]. Such an effect, which tends to keep a spectrally broadened pulse in one fiber core, was demonstrated in a multichannel fiber structure, as a basis of the creation of "arrayed light bullets" [33]. Motivated by these concepts, we initiated a new study of self-trapping, alternating between the two fiber cores, aiming at achieving high-contrast switching performance. It is focused on the performance of a highly nonlinear DCF with two soft glass kernels. Strong nonlinearity is ensured by using the PBG-08 glass, while the complex air–glass PCF structure is replaced by a low-index glass [34]. The high-index contrast between the core and cladding in this system supports very efficient switching performance, as predicted by simulations [35]. Moreover, a higher level of dual-core symmetry was achieved in this fiber, in comparison to previously used dual-core PCFs, which is necessary for the operation of all-optical switching in DCFs [36].

2.1 Symmetrical dual-core highly nonlinear optical fibers

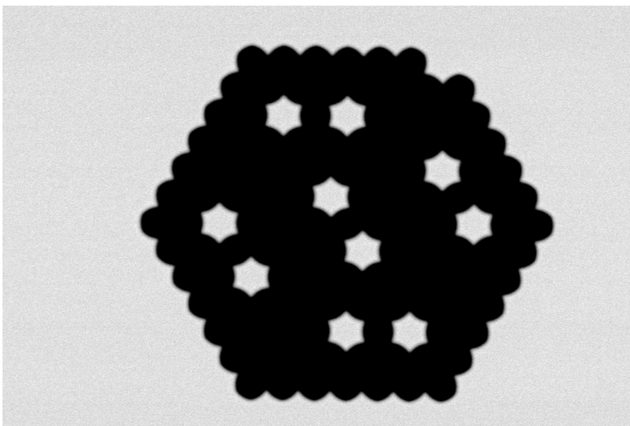

Fig. 2.1: *SEM images of the final fabricated all-solid DCF with simple cladding DCFs with optimal symmetry.*

The fiber's core material was the lead-silicate glass PBG-08, which has been popularly used for all solid nonlinear PCFs. However, it did not exhibit superior switching performance compared to the air-glass PCF. PBG-08 has a high nonlinear refractive index of $4.3 \cdot 10^{-19}$ m^2/W and a linear refractive index of approximately 1.9 in the near-infrared (NIR) spectral region. To achieve better results, a complementary borosilicate glass was developed to match the thermal properties of PBG-08, resulting in the creation of the new glass, UV-710, with a refractive index of around 1.5 in the NIR [37].

Figure 2.2 displays the group refractive index for both glasses in the visible and NIR spectral regions, along with their essential rheological properties. The graph illustrates a significant index contrast of 0.4 between the glasses in the NIR, even during short pulse propagation. The thermal treatment behavior of both glasses is quite similar, allowing them to be combined in the all-solid fiber manufacturing process.

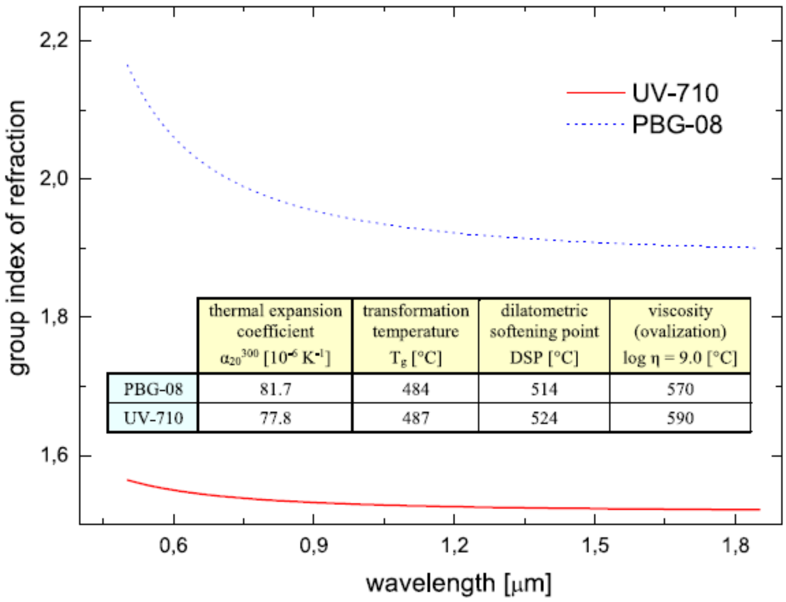

	thermal expansion coefficient α_{20}^{300} [10^{-6} K^{-1}]	transformation temperature T_g [°C]	dilatometric softening point DSP [°C]	viscosity (ovalization) log η = 9.0 [°C]
PBG-08	81.7	484	514	570
UV-710	77.8	487	524	590

Fig. 2.2: *Group refractive index of the two selected glasses and their key rheological properties (in the inserted table) [38].*

The fabrication of the double-clad fiber (DCF) was accomplished using the stack-and-draw method, commonly employed in PCF manufacturing. Initially, cylindrical glass rods of identical diameters were prepared from both glasses: the high-index PBG-08 and the low-index UV-710. The UV-710 glass rods were arranged in a hexagonal lattice structure with 6 rings of elements surrounding the central rod. Subsequently, two UV-710 glass rods flanking the central rod were replaced with PBG-08 ones, and the small air gaps between the rods were filled during the two-step drawing process.

In the first step, several 20-cm long sub-preforms with a diameter of about 1.6 mm were manufactured. After identifying the best symmetry sub-preform, the final drawing process was performed. Before the last drawing process, the sub-preform was enclosed in a capillary of PBG-08 glass to create the outer cladding with a larger diameter, approaching the standard size. The resulting fiber had an outer diameter of 111 μm.

The scanning electron microscope (SEM) images in Fig. 2.1 (a magnification of 5000 and 20,000) show that the core borders did not form the expected regular hexagons, instead taking on a star-like shape. This deformation occurred because the UV-710 glass used for the cladding is harder than the PBG-08 glass used for the core, preserving the original curvature of the cladding rods. The distance between the centers of the DCF cores is 3.1 μm, and the effective mode area A_{eff} of a single core is 1.86 μm^2.

2.2 Experimental results

The pilot experiments in the optimized dual-core-fiber, using pulses of 100 fs duration, with carrier wavelength 1700 nm, have demonstrated, for the first time, high-contrast (16.7 dB) switching in the soliton regime [38]. In this section, we report essentially more advanced experimental results achieved in the C-band (at 1560 nm), using a new generation of strongly nonlinear high-index-contrast DCFs. The experimental findings are supported by simulations that use a model with experimentally relevant parameters.

In the experiment, we used a setup similar to the one in Ref. [38]. The laser source was a Menlo C-fiber amplified oscillator, generating 3 nJ pulses at 1560 nm, with a pulse width of 75 fs, at the frequency of 100 MHz. The output channels of the DCF were monitored sequentially by a CCD camera (ElectroOptic CamIR1550) collecting images recorded at each level of the input pulse energy.

Figure (2.3) presents a sequence of camera images recorded with increasing input energy. These results are similar to the switching performance reported for the 1700 nm carrier wavelength [38], but achieved at lower pulse energies. The switching performance includes back-and-forth switching steps, following the increase in energy, at levels 100–150 pJ and 150–200 pJ, respectively. They correspond to the above-mentioned numerically predicted transitions from oscillations to the trapping in the cross channel, finally followed by the retention in the straight one

The spectrally resolved dual-core extinction ratio, $ER(\lambda)$, was calculated, on the basis of the

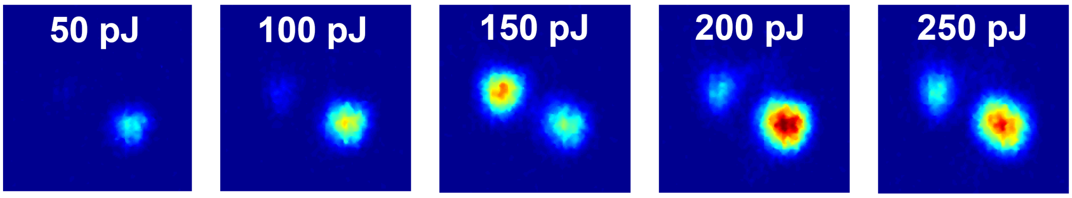

Fig. 2.3: *Camera images sequence of the output pulse for increasing energies of the input.*

experimental data, using power spectra $S_{right}(\lambda)$ and $S_{left}(\lambda)$, which were separately collected from both cores, as following

$$ER(\lambda) \equiv 10\log(S_{right}(\lambda)/S_{left}(\lambda))$$

The dependence of $ER(\lambda)$ on the input pulses energy, E, is shown in Fig.2.4, revealing spectral details of the complex Fig. 3. Sequence of camera images of the output fiber facet for different energies of the input switching behavior, in correspondence with the camera images: at first, $ER(\lambda)$ decreases with the increase in E in the range of 50–150 pJ, then it increases between 150 and 250 pJ. The scenario of the all-optical soliton switching is supported by the fact that only moderate spectral broadening takes place, and the switching is spectrally homogeneous. The same forth-and-back switching scenario is presented by the arrow pairs in Fig. 2.4, spanning in a spectral range of 1510–1575 nm. This range covers the majority of the pulse energy taking into consideration the basic spectral profile presented in the inset in Fig. 2.4. The fourth switching step has lower contrast according to the spectral results comparing the length of the cyan and orange arrows. The origin of this discrepancy is the chromatic aberration of the out-coupling optics avoiding the sharp separation of the two output spectra originating from the straight and cross channels [38], even though the switching performance reveals the possibility of directing the energy to either channel in a reversible way. An essential asset of the operation scheme produced in this work, in theoretical and experimental forms, is that it provides high switching contrasts without the requirement of precise adjustment of the fiber length.

2.3 Theoretical model and simulation results

In Chapter 1, we have derived the coupled nonlinear Schrödinger equations (NLSEs) for directional couplers and several of their solutions in low-power regimes (linear cases). In the higher power regime, where nonlinearity is not negligible, The NLSEs can only be solved numeri-

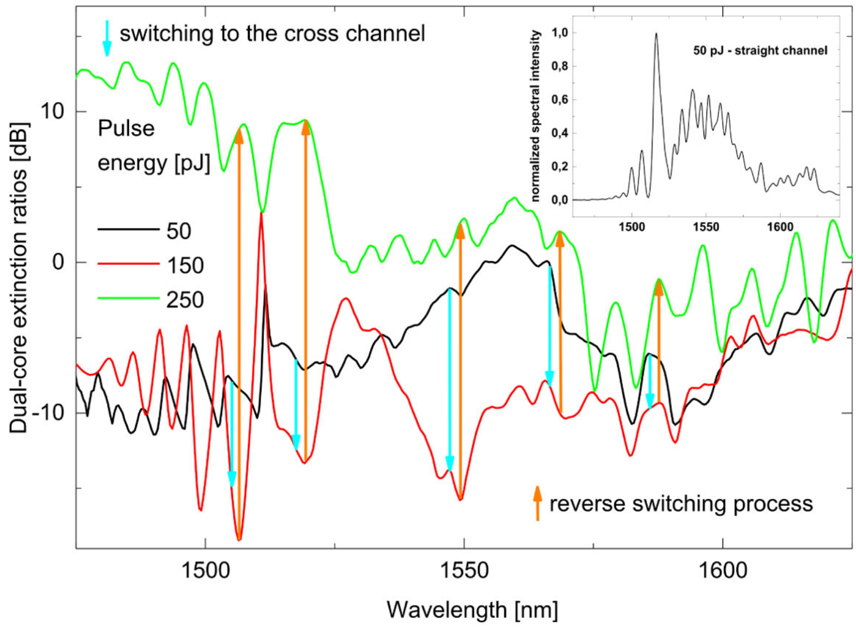

Fig. 2.4: *Spectrally resolved extinction ratio between output intensities in the two channels, measured for different input energies, E. The inset displays the respective spectral intensity for $E = 50$ pJ.*

cally. In this chapter, we will investigate a nonlinear switching mechanism in a dual-core highly nonlinear, high-contrast fiber, which is introduced in Chapter 1, using a model based on the system of NLSEs. The model does not consider another nonlinear effect such as Raman scattering, self-steepening, and higher order GVD effect (cf. Ref. [34]). Thus, the model is based on the system of linearly coupled nonlinear Schrödinger equations (NLSEs) [39–42], written for complex envelopes $A_{1,2}(t, z)$ of electromagnetic waves in the cores:

$$\begin{aligned} i\frac{\partial A_1}{\partial z} &= \frac{-\beta_2}{2}\frac{\partial^2 A_1}{\partial t^2} - \gamma|A_1|^2 A_1 - \kappa A_2, \\ i\frac{\partial A_2}{\partial z} &= \frac{-\beta_2}{2}\frac{\partial^2 A_1}{\partial t^2} - \gamma|A_1|^2 A_2 - \kappa A_1. \end{aligned} \tag{2.1}$$

Where z and t are the propagation distance and time in physical units, respectively. β_2,γ, and κ represent the GVD, Kerr nonlinearity, and inter-core coupling. We define dimensionless parameter for time, distance and amplitude $t = \tau\sqrt{\beta_2/\kappa}$, $z = \zeta/\kappa$, $\psi_{1,2} = \sqrt{\kappa/\gamma}A_{1,2}$. Units of the propagation length and time are $z_0 = \pi/(2\kappa) \approx 21$ mm and $t_0 \approx 32$ fs. The set of Eq. (2.1) in rescaled units becomes:

$$\begin{aligned} i\frac{\partial \psi_1}{\partial \zeta} &= -\frac{1}{2}\frac{\partial^2 \psi_1}{\partial \tau^2} - |\psi_1|^2\psi_1 - \psi_2, \\ i\frac{\partial \psi_2}{\partial \zeta} &= -\frac{1}{2}\frac{\partial^2 \psi_2}{\partial \tau^2} - |\psi_1|^2\psi_2 - \psi_1. \end{aligned} \tag{2.2}$$

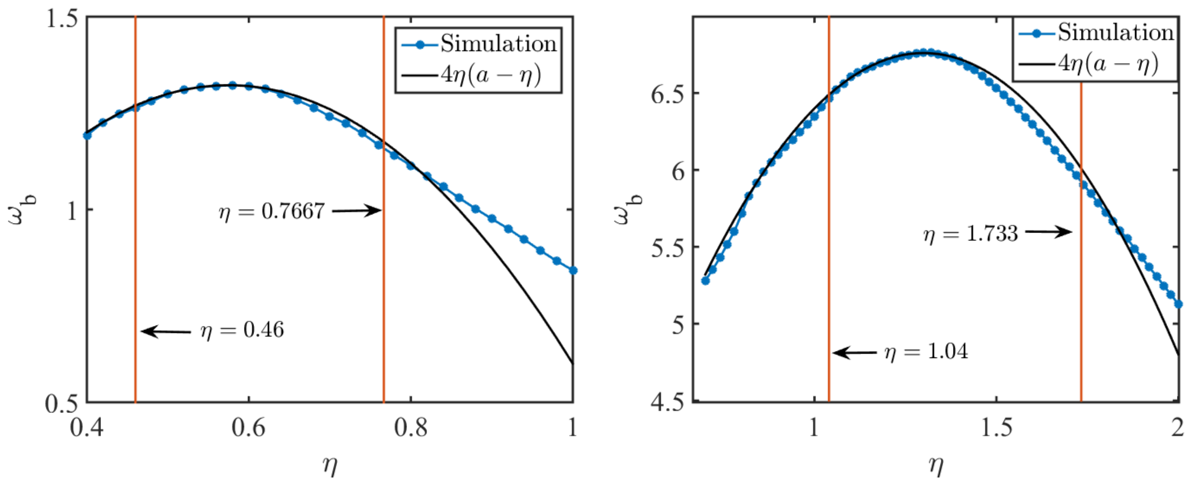

Fig. 2.5: *Frequency of soliton breather as a function of eta for two values of amplitude* $a = 1.15$ *and* $a = 2.6$*. The red lines represent the limits of the interval* $3a/2 < \eta < 5a/2$*, where the formula (1.131) is valid.*

In our simulation of the system, a soliton-like pulse with independent amplitude a and inverse width η was launched in one core, coupled at $\zeta = 0$, and has the form:

$$\begin{aligned} \psi_1(0,\tau) &= a\,\mathrm{sech}(\eta\tau), \\ \psi_2(0,\tau) &= 0. \end{aligned} \tag{2.3}$$

Where the relation of η and FWHM width of the pulse is $t_{FWHM} = 1.76t_0/\eta$. Simulations of Eq. (2.2) were performed using the split-step Fourier method with parameters corresponding to the all-solid 4.3 cm long DCF. The respective parameters, produced by Lumetrical mode solver at wavelength 1.56 μm, are the inverse group velocity $\beta_1 = 6.56 \times 10^{-9}$ s/m, GVD $\beta_2 = -7.73\times 10^{-26}$, inter-core coupling $\kappa = 75\,\mathrm{m}^{-1}$ and nonlinear coefficient $\gamma = 0.4\,\mathrm{W}^{-1}\mathrm{m}^{-1}$ (measured in Ref. [43]). The FWHM width of the pulse is $t_{FWHM} \approx 75$ and $\eta = 0.78$. In Eq. 2.2 the period of the popular oscillation between the cores is π, and the length of the sample approximately equals 3 so switching could be obtained. Relation of energy and scaled amplitude a in equation 2.3 is:

$$E = \frac{\kappa}{\gamma}\int_{-\infty}^{+\infty} |\psi_1(0,\tau)|^2 t_0 d\tau \approx 1.14\frac{a^2 t_{FWHM}\kappa}{\gamma} \approx 30a^2. \tag{2.4}$$

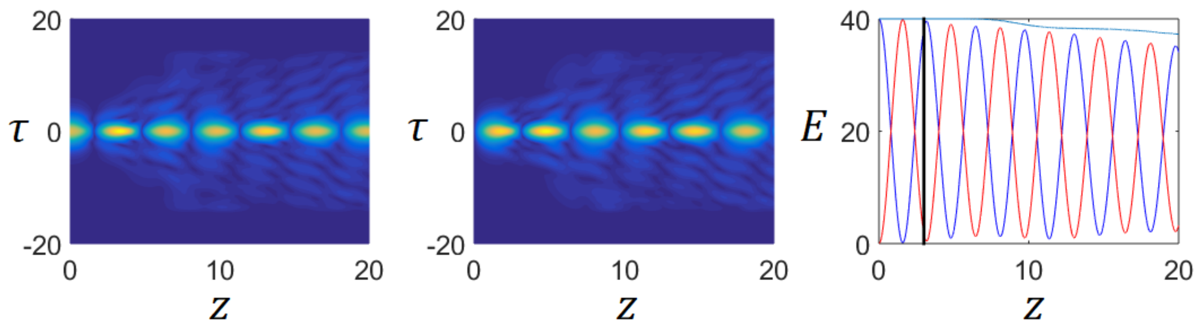

Fig. 2.6: *Periodic inter-core oscillations, produced by numerical solutions of Eqs. (2.2) for the of the input amplitude $a = 1.15$, and inverse width, $\eta = 0.78$. The left and central columns display spatiotemporal patterns of the intensities, $|A_{1,2}(z.t)|^2$, in the bar and cross channels, respectively. The blue and red curves in the right column show the energy in each channel (and the total energy, shown by the cyan curve) versus the propagation distance. The black vertical line at $\zeta = 3$ denotes the length of the fiber corresponding to the experiment.*

2.3.1 Osillation, switching and self-trapping

In the case $\kappa = 0$, the input in Eq. (2.3) only propagates in one core, generating intrinsic oscillations of deform solitons or so-called breathers. Referring to the exact solution of NLSE Eq. (1.115) in Chapter 1, the spatial frequency of these oscillations is given by $\omega = 4(a-\eta)\eta$ when the width of the input pulse falls within the range $3/2 < a/\eta < 5/2$. Figure 2.5 illustrates the breather frequency with respect to η for two amplitude values, as calculated using the above formula and obtained from simulations. Remarkably, the frequency formula and simulation results exhibit agreement within the interval $3/2 < a/\eta < 5/2$. Outside of this range, oscillations still occur, but the correspondence between simulation and approximation formulas cannot be guaranteed. If the coupling parameter κ is greater than zero, it results in the interaction between oscillations inter- and intra-channel oscillations and the emission of small amplitude waves in each channel, mostly at the initial stage of the propagation.

The amplitude of the pulse, which is directly related to the degree of nonlinearity, plays a crucial role in the switching mechanism. When the amplitude is relatively small we observe quasi-harmonic oscillations of energy exchange between the cores. This behavior is due to the stronger inter-core oscillation dominating the weaker intra-core oscillation. Fig. 2.6 shows spatiotemporal patterns in τ and z plane and z-dependent energy for each channel for amplitude $a = 1.15$ from input function (2.3). The right-hand panels depict the slow decay of total energy over long propagation distances, indicated by cyan lines. This decay is primarily due to losses at absorbers placed at the edges of the time-integration domain, simulating the radiation losses observed in the experiment. In the case of $\zeta \approx 3$, which corresponds to a fiber length of 4.3 cm in the experiment, the losses are negligible. By slowly increasing the amplitude of the input, the domination of the linear effect fades away as shown in Fig. 2.8. In the left panel, which corresponds to amplitude is smallest $a = 1$, The dynamics in the two cores are analogous to the linear oscillations with an unchanging period. In the central panel, which corresponds to $a = 1.15$, the inter-core oscillation slightly changes its frequency and decreases the contrast between the two cores. This change is more profound in the case of $a = 1.4$, which is shown in the right panel.

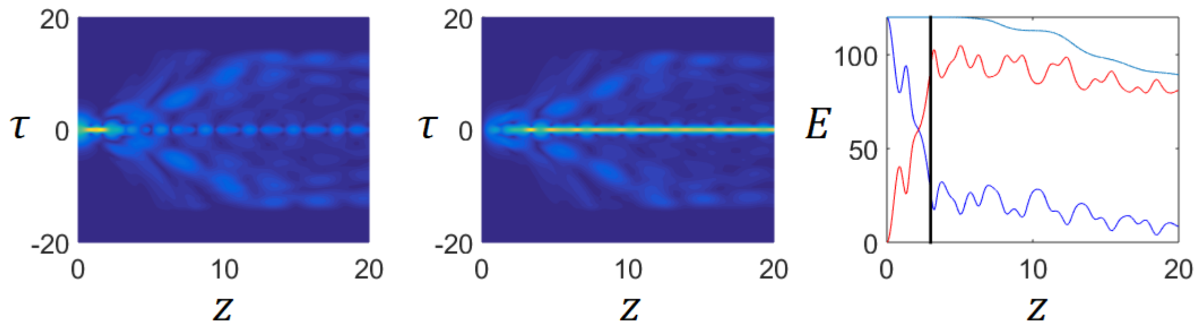

Fig. 2.7: *Self-trapping in the cross channel, produced by numerical solutions of equations (2.2) for the of the input amplitude $a = 2.0$, and inverse width, $\eta = 0.78$. The left and central columns display spatiotemporal patterns of the intensities, $|A_{1,2}(z.t)|^2$, in the bar and cross channels, respectively. The blue and red curves in the right column show the energy in each channel (and the total energy, shown by the cyan curve) versus the propagation distance. The black vertical line at $\zeta = 3$ denotes the length of the fiber corresponding to the experiment.*

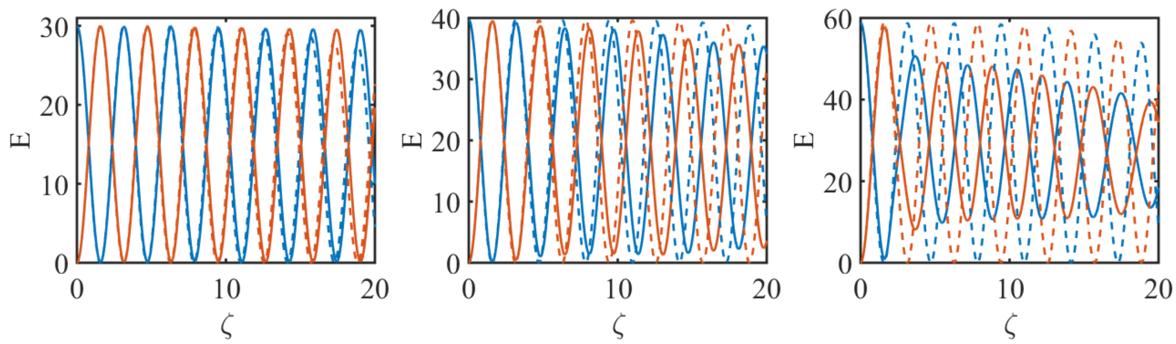

Fig. 2.8: *Comparison of energy in each channel as a function of propagation distance z (solid lines) in the low nonlinear regime, with respect to the energy of linear oscillation (dashed lines). The panels from left to right correspond to $a = 1, 1.15$, and 1.4, respectively.*

However, if we increase the amplitude to $a = 2.0$, the quasi-soliton will switch to the cross channel. The spatiotemporal patterns in τ and z plane and z-dependent energy for each channel for $a = 2$ are shown in figs 2.7. Here, the Kerr nonlinearity overwhelms the linear coupling,

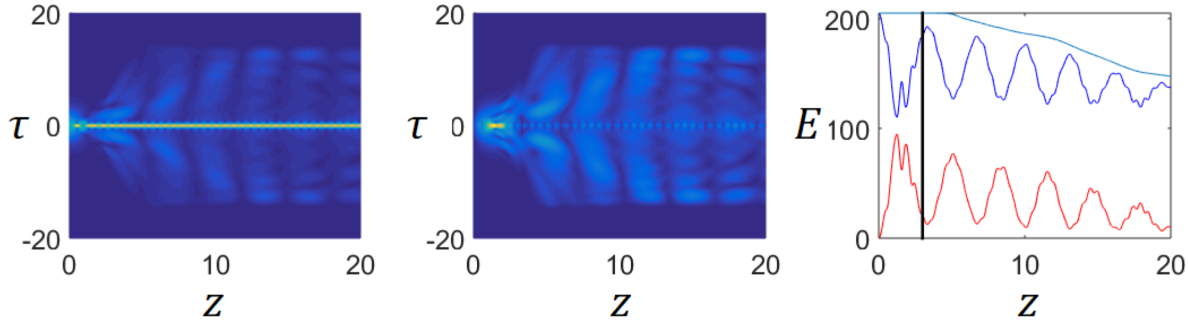

Fig. 2.9: *retention in the cross channel, produced by numerical solutions of equations (2.2) for input amplitude $a = 2.6$, and inverse width, $\eta = 0.78$. The left and central columns display spatiotemporal patterns of the intensities, $|A_{1,2}(z.t)|^2$, in the bar and cross channels, respectively. The blue and red curves in the right column show the energy in each channel (and the total energy, shown by the cyan curve) versus the propagation distance. The black vertical line at $\zeta = 3$ denotes the length of the fiber corresponding to the experiment.*

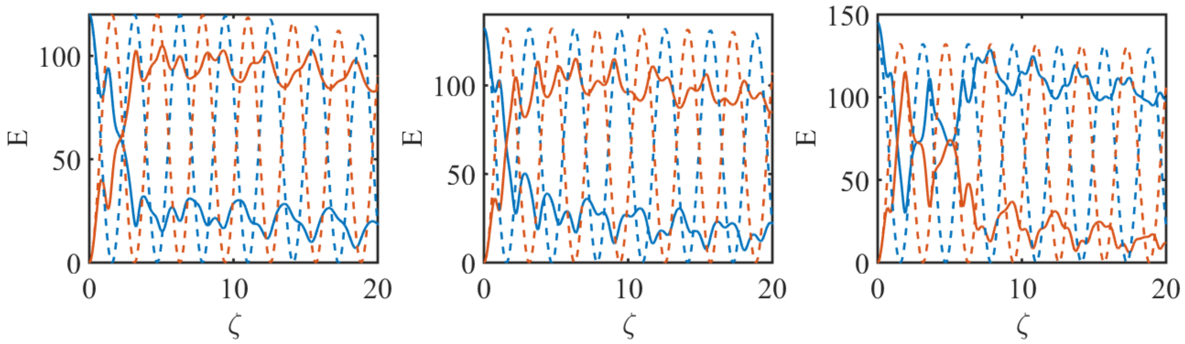

Fig. 2.10: *Comparison of energy in each channel as a function of propagation distance z (solid lines) in the high nonlinear regime, with respect to the energy of linear oscillation (dashed lines). The panels from left to right correspond to $a = 2.0, 2.1$, and 2.2.*

thus inter-core oscillation is becoming weaker than intra-core oscillation. If the amplitude is further increased to $a = 2.6$ or higher, strong nonlinearity ensures that most of the energy remains in the straight channel, while the residual radiation oscillates between the channels. The spatiotemporal patterns in τ and z plane and z-dependent energy for each channel for this case are shown in Fig. 2.9. The inter-cores oscillation is negligible in this scenario. In order to show how fragile the switching/trapping process we did some extra studies (not presented in the paper). We compare the linear oscillation and the dynamics of the system in such high nonlinearity, demonstrated in Fig. 2.10. In this case, the system becomes very fragile and totally different from linear oscillation. However, it seems that the linear effect is still a decisive factor where switching occurs. In the left panel of Fig. 2.10 the switching of energy takes place at exactly one period of linear oscillation. In the right panel, after several oscillations between two cores, with the same period with linear oscillation, the pulse transfers to the cross channel.

2.3.2 The effect of soliton fission

In the simulations presented above, we observe, for higher amplitudes of the pulse, a phenomenon known as soliton fission. Originally this term was used for the breaking-up of femtosecond optical pulse propagating as a high-order soliton into its constituent fundamental soliton due to strong nonlinear effects. We described the dynamics of higher-order solitons in Chapter 1. We stated there that for $N > 2$ solitons exhibit regular oscillations. This refers to solitons in the single channel, described by the single Nonlinear Schrödinger Equation. The main idea behind soliton fission is that when high-order solitons are perturbed by several effects inside optical fibers, including third-order dispersion, self-steepening, and intrapulse Raman scattering, the dynamics become more complicated, and is no longer harmonic. More frequencies appear when soliton breaks into more constituents. In my opinion, this is the main characteristic of soliton fission.

Our system consists of two coupled equations and as we see in Fig 2.10, the dynamics is no longer harmonic, even though higher-order effects are not included. As we show below, the dramatic change of the pulse shape and division into fundamental solitons and anharmonic dynamics may occur for higher-order solitons solely due to the coupling between channels. To show that the temporal shapes of the pulse in the time domain are examined at various propagation distances. The study aims to analyze the effect of linear coupling and nonlinearity on soliton fission and its connection to the self-trapping and switching behavior. Figure 2.11, 2.12, and 2.13 display three sequences of snapshots illustrating the temporal shape of the pulse for input amplitudes of $a = 1.15, 2.0$, and 2.6, respectively. After a short propagation distance, the pulse breaks into smaller side peaks, while the central peak increases in intensity and narrows in width. Subsequently, these smaller peaks, except for the central one, break into even smaller peaks, spreading out along the time axis. The central peak which is the major part of the pulse also either oscillates between the two cores, self-trapping in bar-core, or switching to cross-core. We observed that soliton fission occurs earlier with stronger narrowing and intensification of the central peak as the amplitude of the input pulse is increased, even by a small amount. As a result, when the peak intensity surpasses the critical point, the pulse is trapped in the current channel. The difference between self-trapping in bar-core and switching to cross-core is that, in the latter case, the trapping occurs later because of the lower intensity of the central peak.

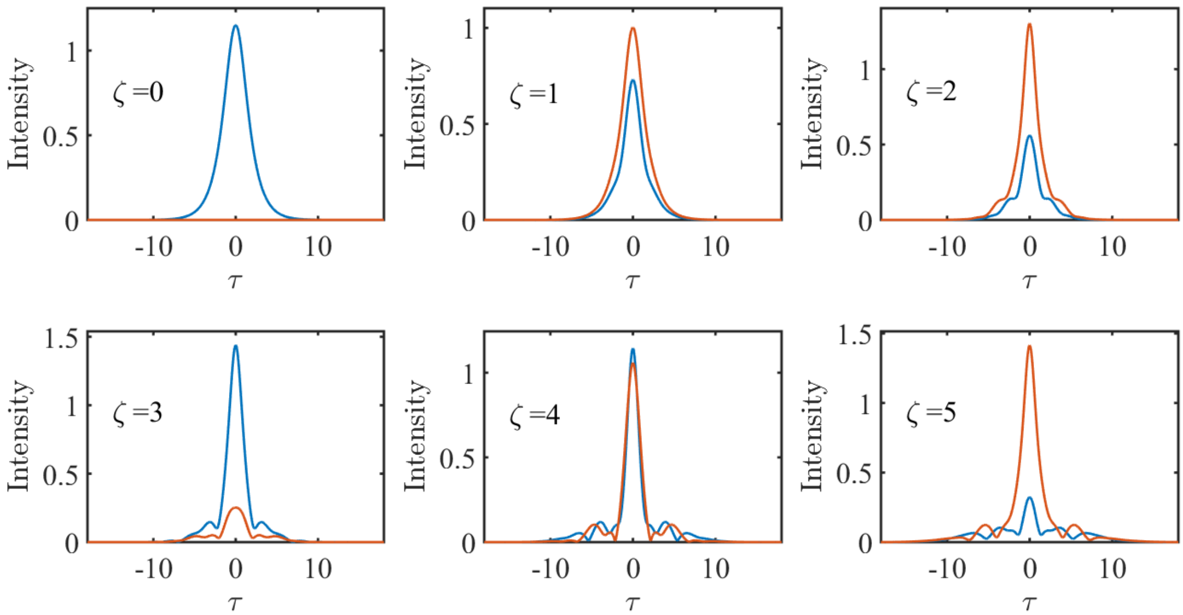

Fig. 2.11: *Snapshots wave function in the time domain at different propagation distances for* $a = 1.15$.

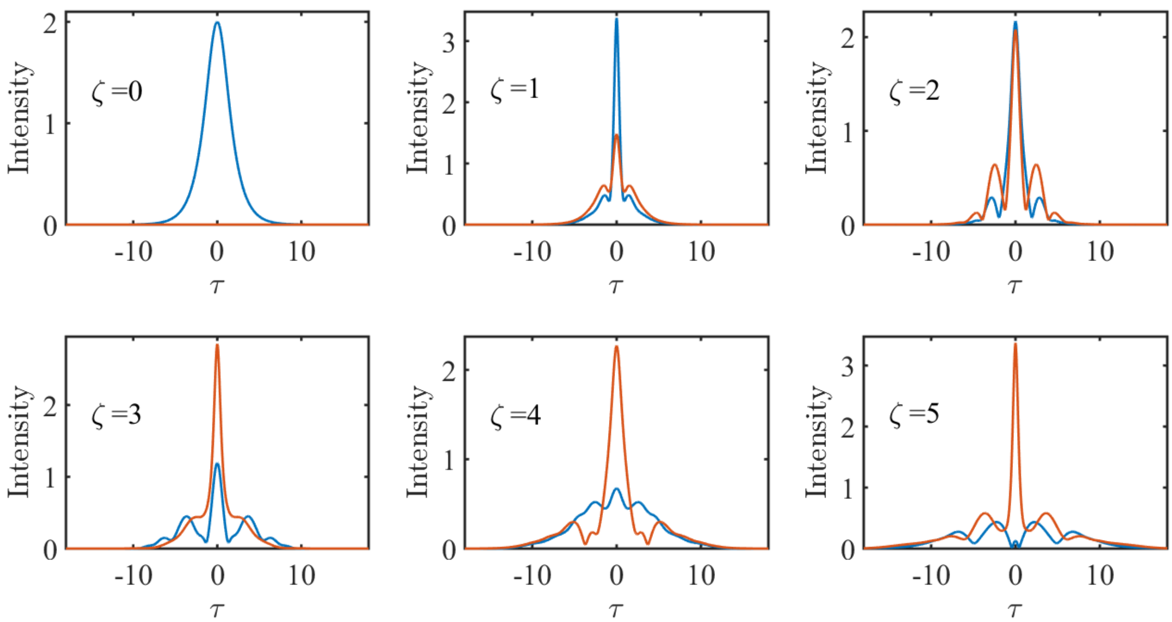

Fig. 2.12: *Snapshots wave function in the time domain at different propagation distances for* $a = 2.0$.

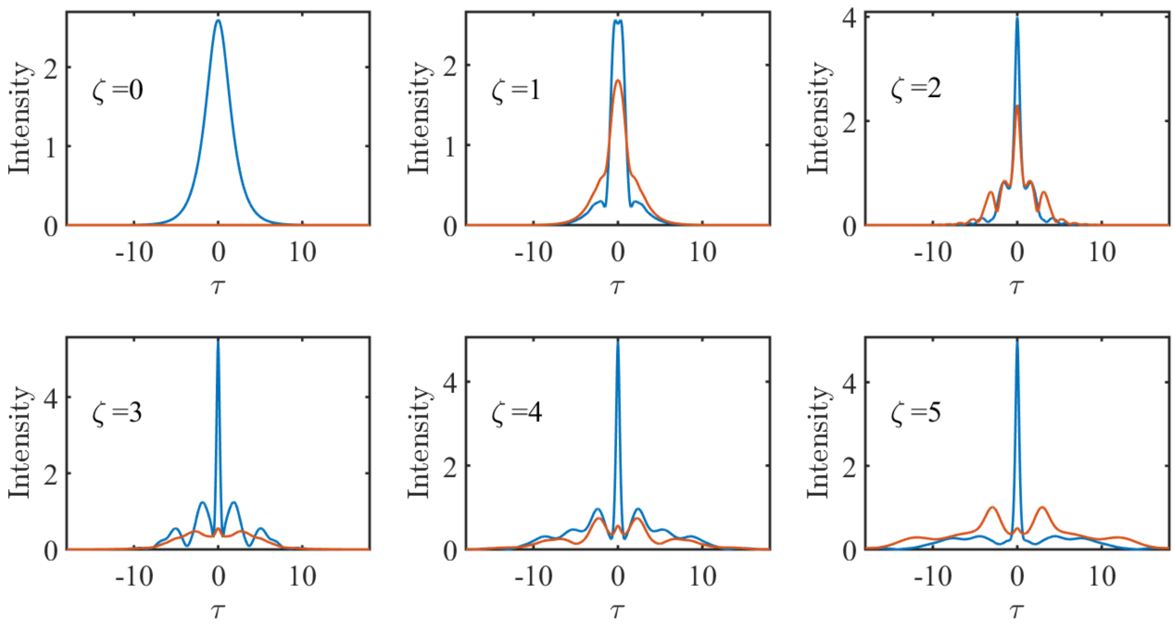

Fig. 2.13: *Snapshots wave function in the time domain at different propagation distances for* $a = 2.6$.

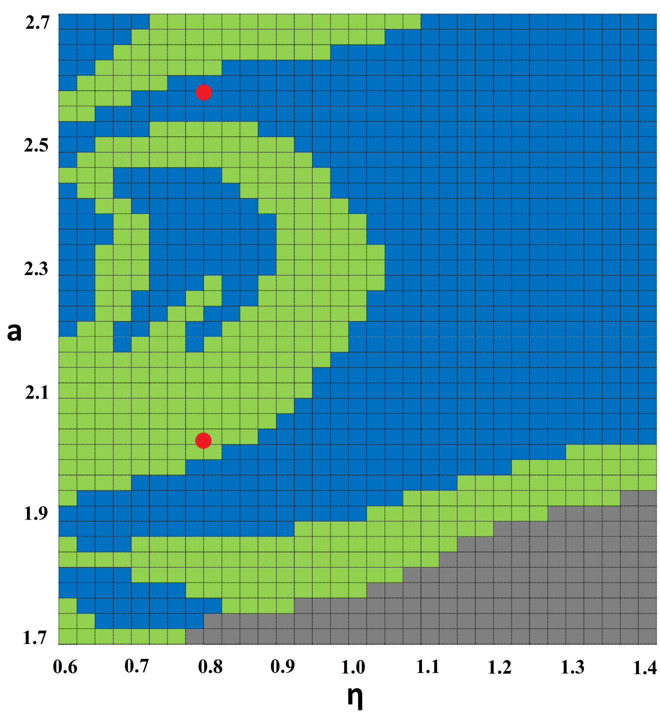

Fig. 2.14: *Chart of dynamical regimes of the system in the* (η, a)*plane, created by numerical solutions of of Eq. (2.2) with input in Eq. (2.3). Gray, green, and blue areas represent inter-core oscillations, switching into the cross channel, and trapping in the straight one, respectively. Red circles refer to the two bottom rows in Fig. 2.1. The top row falls in the gray area beneath the frame of the chart.*

2.3.3 Regions of the three outcomes of the dynamics

Finally, we systematically investigate the effects of pulse width and amplitude on the dynamics of the system by changing each parameter with small steps (0.02 for η and 0.025 for a). Figure 2.14 summarises the results of simulation in a plane of parameters (η, a) of input in equation 2.3. The chart displays three outcomes: periodic oscillation (gray area); switching into the cross channel (green area) and self-trapping in the straight one (blue). For $\eta < 1$, the increase of a exhibits a simple trend for the transition of oscillation to switching, followed by the transition to self-trapping in the straight channel. For $\eta > 1$, varying amplitude a we cross several borders between regions corresponding to the self-trapping in the cross and straight channels. This complex structure exists due to the fact that, in the course of self-compression, the initial pulse keeps oscillating between the channels, while the self-trapping occurs only if the soliton acquires a sufficiently high peak intensity. The pulsations persist in the course of several periods due to the interplay between the single-channel breathing of the deformed soliton and inter-core oscillations.

To summarize the comparison between the numerical and experimental results presented above, we note that the three values of the pulse's amplitude in Eq. (2.3), $a = 1.15, 2$, and 2.6, which give rise to the different outcomes of the transmission through the DCF presented in Figs. 2.6, 2.7 and 2.9 (quasi-linear oscillations, self-trapping in the cross channel, and retention in the straight one), correspond, in physical units, to incident pulse energies 40, 120, and 205 pJ, respectively. The numerical results, obtained for this set of values of the energy correspond precisely to the experimental results observed for energies 50, 150, and 250 pJ, which differ from their theoretical counterparts by a constant factor, ≈ 1.25. Additional effects, such as third-order GVD and Raman effects [16], account for the remaining discrepancy

Losses may also affect the soliton propagation in the DCF. However, limited fiber lengths, for which the current experiments were performed, make dissipative effects a relatively weak perturbation [38]; therefore, they are not included in the theoretical model presented above. In conclusion, the reversible high-contrast switching performance of ultra-fast quasi-solitons in the C-band is demonstrated in the strongly nonlinear DCF made of soft glass. Both experimental and numerical results reveal three different scenarios of soliton propagation, viz., periodic oscillations, self-trapping in the cross channel, and self-trapping in the straight one, depending on the energy of the incident pulse. The experimentally observed scenarios and transitions among them are predicted by systematic simulations of the system of coupled NLSEs. The results may be summarized as a well-defined forth-and reverse soliton-switching effect, controlled by the monotonous increase in the pulse's energy. Such a sub-nano joule high contrast switching protocol may find applications to the design of all-optical signal-processing setups.

Chapter 3

Self-trapping and switching in asymmetrical dual-core highly nonlinear fibers

Here we investigate experimentally and theoretically the effects of the inter-core propagation mismatch on nonlinear switching in dual-core high-index-contrast soft-glass optical fibers. Incident femtosecond pulses of various energy are fed into a single ("straight") core, to identify transitions between different dynamical regimes, viz., inter-core oscillations, self-trapping in the cross core, and retaining the pulse in the straight core. The transfer between channels, which has a solitonic character, is controlled by the pulse's energy. A model based on the system of coupled nonlinear Schrödinger equations reveals the effect of the mismatch parameter and pulse duration on the diagram of the various energy-dependent dynamical regimes. Optimal values of the mismatch and pulse width, which ensure stable performance of the nonlinear switching, are identified. The theoretical predictions are in agreement with the experimental findings.

In Chapter 2, the exchangeable self-trapping in both cores is the key mechanism in the studied dynamical regimes, which could be simulated using a relatively simple model. However, the role of asymmetry of the dual-core structure was not investigated experimentally or theoretically. In the third chapter of the thesis, we consider optical couplers with two cores, but they are not identical. The asymmetry can be caused for example by the difference in effective refractive index. For simulations, we use the set of linearly coupled nonlinear Schrödinger equations (NLSEs) written for complex envelopes $A(z, t)$ of electromagnetic waves. In the mismatched cores of the DCF, it read:

$$\frac{\partial A_1}{\partial z} = -\beta_{11}\frac{\partial A_1}{\partial t} - \frac{i\beta_2}{2}\frac{\partial^2 A_1}{\partial t^2} + i\delta A_1 + i\gamma|A_1|^2 A_1 + i\kappa_{12}^0 A_2 - \kappa_{12}^1\frac{\partial A_2}{\partial t} \tag{3.1}$$

$$\frac{\partial A_2}{\partial z} = -\beta_{11}\frac{\partial A_2}{\partial t} - \frac{i\beta_2}{2}\frac{\partial^2 A_2}{\partial t^2} - i\delta A_2 + i\gamma|A_1|^2 A_2 + i\kappa_{21}^0 A_1 - \kappa_{21}^1\frac{\partial A_1}{\partial t} \tag{3.2}$$

All coefficients were evaluated at central frequency ω_0 corresponding to the wavelength $\lambda_0 = 1700$ nm of the excitation pulses for the specific fiber employed in our experimental study, using a mode solver from Lumerical. The two fiber cores have a nearly hexagonal shape, with the 3.1 μm distance between their centers and the effective mode area of 1.66 $\mu\mathrm{m}^2$ at 1700 nm [44]. The frequency-independent coupling coefficients κ_{12}^0 and κ_{21}^0 are, respectively:

$$\kappa_{12}^0 = \frac{2\pi^2}{\lambda_0^2\beta}\int\int_{-\infty}^{\infty}(n^2 - n_1^2)F_1^* F_2 dxdy, \tag{3.3}$$

$$\kappa_{21}^0 = \frac{2\pi^2}{\lambda_0^2\beta}\int\int_{-\infty}^{\infty}(n^2 - n_2^2)F_2^* F_1 dxdy. \tag{3.4}$$

where functions $F_1(x, y)$ and $F_2(x, y)$ are field-distribution profiles of fundamental modes in each core, subject to the normalized conditions,

$$\int\int_{-\infty}^{\infty}|F_1(x, y)|^2 dxdy = \int\int_{-\infty}^{\infty}|F_2(x, y)|^2 dxdy = 1,$$

κ_{21}^0 and κ_{12}^0 are the first-order expansion of the frequency dependent coupling coefficient κ (coupling dispersion), n_1 and n_2 are refractive indices of the two cores and $n(x, y)$ is the refractive-index profile of the DCF [1]. In our case, the refractive indices of both cores are identical (the PBG08 glass was used as the core material, with $n_{1,2} = 1.9$), while the asymmetry is underlined by a difference in the shapes of the cores. Beyond the core, the refractive index is uniform, corresponding to the cladding material, *viz.*, UV710 glass ($n = 1.52$). The asymmetry parameter is

$$\delta = \frac{1}{2}(\beta_{01} - \beta_{02}) \tag{3.5}$$

where β_{0m} are propagation constants at λ_0 in the individual channel ($m = 1, 2$). The nonlinear Kerr coefficients are:

$$\gamma_m = \frac{2\pi\widetilde{n}_2}{\lambda_0}\int\int_{-\infty}^{\infty}|F_m(x, y)|^4 dxdy \tag{3.6}$$

where $\widetilde{n}_2 = 4.3 \times 10^{-19}$ m^2/W is the nonlinear index of refraction of the PBG08 glass used as the core material, which is about 20 times higher than in silica.

3.1 Rescaling the physical parameters

In the simulations, we used re-scaled parameters and noticed that in our fiber differences between the cores in terms of the coupling coefficients are negligible, therefore: $\kappa_{12}^{0,1} \approx \kappa_{21}^{0,1} = \kappa_{0,1}$. We define dimensionless parameters for time, distance, and amplitude in the same fashion as the previous Chapter, and cast Eqs. (3.1)-(3.2) in the following form (notice that we have defined unit of time t_0 and unit of length z_0, which will later be related to the pulse duration and propagation length):

$$-i\frac{\partial\psi_1}{\partial\zeta} = i\epsilon\frac{\partial\psi_2}{\partial T} - i(\alpha_2-\alpha_1)\frac{\partial\psi_1}{\partial T} + \frac{1}{2}\frac{\partial^2\psi_1}{\partial T^2} + \sigma\psi_1 + |\psi_1|^2\psi_1 + \psi_2, \tag{3.7}$$

$$-i\frac{\partial\psi_2}{\partial\zeta} = i\epsilon\frac{\partial\psi_1}{\partial T} + \frac{\alpha}{2}\frac{\partial^2\psi_2}{\partial T^2} - \sigma\psi_2 + |\psi_2|^2\psi_2 + \psi_1. \tag{3.8}$$

where $\alpha_1 = \beta_{11}/\sqrt{\kappa_0|\beta_{21}|}$, $\alpha_2 = \beta_{12}/\sqrt{\kappa_0|\beta_{21}|}$, $\alpha = |\beta_{22}|/|\beta_{21}|$, $\epsilon = \kappa_1/\sqrt{\kappa_0|\beta_{21}|}$, and the mismatched parameter: $\sigma = (\beta_{01}-\beta_{02})/(2\kappa_0)$ and we used the retarded time $T = \tau - \alpha_2\zeta$. Using the values reported in Table 3.1 $\alpha_1 = 656.0245871$, $\alpha_2 = 656.0485128$, $\epsilon = -0.01492$. The last parameter which is related to the dispersive character of the coupling coefficient is crucial for pulse propagation dynamics.

Table 3.1: *Optical parameters of the dual-core fiber, which were utilized for the numerical study of the nonlinear propagation. The parameters, corresponding to the fiber used in the experiment, were produced with the help of the mode-solver at the carrier wavelength of* 1700 *nm.*

Physical quantity	1st core	2nd core	Units
n_{eff}	1.77766	1.77719	
β_0	6.56172×10^6	6.55996×10^6	1/m
β_1	6.58061×10^{-9}	6.58085×10^{-9}	s/m
β_2	$-9.886149 \times 10^{-26}$	$-9.886149 \times 10^{-26}$	s^2/m
γ	0.85338	0.85584	1/(W.m)
κ_0	1017.8058	1017.8058	1/m
κ_1	-1.49662×10^{-13}	$-1.49662 \times 10^{-13}.$	s/m

Due to the small difference between the GVD and nonlinearity in both cores, average values were used for the numerical modeling, *viz.*, $\beta_2 = -9.886149 \times 10^{-26}$ s^{2}m^{-1}, $\gamma = 0.85461$

$\mathrm{W}^{-1}\mathrm{m}^{-1}$ and $\alpha = 1$. The negative value of β_2 means anomalous GVD of the fiber at 1700 nm, hence solitonic propagation may be expected, initiated by the ultrafast excitation pulse in such a highly nonlinear fiber.

We call the core with higher group velocity high-index core, and the one with lower group velocity low-index core. The units of propagation length and time for our experimental conditions can be evaluated to be

$$z_0 = \frac{\pi}{2\kappa} = 1.54\,\mathrm{mm}, \tag{3.9}$$

$$t_0 = \sqrt{|\beta_2|/\kappa} = 9.86\,\mathrm{fs}. \tag{3.10}$$

The length of our fiber in the experiment was about 18 mm, which corresponds to the dimensionless propagation distance of 18.3. It is worth mentioning that, after the completion of full periods of inter-core oscillations in the linear propagation regime, the energy stays in the initially excited core. In particular, the 18 mm propagation length, representing about 6 periods, maintains this effect, as confirmed experimentally by monitoring the field distribution in the area of both cores at the output.

The asymmetry parameter σ plays an important role in the dynamics of the pulse propagation in the fiber. Considering the difference between the optical parameters of the two cores presented in Table (3.1), it is obvious that the most "influential" coefficient is the propagation constant. The group-velocity mismatch, determined by the frequency derivative of β_0, is more than an order of magnitude lower, and the GVD mismatch between the cores is completely negligible. For this reason, the group-velocity difference was fixed, and only $\sigma = (\beta_{01} - \beta_{02})/(2\kappa)$ was varied in the course of the simulations, as it represents the dominant effect of the mismatch. Therefore, in our study, the impact of the asymmetry is investigated by systematically increasing the value of σ from 0, which represents the symmetric coupler without any mismatch. The asymmetry parameter is increased up to the level where the nonlinear switching is still possible, but with lower sensitivity to small changes of the input energy, in terms of the output-port-dominance exchange.

We have also examined the effect of the pulse's shape and concluded that the results are practically the same when sech or Gaussian pulses are used. The pulse-width effect was examined experimentally in the range between 110 and 150 fs, which is sufficiently broad, taking into consideration that the soliton order increases linearly with the increasing width [1]. Careful complex amplitude-phase diagnostics was performed under step-by-step realignment of the setup of the optical parametric amplification (OPA) source to establish the two above-mentioned border values: 110 and 150 fs. For our simulations, we used the input Gaussian pulse

$$\psi(0,\tau) = a \exp\left(-\eta^2\tau^2\right), \tag{3.11}$$

where a is the amplitude of the pulse envelope. From the FWHM definition,

$$\eta\tau = \eta \frac{t_{\mathrm{FWHM}}}{2t_0} = \sqrt{\frac{\ln(2)}{2}} \approx 0.5887 \tag{3.12}$$

it follows that $\eta = 1.1774 t_0/t_{\mathrm{FWHM}}$, hence the respective values of the inverse-width parameter in Eq. (3.11) are $\{\eta(150\,\mathrm{fs}); \eta(110\,\mathrm{fs})\} = \{(11.609/150); (11.609/110)\} = \{0.0774; 0.1055\}$. The energy of the pulse as a function of a and η can be expressed as

$$E = \int_{-\infty}^{+\infty} |A(z,t)|^2 dt = \frac{\kappa t_0}{\gamma}\sqrt{\frac{\pi}{2}}\frac{a^2}{\eta} = 14.739\frac{a^2}{\eta}[\mathrm{pJ}]. \tag{3.13}$$

The experimental work was carried out with the standard setup presented in detail in Refs. [38, 45]. Femtosecond pulses centered at 1700 nm were generated in an OPA pumped by the second harmonics of commercial Yb:KGW laser system (Pharos, Light Conversion) operating at 1 kHz repetition rate. The OPA allowed the tuning of the pulse wavelength in the range of $1500 - 1900$ nm, which is an essential option for studying DCFs with different levels of asymmetry. The propagation-constant mismatch decreases with the increase of the wavelength [36] therefore the DCF sample which featured poor switching performance at 1560 nm was studied in this work, using 1700 nm input pulses. The pulses were guided through a half-wave plate and polarizer representing a tunable attenuator and through a second half-wave plate to set the proper pulse polarization. The in-coupling and out-coupling of the beam were provided by two 40x microscope objectives mounted on 3D-positioners, securing submicron precision. The output of the fiber was monitored by an infrared camera imaging the output facet on its detector surface. Under the single-core excitation, a series of camera images were registered by changing the energy of the excitation pulses in the range of $0.1 - 1.5$ nJ separately for the fast and slowcore excitation. Additionally, the recordings were repeated for different pulse widths achieved by tuning the OPA while simultaneously keeping the central wavelength at 1700 nm.

3.2 Numerical results for nonlinear propagation

3.2.1 The effects of asymmetry and nonlinearity

Let us recall the exact solution (1.172) and, (1.173) of the linearized version of the system, described by Eqs. (1.170s -1.171) for two components chirped Gaussian pulse in the absence of the group velocity mismatch, $\alpha_1 - \alpha_2 = 0$ introduced in Chapter 1. We showed that the dependent of energies of the two components oscillate between the cores according to Eq. (1.176), where asymmetry coefficient σ decrease the oscillation period and hampers the energy transfer between cores. We now introduce a small nonlinearity to the system using Eqs. (3.7 - 3.7) above. Here, the width of the input pulse introduced in Eq. (3.11) is chosen to be $\eta = 1$. We fix the value of the asymmetry coefficient at $\sigma = 1$ and change the amplitude of the input pulse $a = 1.2, 1.5, 1.9$ and 2.0. The normalized $\zeta-$dependent energies in the two cores are numerically calculated and shown in Fig. 3.1.

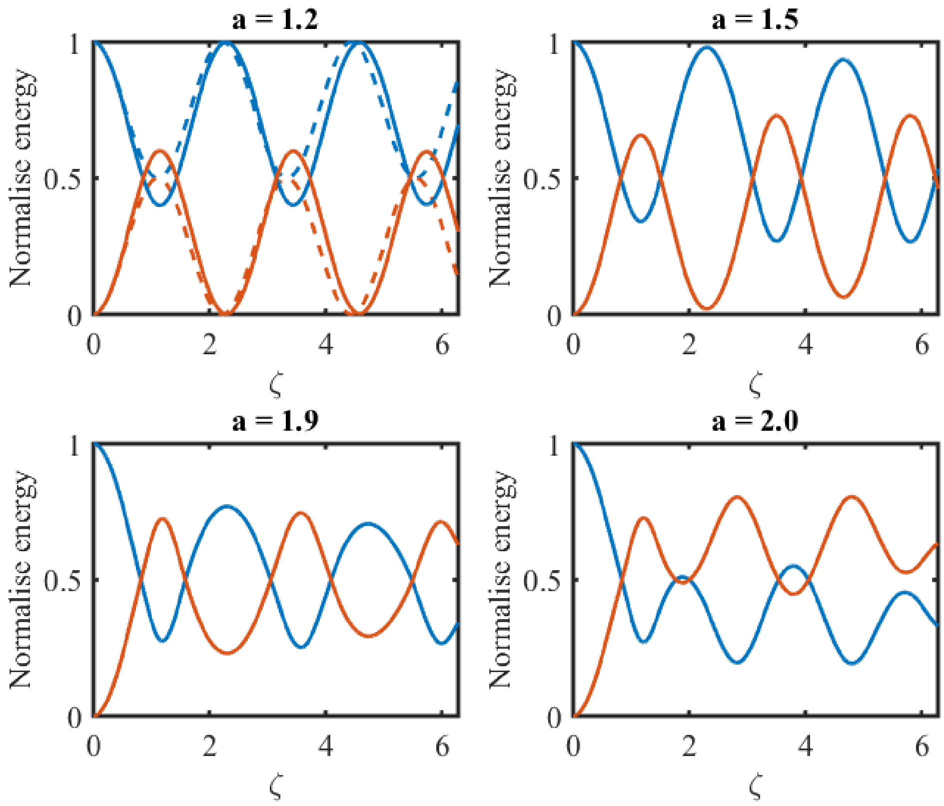

Fig. 3.1: *Energy in first and second cores for $\sigma = 1$ and four values of amplitude a when a pulse with initial form $\mathrm{sech}(\eta\tau)$ is launched in one core at $z = 0$. The dashed lines in the first panel represent dynamics on the linear system with the same asymmetry.*

When the amplitude of the wave is low ($a = 1.2$), the energies undergo oscillations within each core during propagation but predominantly remain concentrated in the excited core, resembling the behavior seen in the linear case. As the amplitude a increases, the energy transfer rises and we observe more oscillations between the two cores, peaking at $a = 1.9$. However, this oscillation at its peak only obtains to more than 50% energy transfer. In comparison with symmetrical linear oscillation, it has a lower contrast between the two cores. This correlation between amplitude and energy transfer arises because the amplitude is directly linked to the intensity $|\psi|$, serving as a balancing factor to minimize asymmetry and reduce the effects of self-trapping. However, due to the oscillation, the magnitude of ψ undergoes variation during propagation and is not uniformly distributed in the time domain, preventing this energy transfer can reaching 100% efficiency, which is possible in linearized cases without mismatch. At higher amplitudes, the oscillation is started to be replaced by switching, where energy is transferred and trapped into the bar core.

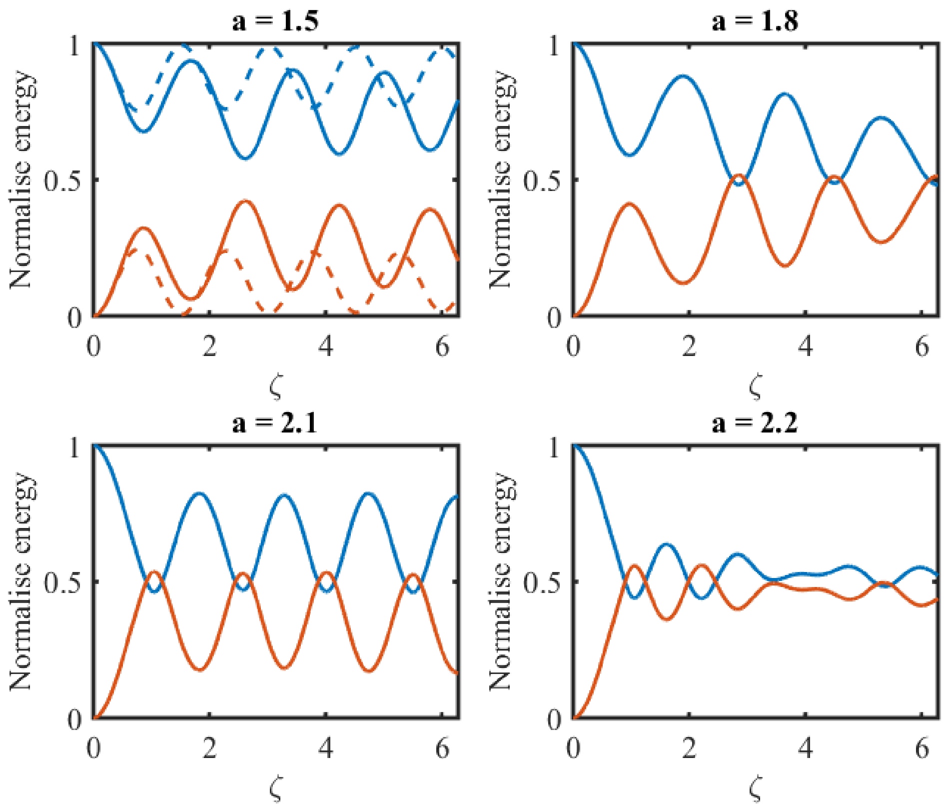

Fig. 3.2: *Energy in first and second cores for $\sigma = 2$ and 4 of amplitude a when a pulse with initial form $\mathrm{sech}(\eta\tau)$ is launched in one core at $z = 0$. The dashed lines in the first panel represent dynamics on a linear system with the same asymmetry.*

Similarly, when $\sigma = 2$, a comparable dynamic change is observed, shown in Fig 3.2. In this situation with a higher value of σ, the initial intra-channel oscillation exhibits a smaller amplitude, and the energy gap between the two cores becomes larger. With an increase in amplitude, the energy gap between the two cores is reduced, leading to significantly lower contrast inter-core oscillation. It seems that, with a fixed value of sigma, the increase of the amplitude within a certain range creates a steady change of dynamics from high contrast intra-core oscillation, to lower contrast inter-core oscillation. At very high amplitude, strong linearity creates higher contrast switching or self-trapping. In this regime, complex layers of switching and self-trapping regions alternate with each other when the amplitude of the pulse is varied. We will investigate these behaviors in the next section.

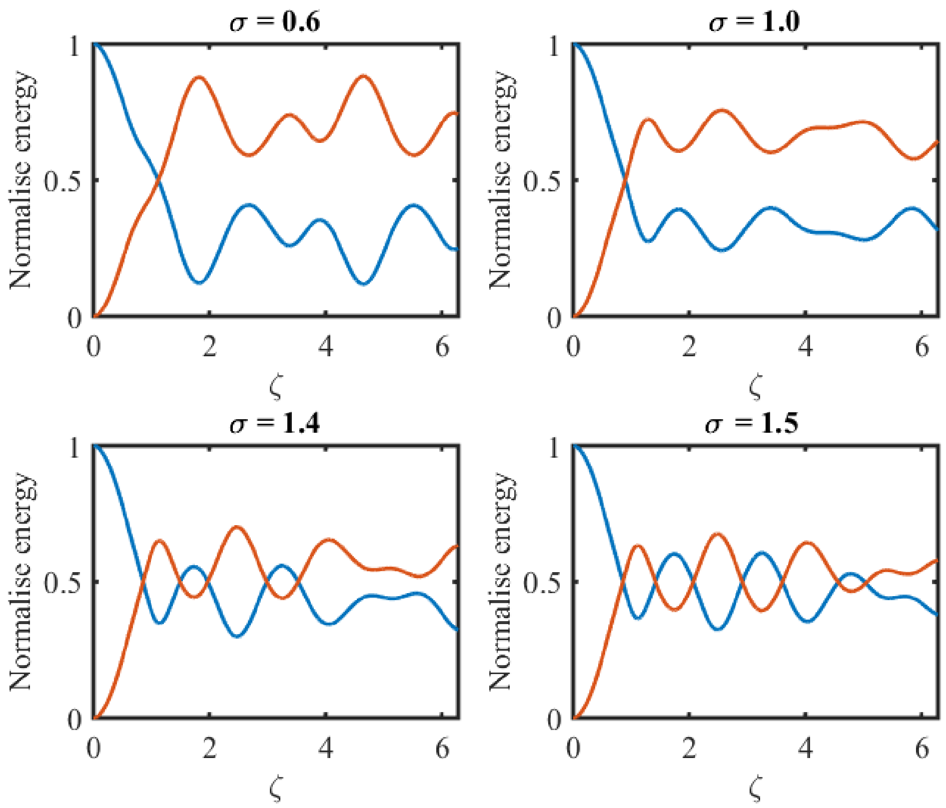

Fig. 3.3: *Energy in first and second cores for* $a = 2.1$ *and 4 values of asymmetry* σ *when a pulse with initial form* $\mathrm{sech}(\eta\tau)$ *is launched in one core at* $z = 0$.

In the subsequent investigation, we maintain a fixed amplitude of $a = 2.1$ while gradually varying the asymmetry value from $\sigma = 0.6$ to 1.5. In Fig 3.3, we present four distinct behaviors of the system resulting from these changes. When the nonlinearity is strong, around $\sigma = 1$, we surpass the range of inter-core oscillation observed in Fig. 3.1 and achieve switching. At lower asymmetry, specifically $\sigma = 0.6$, an even higher contrast is obtained. On the other hand, if we increase the asymmetry greater than 1, this switching becomes less contrast and eventually turns to low contrast inter-core oscillation.

The same trend of dynamic changes is also observed in the scenario where self-trapping occurs at lower asymmetry. The results for $a = 2.4$ with varying values of σ are illustrated in Fig. 3.3. As the asymmetry increases, the energy between the two cores in self-trapping decreases, eventually leading to high-contrast inter-core oscillation.

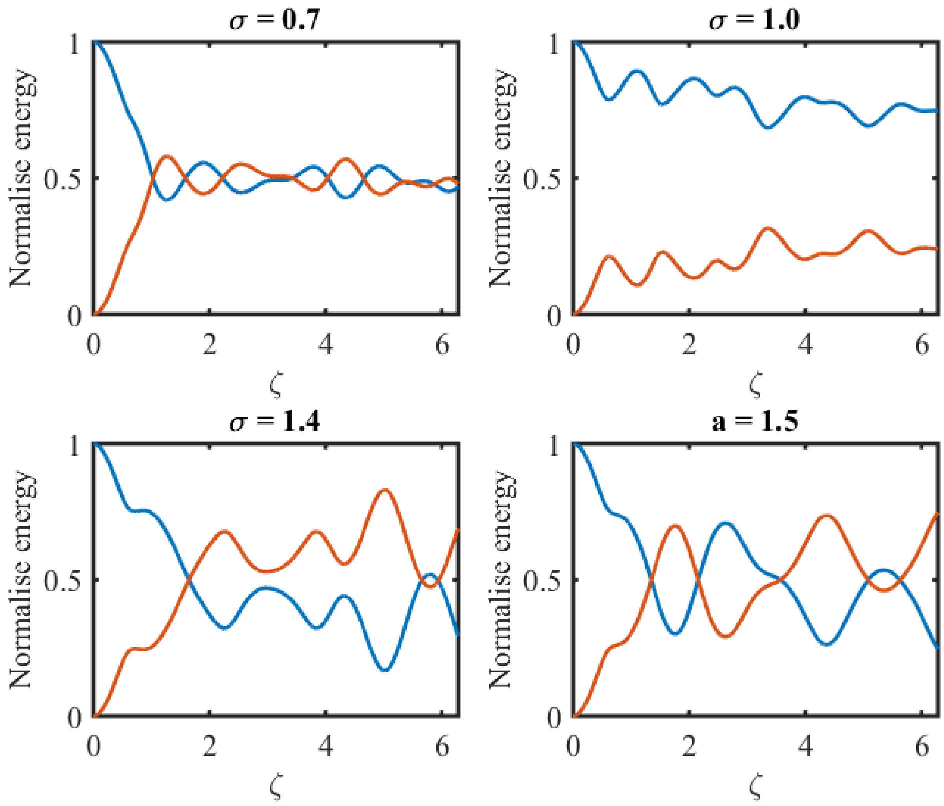

Fig. 3.4: *Energy in first and second cores for $a = 2.4$ and 4 values of asymmetry σ when a pulse with initial form $\operatorname{sech}(\eta\tau)$ is launched in one core at $z = 0$.*

3.2.2 Simulation with experimental data

The analytical solution of phase shift (1.3.4), derived from linearized equation (1.170-1.171) has predicted the reduced coupling efficiency with decreasing excitation wavelength. In correspondence to work done by L. Curilla *et al.* [36] the same effect was observed, therefore we performed the experimental study at 1700 nm instead of 1560 nm. Taking into consideration the positive value of $\Delta\lambda$ tuning the wavelength from 1700 to 1560 nm and the negative value of group velocity mismatch $\alpha_1 - \alpha_2$, the shorter wavelength excitation causes reduced coupling efficiency.

In numerical simulations, we used pulses with two different widths at the FWHM level, 150 and 110 fs to match the experimental data. In the case of the Gaussian pulse, the corresponding values of the inverse pulse width, defined above, were $\eta_1 = 0.077$ and $\eta_2 = 0.11$, respectively. Additionally, we investigated the effect of the mismatch in the effective refractive index to find optimal conditions for controllable switching performance. The propagation distance in the simulations was approximately 25 mm, and since the numerically calculated coupling length was 1.54 mm, it corresponds to about 8 periods of inter-core-coupling oscillations. It provides a possibility for analysis of the nonlinear dual-core propagation even beyond the experimentally studied 18 mm length and puts the findings into a broader context. The simulation parameters (see Table 3.1) were selected from the mode solver analysis of the actual fiber structure. The use of these parameters allows a direct comparison of the numerical results and experimental observations. In the nonlinear simulations, we considered both high-index- and low-index-core excitations, resulting in qualitative agreement with the experimental results in terms of the dependence of the propagation picture on the input energy. However, the considered simple model, which takes into account neither the linear dissipative effects (absorption, Rayleigh scattering) nor nonlinear ones (the stimulated Raman scattering and the generation of dispersive waves), cannot predict precise values of the switching energies. Therefore, when presenting the numerical results, we refer to values of the pulse's amplitude, properly comparing the predictions with the experimental findings.

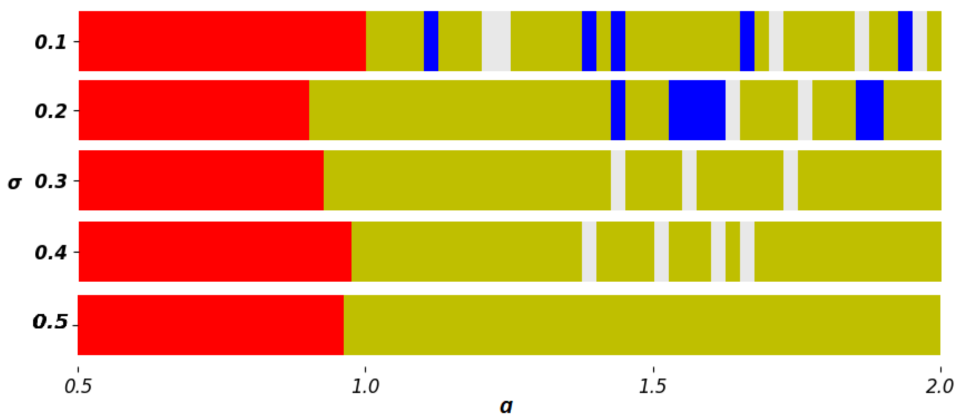

Fig. 3.5: *The pulse amplitude dependence of the dynamical propagation regime of the* 150 *fs Gaussian pulse in the case of the excitation of the low-index core, for different values of the propagation-constant mismatch,* σ*. The red color designates oscillatory behavior, when the final state depends on the actual length of the fiber. Blue means that, after a few initial oscillations, the pulse self-traps mostly in the excited (straight) channel; and yellow means the eventual self-trapping in the initially empty (cross) channel. White stripes were used to mark regions of low contrast, when the signal in both channels is comparable, with small oscillations along the propagation direction.*

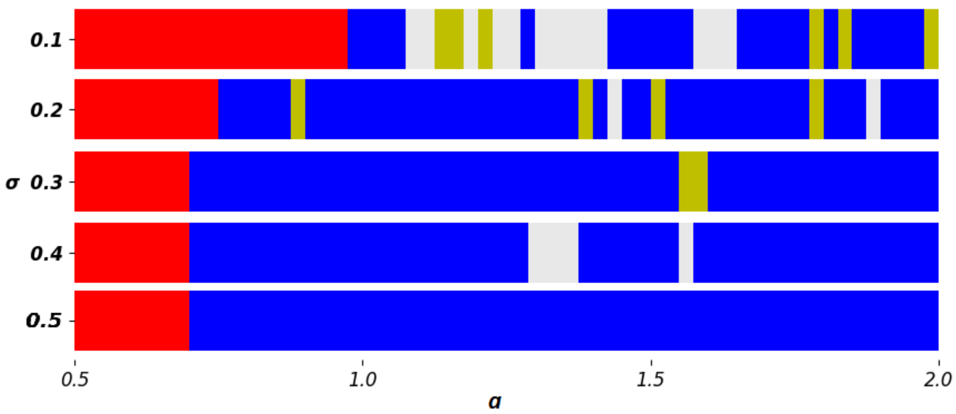

Fig. 3.6: *The pulse amplitude dependence of the dynamical propagation regime of the* 150 *fs Gaussian pulse in the case of the excitation of the high-index core, for different values of the propagation-constant mismatch,* σ*. The meaning of the color code is the same as in Fig. 3.5.*

Preliminary experimental observations imply that introducing core asymmetry may lead to more stable and controllable switching performance (self-trapping of the pulse in the straight, initially populated or the opposite, initially empty channel, depending on the initial pulse amplitude) [45]. To put it in quantitative terms, in our simple model we varied the asymmetry parameter σ from 0.1 to 0.5 for the 150 fs pulse and classified outcomes of the dynamics according to the dependence on the input pulse amplitude. Results are summarized in Figs. 3.5 and 3.6, which represent maps of the nonlinear dynamical scenarios in two cases, when the incident pulse excites either the low- or high-index core. The red color designates oscillatory behavior, when the final state depends on the actual length of the fiber. Blue means that, after a few initial oscillations, the pulse self-traps mostly in the excited (straight) channel; and yellow means the eventual self-trapping in the initially empty (cross) channel. We also marked (with white stripes) cases where we observed low-contrast oscillatory behavior as a function of propagation distance. In the case of launching the pulse into the low-index core, at relatively low mismatch values ($\sigma < 0.3$) we observe several alternations of the pulse trapping between both channels with increasing amplitude. At some amplitudes of input pulses, after a transient distance, the signal becomes almost equally redistributed between two channels, performing low contrast oscillations (white regions). This outcome seems too fragile for the system to be used as an all-optical switch. However, at $\sigma = 0.3$ they are not very frequent and the self-trapping takes place in the initially empty (cross) channel in a broad range of pulse amplitude. Such behavior is quite natural, given the propensity of light to stay in a medium with a higher refractive index. This outcome persists up to the highest analyzed amplitude of the input, i.e. $a = 2.0$, with some exceptions in narrow amplitude regions (white stripes), where equalized energies were predicted comparing the two channels.

In the case of higher mismatch, i.e. $\sigma = 0.4$, similar behavior is predicted, with some equalized dual-core energy distribution situations, but without retaining effect in the excited core. Thus, the low-index core excitation with 150 fs pulse width is not optimal for nonlinear switching performance. In the case of low asymmetry level ($\sigma \leq 0.2$), the system is unstable: there are several transitions between the excited and cross-core self-trapping state with increasing pulse amplitude. On the other hand, the higher asymmetry levels ($\sigma > 0.2$) do not express self-trapping in the excited core; therefore, it does not support the effective nonlinear switching performance.

If the high-index core is initially excited, we again observe, at first, oscillations-straight (excited) channel trapping transition in the region of low energy. When the energy is higher, self-trapping occurs also in the empty (cross) channel. Such switching behavior to the cross-channel takes place in some narrow intervals of values of a (e.g., around 1.6 for the moderate asymmetry, $\sigma = 0.3$, which is shown in Fig. 3.6). Additionally, the trapping threshold decreases when the asymmetry increases. The reason for the latter effect is that the initial asymmetry of the fiber strengthened the trend to self-trapping in the high-index core. The higher the initial asymmetry, the lower the pulse energy is sufficient to induce additional asymmetry (discrete self-focusing in terms of the channels) for establishing the self-trapping process. The yellow-colored areas disappear above $\sigma = 0.3$: only equalized dual-core energy effect is predicted (white stripes) in some narrow amplitude intervals. The reason for this behavior in the case of the highest asymmetry level is that the initial asymmetry already prevents self-trapping in the cross-channel. Therefore, we conclude that 0.3 is the optimal mismatch value for switching in the case of 150 fs pulse width and high index core excitation, with a clear self-trapping effect also in the non-excited channel. Thus we have a robust possibility to control the release of the pulse from a particular output port, regardless of whether the high or low index core is excited.

Analyzing the numerical results, we have concluded that the optimal value of the asymmetry parameter is 0.3 because for higher values of σ the self-trapping in the originally non-excited core is not more predicted. The switching dynamics are different when we excite the low- or high-index-core, with the cross or straight-core self-trapping dominance occurring, respectively, in the former and latter cases. Furthermore, in the case when the fiber length in the experimental realization is equal to a multiple of the inter-core-oscillation period, a different peculiarity is observed in the transition between the inter-core oscillations and self-trapping in the high-index core. As concerns the dominance of the output core, it is preserved in the case of the excitation of the high-index core, and, on the contrary, it is exchanged in the case of the low-index core excitation. In addition to that, the self-trapping may be switched between the two channels in narrow intervals of the initial amplitude, as may be concluded from Figs. 3.5 and 3.6 at low or moderate levels of the phase-velocity mismatch. The overall dynamics seem more stable in comparison to that observed in symmetric or weakly-asymmetric DCF studied before [44], where the diagram of dynamical regimes was more intricate, exhibiting stronger sensitivity to small variations both of the amplitude and pulse width.

3.3 Detailed comparison with experimental observations

Here, we aim to compare predictions of the above theoretical model with the experimental observations made in a nonlinear DCF, with the structure expressing optical parameters presented in Table 3.1, at wavelength 1700 nm. Numerical simulations were performed with parameters matched to the experimental setup, including the wavelength, shape, and duration of the incident pulse.

3.3.1 The core selection effect

In Fig. 3.7 we present the comparison between the theoretical model and experimental registration for the case of the low-index core excitation and the incident Gaussian pulse width $t_{FWHM} = 150$ fs (the top panel of Fig. 3.7). Camera images demonstrate a single exchange of the dominant core around the critical value of the pulse energy of $E = 0.87$ nJ. The simulation results predict the same one-step switching behavior from the inter-core oscillations to self-trapping in the cross-core, which takes place at the amplitude $a = 0.95$. A narrow region of low contrast was predicted around $a = 1.45$, 1.55, and 1.75, and a similar effect is visible from the camera images. The bottom panel of Fig. 3.7 reports the distance-dependent dynamics of the energy distribution in both cores (blue - low-index/bottom core, red - high-index/top core) in the case of 150 fs pulse width and $a = 1.65$. It reveals that the propagation maintains an oscillatory character over the whole analyzed length, with an exponential decrease of the peak power after each period $z/z_0 = 1.65$. It is an example of the disturbing effect of the coupling on the soliton self-trapping mechanism. It takes place when the pulse cannot reach the self-trapping critical

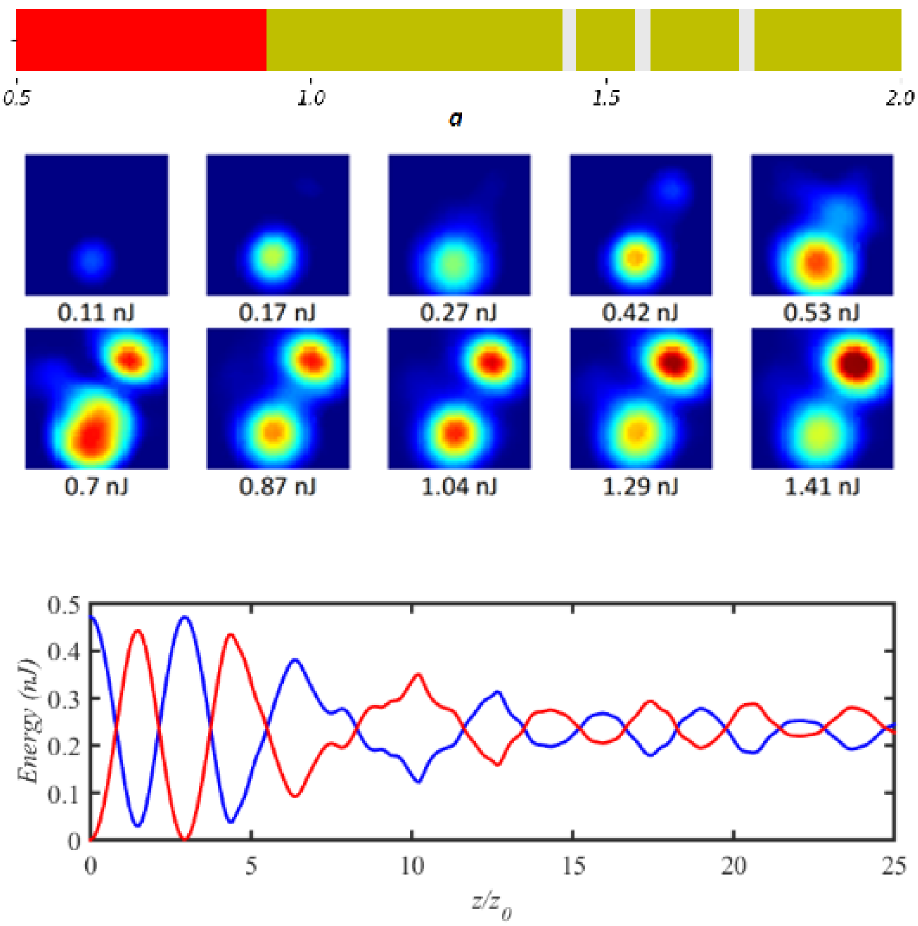

Fig. 3.7: *The comparison between the simulations diagram and experimental registration of the energy-dependent output dual-core field distribution for the case of* 150 *fs Gaussian pulse launched into the low-index core. The bottom figure shows typical dynamics in the low-contrast regions.*

peak power, resulting in equalized field distribution between the two channels during the soliton self-compression process. As a consequence, the self-trapping process doesn't take place and the propagation maintains its harmonic features along the entire considered length. However, such an effect requires a certain ratio between the self-compression distance determined by the pulse amplitude and the coupling. Therefore, a slight tuning of the amplitude below or above the 1.65 level results in a clear self-trapping effect. In the case of the high-index-core excitation, the images of the output fiber facet reveal a different result, viz., transient switching behavior at higher pulse energy, i.e. around 1.26 nJ (Fig. 3.8). Under further increasing of the pulse's energy, the same straight-core dominance was observed as in the linear propagation regime. The simulations predict a similar outcome with the transient cross-core dominance effect around the amplitude level of 1.65.

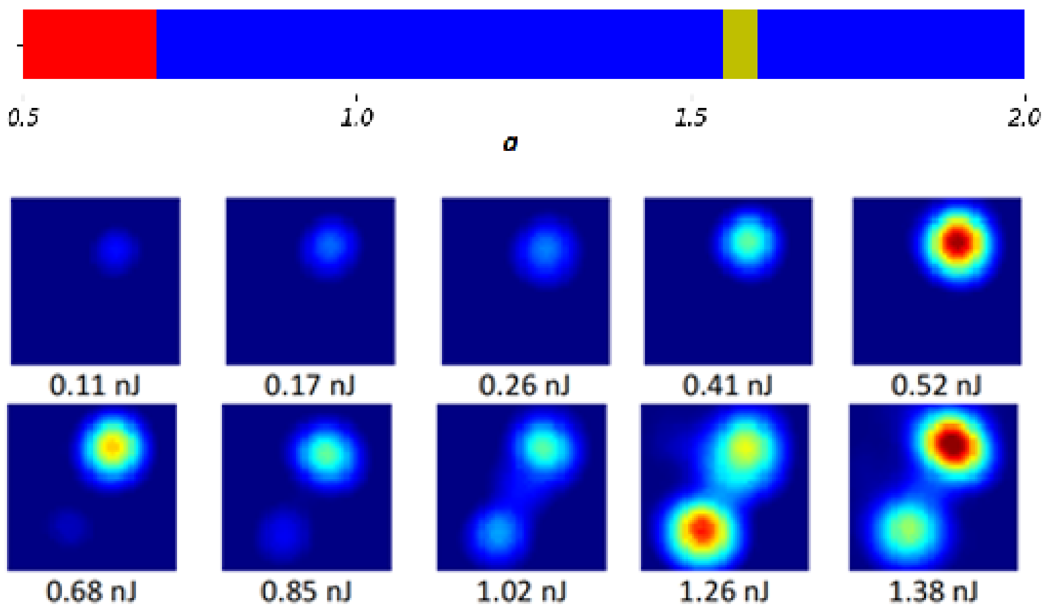

Fig. 3.8: *The comparison between the simulations diagram and experimental registration of the energy-dependent output dual-core field distribution for the case of* 150 *fs Gaussian pulse launched into the high-index core.*

The transition between the oscillatory and straight-core self-trapping, predicted by the simulations at the 0.72 level, is not observable experimentally because it does not change the core dominance in the output, due to the choice of the fiber's length corresponding to an integer number of oscillation periods. Thus, the optimal level of the mismatch parameter identified in the numerical study ($\sigma = 0.3$) predicts a similar switching performance as the experimental observation. It is a signature of the same optimal asymmetry level established in the experiment. It was ensured by tuning the wavelength of the excitation pulses to secure robust switching performance. Indeed, exciting the same DCF by C-band pulses resulted in poor switching performance [46]. However, the 1700 nm excitation improved it significantly; therefore, we set this wavelength also in our numerical analysis.

3.3.2 The pulse-width effect

Figure 3.9 presents the case of the low-index core excitation by pulses with 110 fs pulse width. It shows more sophisticated dynamics than the one in the case of 150 fs pulse width presented in Fig.3.6. It expresses three transitions between the output straight/cross core dominance at pulse energies 0.42 nJ, 0.69 nJ, and 1.03 nJ, considering both the simulation outcomes (top panel) and the experimental results (bottom panel). The numerical results predict transitions around amplitude levels 0.95, 1.8, and 1.95, which resemble the experimental observations with two dominance exchanges. The images in Fig. 3.10 show the corresponding situation when the high-index core is excited with 110 fs pulse (bottom panel) and the predictions of the theoretical model for the same conditions at which the experiments were performed (top panel). The simulations exhibit three transitions: inter-core oscillations to self-trapping in the straight core at amplitude 0.75, then some low contrast lines transition to the straight core self-trapping state around level 1.85, followed by the inverse transition. The latter was not observed in the experiments due to limitations imposed on the pulse input energy, which should be kept below 1.5 nJ in order not to damage the input facet of the fiber. Furthermore, the oscillations to straight core self-trapping transition do not cause any exchange of the dominant core, as in the case of the results obtained for 150 fs pulse width (Fig.3.5). Therefore, from the camera images, one can see that only one straight/cross-core transition is observed at 1.27 nJ, in correspondence to the numerical outcomes. between the inter-core oscillations and self-trapping in the cross-core occurs, at the amplitude 0.95. In contrast, considering both the low and high-index core excitation cases, the 110 fs pulse width causes more complex changes in the pulse energy-dependent dual-core propagation dynamics. The reason for such character in the case of the shorter pulse is the linear decrease of the soliton order N with decreasing pulse width, according to the following equation

$$N^2 = \frac{\gamma P_0 T_0^2}{|\beta_2|}, \tag{3.14}$$

where P_0 is the input pulse peak power and T_0 the pulse width. The lower soliton order in the case of 110 fs pulse width reduces the disturbance of the pulse during the soliton fission process. Thus, the more preserved single pulse character supports more exchanges between the trapped channels with increasing pulse energy. The soliton self-compression effect, characterized by the factor $F_c = 4.1N$ [47] is also more pronounced in the case of longer pulses. Consequently, the stronger selective self-focusing (which favors a particular channel) prohibits the transfer to the straight core at higher pulse amplitudes. Summarizing this sub-chapter, the 110 fs pulse width seems to be more advantageous because it enables high switching contrast between the channels based on self-trapping taking place in both of them. It is governed just by a slight change of the pulse amplitude and it is predicted in the case of both high- and low-index core excitation. The experimental observations confirmed these findings by comparing 110 fs vs. 150 fs pulse excitation and considering both core's excitation.

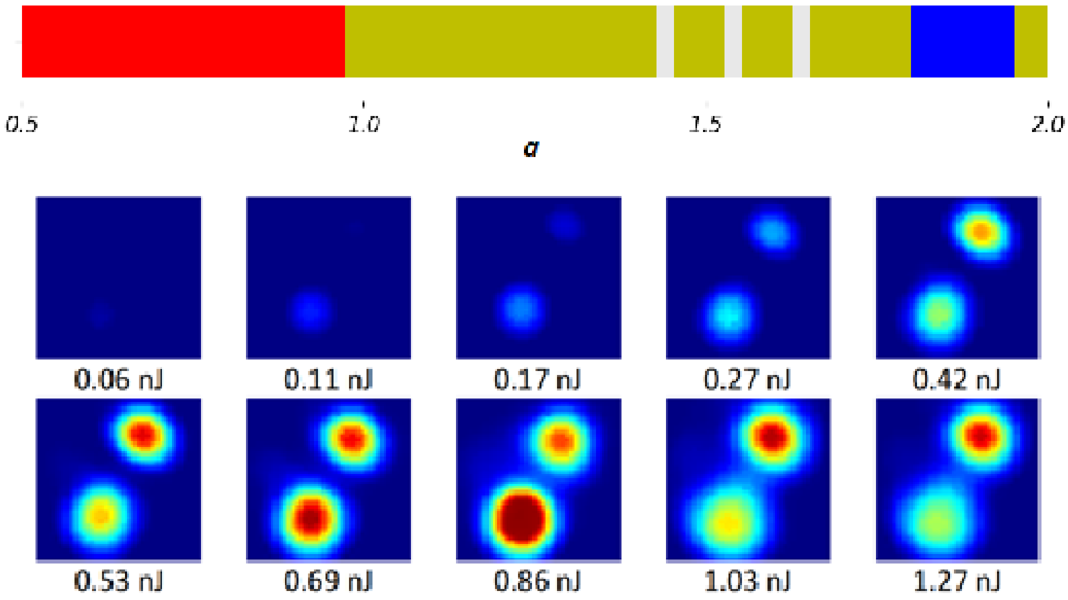

Fig. 3.9: *The comparison between the simulations diagram and experimental registration of the energy-dependent output dual-core field distribution for the case of* 110 *fs Gaussian pulse launched into the low-index core.*

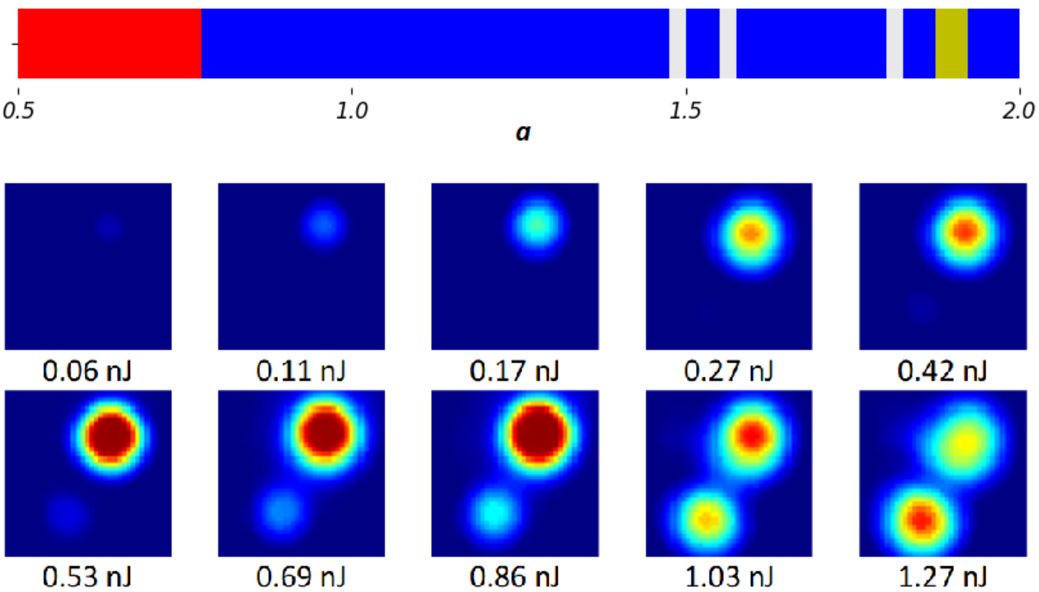

Fig. 3.10: *The comparison between the simulations diagram and experimental registration of the energy-dependent output dual-core field distribution for the case of* 110 *fs Gaussian pulse launched into the high-index core.*

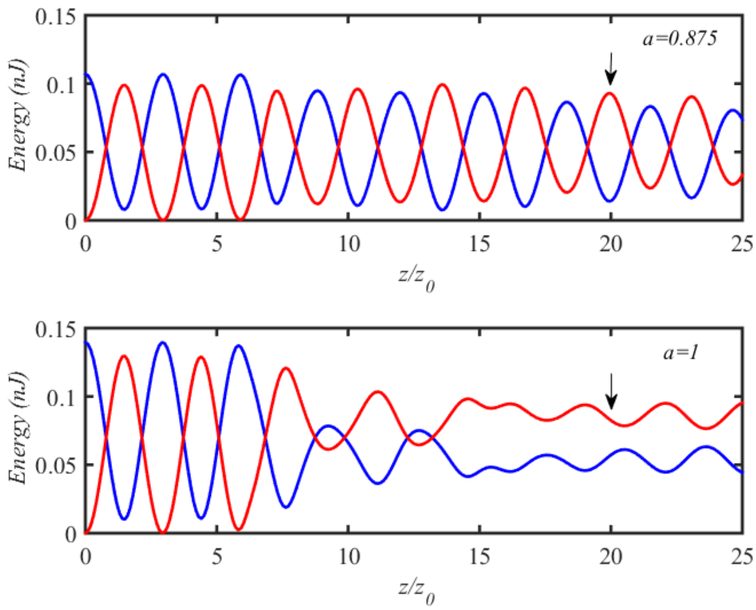

Fig. 3.11: *The dependence of the integral field energy on the propagation distance in both cores, as produced by the simulations. It shows the transition of oscillations to the cross-core self-trapping for the input pulse amplitudes* 0.875 *(the upper panel) and* 1.0 *(the lower panel). Excitation pulses with a width of* 110 *fs and Gaussian shape were launched into the low-index core of the fiber with asymmetry parameter* $\sigma = 0.3$*. The black arrow marks the length of the fiber in the experiment.*

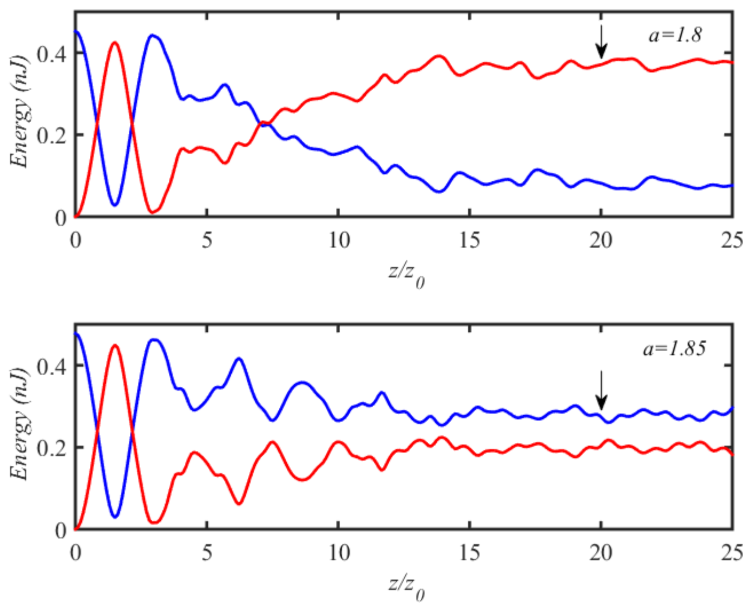

Fig. 3.12: *The dependence of the integral field energy on the propagation distance in both cores, as produced by the simulations. It shows the transition of the trapping from the cross core to the straight one for input pulse amplitudes* 1.8 *(the upper panel) and* 1.85 *(the lower panel). Excitation pulses with a width of* 110 *fs and Gaussian shape were launched into the low-index core of the fiber with asymmetry parameter* $\sigma = 0.3$*.*

Finally, in Figs.3.11-3.13 we illustrate the propagation-distance-dependent distribution in both cores in the case of 110 fs pulse width, which signals the onset of the same sequence of three transitions as observed experimentally (bottom panel of Fig. (3.9). The top panel of Fig. 3.11 reveals that, when nonlinear effects are small at the low amplitude level, the propagation features an oscillatory character in the whole studied propagation range [44]. The harmonic behavior in the propagation evolution graphs with higher pulse amplitudes terminates after a few initial oscillations due to the soliton self-compression and the subsequent self-trapping process [34]. According to our simulations, when the self-trapping commences, the core dominance is preserved in the whole subsequent range of the studied propagation lengths, including the value corresponding to the fiber length in the experiment. Another important aspect of the dual-core field-evolution plots is that they express nearly 100% transfer of the pulse's energy between the cores. It originates from the low level of the propagation constant mismatch parameter, 0.3, which, according to Eq. (1.164) describing various linear propagation approaches causes only a slight modification of the effective coupling constant, hence the coupling period remains similar to that for the zero mismatch. Black arrows indicate the observation point, which corresponds to the fiber length used in the experiment. All three transitions are presented subsequently in Figs. 3.11-3.13 exhibit a clear exchange of the dominant cores following a slight increase of the pulse amplitude between the top and bottom panels. Accordingly, all of them have been identified experimentally by the camera monitoring the output fiber facet, and the corresponding pairs of camera images (0.27 - 0.42 nJ, 0.53 - 0.69 nJ, 0.86 - 1.03 nJ) exhibit convincing switching contrasts. Thus, the experimental observations have confirmed the predictions of the numerical simulations, i.e. the three-transition character of the energy dependence for the 110 fs pulse width, in the case of low-index core excitation.

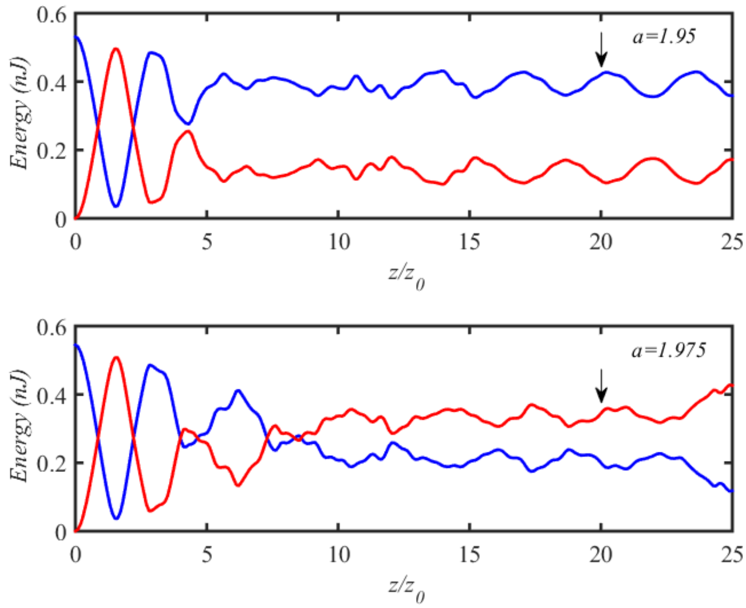

Fig. 3.13: *The dependence of the integral field energy on the propagation distance in both cores, as produced by the simulations. It shows the transition of the trapping from the straight core to the cross one for input pulse amplitudes* 1.95 *(the upper panel) and* 1.975 *(the lower panel). Excitation pulses with a width of* 110 *fs and Gaussian shape were launched into the low-index core of the fiber with asymmetry parameter* $\sigma = 0.3$.

Chapter 4

Control of dual-wavelength switching in asymmetric dual-core fiber

We present a systematically produced experimental and theoretical investigation of dual-wavelength switching of 1560 nm, 75 fs signal pulses (SPs) driven by 1030 nm, 270 fs control pulses (CPs) in a dual-core fiber (DCF). We demonstrate the switching contrast of 31.9 dB at the 14 mm fiber length by in-coupling temporally synchronized CP-SP pairs into the fast core of the DCF with a moderate inter-core asymmetry. A model based on three coupled propagation equations is used to identify the nonlinear compensation of the asymmetry as a physical mechanism behind the efficient switching performance.

In the experimental study in reference [48], it was shown the first evidence of proof of dual-wavelength switching based on the interaction between two temporally synchronized pulses using an all-solid DCF. It is based on a combination of two femtosecond pulses of different wavelengths, simultaneously launched into the same fiber core. A longer wavelength (1560 nm) low energy pulse served as an information carrying signal and the shorter wavelength one (1030 nm) with higher energy was the control pulse. It was demonstrated that using such a temporally synchronized pair of pulses at appropriately adjusted control pulse energy, the intra-channels refractive index mismatch is compensated leading to signal switching from the excited to the non-excited core with negligible distortions. Such an approach is more effective than the simple energy control of one single ultrashort pulse presented in our other works (*self-switching*) [34, 44–46, 49], as it provides balancing the inter-core asymmetry. The latter problem is inherent to DCFs, being a basic limiting factor of high-contrast directional coupler performance. In general, the two cores of a DCF are distinguished as slow and fast ones, with effective refractive indices n_{01} and $n_{02} < n_{01}$, respectively. The motivation for the use of the nonlinear dual-wavelength interaction is that the co-propagating control pulses of appropriate energy reduce the group velocity $v_{\mathrm{g},2}$ of the signal pulses in the excited core in the time window of the control pulse duration to the level of the non-excited core group velocity [48]. An important aspect of this approach is the strong spectral dependence of the coupling length, which prevents the energy transfer of the shorter wavelength CP pulses to the cross core. As a result, the switching contrasts > 25 dB were recorded, exceeding the best experimental results of the self-switching in the C-band [45] and the theoretical predictions of ultrafast solitonic self-trapping in highly nonlinear DCFs [34]. Additionally, we point out that a shorter fiber length of only 14 mm was used, instead of the 35 mm used during the self-switching study at a similar 1550 nm signal wavelength. A complete comparison between the two methods can be found in [50].

Our pilot dual-wavelength switching demonstration showed some drawbacks, mainly the relatively high energies of the control pulses at the level of a few nanojoules. In this Chapter, we present an advanced study, supported also by numerical simulations. We analyzed several DCF samples and optimized simultaneously their length, control pulse energy, and delay between the signal and control pulses. Thanks to these efforts, we reduced the switching energy down to the sub-nanojoule regime preserving the advantageous switching contrast level. Furthermore, we also performed several numerical simulations considering fiber parameters, especially mismatch and higher-order coupling, to investigate their roles in the switching performance of the DCFs.

4.1 Description of the Experiment

We investigated a simple cladding of all-solid DCFs with the cross-section presented in Fig.4.1 (left). The fiber was made with two thermally matched soft glasses (PBG-08 - lead-silicate and UV-710 – borosilicate for cores and cladding, respectively) and expressed a DC asymmetry level of $\delta n_{\mathrm{a}} = 2.2 \times 10^{-4}$ at 1560 nm. It is calculated as the difference between the effective refractive indices of the slow and fast cores $\delta n_{\mathrm{a}} = n_{01} - n_{02}$, respectively. The experimental setup consisted of two laser arms, where two femtosecond pulses with different wavelengths were generated at 10 kHz repetition rate, labeled as control (1030 nm, 270 fs pulse from a commercial ultrafast Yb:KGW amplifier - Pharos, Light Conversion) and signal (1560 nm, 75 fs pulse, generated in a self-made double pass optical parametric amplifier (OPA), pumped by second-harmonic of the same Yb:KGW amplifier). The two pulses were combined by a dichroic mirror and synchronized by a delay line unit positioned in the control arm. The energy and polarization of the control pulses were controlled independently using two half-wave plates separated by a Glan-Taylor polarizer placed between them; however, the control field was selectively filtered out after the fiber by a high reflectance mirror. Thus, only the signal field on the DCF output facet was imaged on the multimode collections fiber of a spectrometer or alternatively on an infrared camera chip tilting a flip mirror into the output beam path.

Control pulse energy-dependent series of the space and spectral distribution of the output field were recorded separately from both cores to study the effect of the fiber length, the delay between the signal and control pulses, and the choice of the fiber core. More details about the experimental setup are presented in [38, 48]. The camera images were processed by calculating the dual-core extinction ratio (*ER*) integrating separately the intensity distribution in the area of both cores. Fig.1 (right) shows the camera images at the output facet of the DCF with an optimal length of 14 mm under excitation of the fast (top series) and slow (bottom series) cores, respectively. The results revealed that the fast core excitation supports a more efficient switching performance than the slow one thanks to the DC asymmetry balancing principle [48]. In the first case, a switching contrast of 41.5 dB was calculated between 0.2 and 0.6 nJ control energy levels at which the highest and lowest*ER* were identified, respectively. In the case of slowcore excitation (bottom series), no switching performance has been recorded. Therefore, in this paper, we report solely on the results of the fast core excitation, mainly*ER* dependence on control pulse energy, delay, and spectral transformations under different experimental conditions.

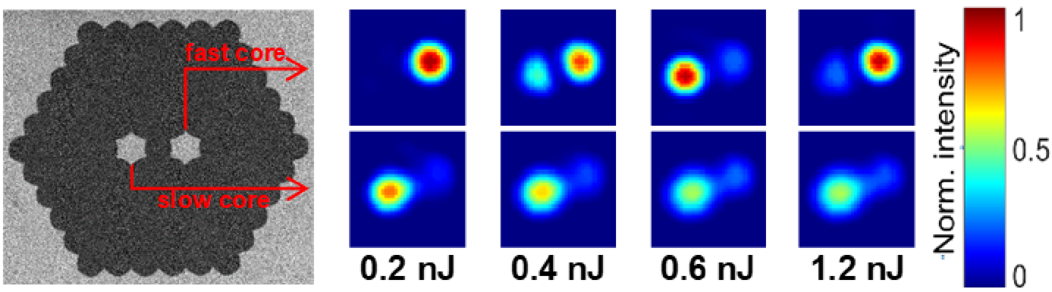

Fig. 4.1: *Scanning electron microscope image of the cross-section of the all-solid DCF structure (left). Infrared camera images of the 1560 nm, 75 fs signal field at the DCF output under increasing energy of 1030 nm, 270 fs control pulses and exciting the right (top series) and left (bottom series) cores of a 14 mm DCF with the combined beam.*

4.2 Theoretical Insight

4.2.1 Theoretical model and rescale of physical parammeter

To follow the main features of the system dynamics we introduced a model based on coupled nonlinear Schrödinger equations (NLSE). The dynamics of the control pulse amplitude A_0, which is propagating only in the bar core, is described by

$$\frac{\partial A_0}{\partial z} = -\beta_{10}\frac{\partial A_0}{\partial t} - \frac{i\beta_{20}}{2}\frac{\partial^2 A_0}{\partial t^2} + i\gamma|A_0|^2 A_0, \tag{4.1}$$

where z and t are the propagation distance and time in physical units, and coefficients β_{10}, and β_{20}, γ, represent, respectively, group velocity the group-velocity dispersion and Kerr nonlinearity. Similarly, equations for signal pulse amplitudes in the mismatched bare and cross-cores of the fiber read

$$\begin{aligned}\frac{\partial A_1}{\partial z} &= -\beta_{11}\frac{\partial A_1}{\partial t} - \frac{i\beta_{21}}{2}\frac{\partial^2 A_1}{\partial t^2} + i\kappa_0 A_2 - \kappa_1\frac{\partial A_2}{\partial t} - 2i\delta A_1 + i\gamma|A_0|^2 A_1,\\ \frac{\partial A_2}{\partial z} &= -\beta_{12}\frac{\partial A_2}{\partial t} - \frac{i\beta_{22}}{2}\frac{\partial^2 A_2}{\partial t^2} + i\kappa_0 A_1 - \kappa_1\frac{\partial A_1}{\partial t},\end{aligned} \tag{4.2}$$

where $\beta_{11} = \beta_{12} = \beta_1$ is the signal pulse inverse group velocity, $\beta_{21} = \beta_{22} = \beta_2$ is the signal pulse GVD, (equal in both cores), γ is nonlinearity coefficient (control pulse is acting on the signal by XPM only), δ is the difference of the refractive index between cores, defined as $\delta = (\beta_{01} - \beta_{02})/2$, κ_0 and κ_1 are zeroth and first-order coupling coefficient, respectively.

By means of the rescaling and introducing retarded time $\tau = t\sqrt{\kappa_0/|\beta_2|}$, unit of length $z = z\kappa_0$, $\psi = \sqrt{\gamma/\kappa_0}A_0$ and $\phi_{1,2} = \sqrt{\gamma/\kappa_0}A_{1,2}$, Eqs. (4.1) and (4.2) are cast in the normalized form, with β_2, γ, and κ set equal to 1. We use the retarded time $T = \tau - z\beta_{10}$, to follow the control pulse (notice that control and signal pulses move with different group velocities). The rescaled equation for the control pulse in our simplified model becomes:

$$i\frac{\partial \psi}{\partial z} = \frac{\beta_{20}}{2\beta_2}\frac{\partial^2 \psi}{\partial T^2} - |\psi|^2\psi. \tag{4.3}$$

At the input of the bar core, the control pulse has form $\psi(0,\tau) = a_c \exp[-(\tau/w_1)^2]$, where $w_1 = T_c/(1.1774t_0)$ and a_c is the amplitude of control pulse in the reduced units. Here, T_c is fullwidth half maximum. The set of rescaled equations for a signal pulse becomes:

$$i\frac{\partial\varphi_1}{\partial z} = -i\alpha\frac{\partial\varphi_1}{\partial T} - \frac{1}{2}\frac{\partial^2\varphi_1}{\partial T^2} - (\gamma|\psi|^2 - 2\sigma)\varphi_1 - \varphi_2 - i\epsilon\frac{\partial\varphi_2}{\partial T},$$
$$i\frac{\partial\varphi_2}{\partial z} = -i\alpha\frac{\partial\varphi_2}{\partial T} - \frac{1}{2}\frac{\partial^2\varphi_2}{\partial T^2} - \varphi_1 - i\epsilon\frac{\partial\varphi_1}{\partial T} \tag{4.4}$$

where $\alpha = (\beta_1 - \beta_{10})/\sqrt{|\beta|/\kappa_0}$ is the group velocity mismatch between control and signal pulses, $\sigma = \delta/\kappa_0$ is the index mismatch between the cores and $\epsilon = \kappa_1/\sqrt{\kappa_0|\beta_2|}$ is the dispersive coupling coefficient.

The input of signal pulse, which enters only slow channel, has form $\phi_1(0,\tau) = a_s \exp\{-[(\tau - d)/w_2]^2\}$, where $w_2 = T_s/(1.1774t_0), T_s$ is full width half maximum and a_s is the amplitude of the signal pulse. The parameter d in the signal pulse formula denotes the delay between the control and signal pulse. The units of propagation length and time are related to the experimental parameters by:

$$t_0 \equiv \sqrt{|\beta_2|/\kappa_0} = 2.49854 \times 10^{-14}[\mathrm{s}], \tag{4.5}$$

$$z_0 \equiv 1/\kappa_0 = 8.11402 \times 10^{-3}[\mathrm{m}]. \tag{4.6}$$

The energy of the control pulse as a function of intensity a_c can be expressed as:

$$E = \int_{-\infty}^{+\infty} |A_1(0,\tau)|^2 t_0 d\tau = \frac{\kappa_0 \tau_0 a_c^2 w_1}{\gamma} \approx 15.189 a_c^2 \text{ pJ}. \tag{4.7}$$

The width of the control pulse is $T_c = 270$ fs and signal pulses $T_s = 75$ fs. Effective coupling is given by $\kappa_{eff} = \sqrt{\kappa_0^2 + \delta^2} = 900.97812$ m^{-1}, where $\kappa_0 = 123.24347$ m^{-1}. We calculate the widths of the pulses for the rescaled equations, obtaining $w_1 = 9.1780$, $w_2 = 2.5494$. The values mentioned here are constants; therefore, they will no longer be specified in the parameter list in the following figure captions.

4.2.2 Switching mechanism

We simulated pulse propagation in the parameter range corresponding to the experiment performed in the 14 mm long all-solid dual-core in-house drawn fiber. The values of parameters, mentioned above, were produced by Lumerical mode solver at carrier wavelength $\lambda = 1030$ nm for the control pulse, and $\lambda = 1560$ nm for the signal. In the simulations, we also used the

Table 4.1: *Optical parameters of the first core, corresponding to the fiber used in the experiment, was produced with the help of the mode-solver at the carrier wavelength of* 1030 *nm.*

Physical quantity	Value	Units
n_{eff}	1.85333	
β_{00}	11.3051×10^{6}	1/m
β_{10}	6.58267×10^{-9}	s/m
β_{20}	10.2827×10^{-26}	s^2/m
γ	1.86066	1/(W.m)

Table 4.2: *Optical parameters of the dual-core fiber, corresponding to the fiber used in the experiment, was produced with the help of the mode-solver at the carrier wavelength of* 1560 *nm.*

Physical quantity	1st core	2nd core	Units
n_{eff}	1.79384	1.79341	
β_0	7.22477×10^{6}	7.22304×10^{6}	1/m
β_1	6.57165×10^{-9}	6.57198×10^{-9}	s/m
β_2	-7.69372×10^{-26}		s^2/m
κ_{eff}	900.97812		1/m
κ_0	123.24347		1/m
κ_1	-9.20669×10^{-13}		s/m

value of $\gamma = 1.86\,(\mathrm{W}\cdot\mathrm{m})^{-1}$ for the nonlinearity coefficient. Notice that the control pulse experiences both effects of dispersion and self-phase modulation, but the signal, which is relatively weak, interacts with control via cross-phase modulations, and only in the first channel (core). First, we looked at the interaction of control and signal pulse that occurred at the overlap area. Figure 4.2a shows a schematic of the relative width of signal and control pulses and relative the walk-off over the length of the DCF (dashed lines) where the delay is arbitrarily chosen to be 510 fs. The walk-off distance is about one-half of the FWHM of the control pulse. Thus the signal pulse only interacts with either the trailing edge or the leading edge of the control pulse. Furthermore, due to the self-phase modulation, the control pulse is widened in the time domain, coinciding with a weakening of the peak power. This behavior is presented in the 4.2b, showing the evolution of the control pulse after various propagation distances. Therefore, to maximize energy transfer using compensation of mismatch and nonliterary, the control pulse intensity at the input of the excited core must be higher than the level of mismatch.

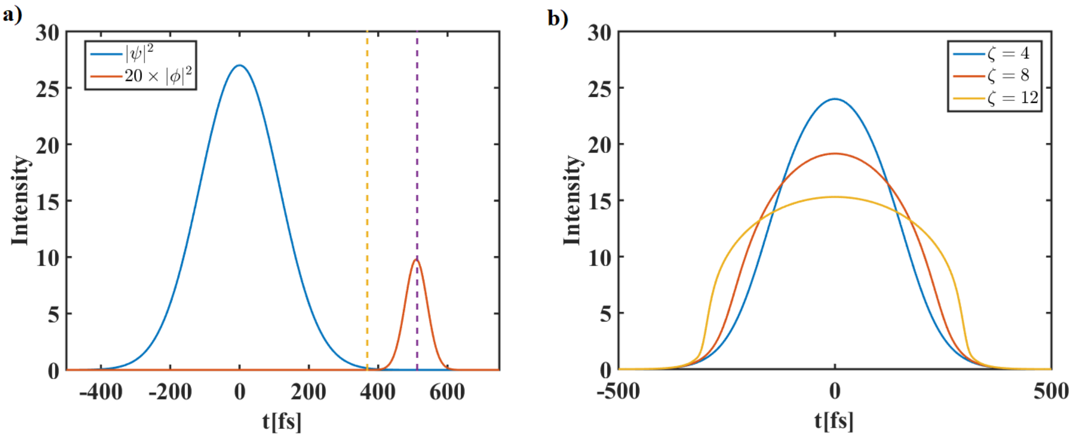

Fig. 4.2: *a) Schematic of the relative width of signal and control pulses; the distance between dashed lines indicates relative the walk-off over the length of the DCF. b)Control pulse after different distances*

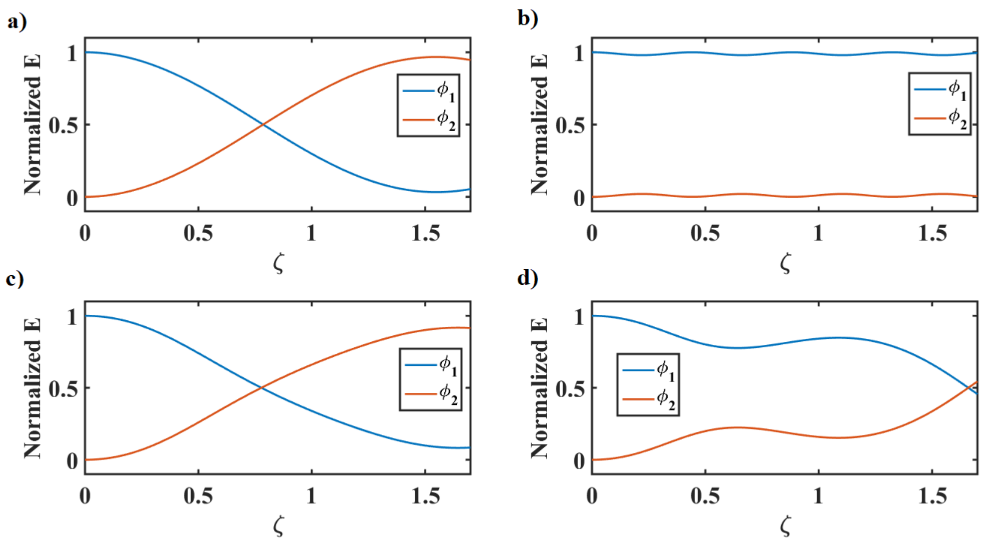

Fig. 4.3: *Switching performance in the DCF: a) Perfect cross-transfer in the case of symmetric fiber. b) oscillations with negligible transfer for the used asymmetric DCF without control pulse. c) The best switching performance that we obtained using a control pulse of 340 pJ. d) situation when compensating control pulse has too high intensity.*

Then we calculated the energy transfer of the energy of the signal pulse between both cores. Results of the simulations are presented in Fig. 4.3. In panel (a) we show, for the control, switching in the case of the fiber with perfectly symmetric cores. Notice that it approximately corresponds to half the period of the inter-core oscillation. When asymmetry is present, the period of oscillations is increased; however, the transfer is dramatically reduced (see model below). Its effect on the experimental conditions is represented in panel (b) The presence of an extra control pulse of appropriate intensity compensates for the mismatch, as shown in panel (c). Nonetheless, if the control intensity is not optimized, the switching performance may still

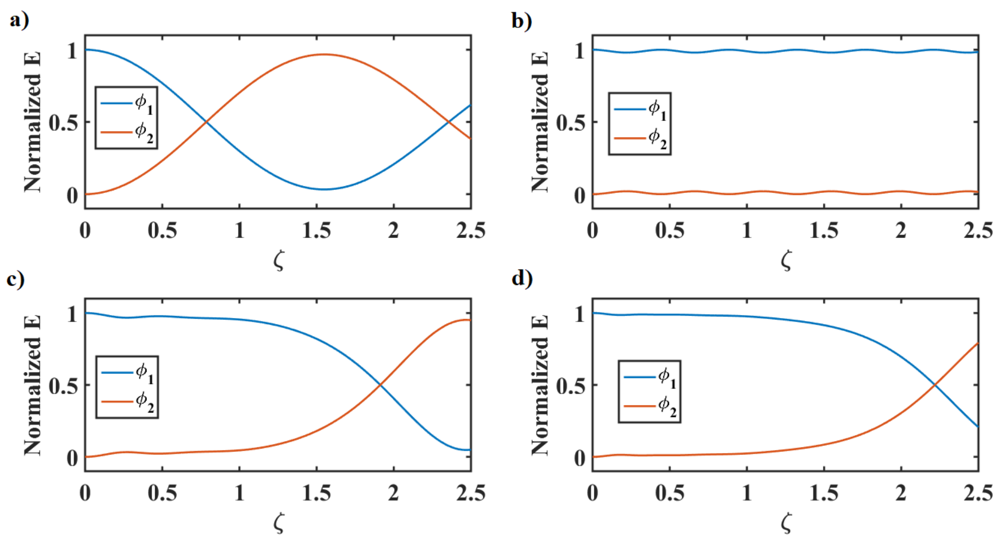

Fig. 4.4: *Switching performance in the DCF with fiber length equals to 2.5: a) Inter-channel oscillation in the symmetrical fiber in the absence of control pulse. b) oscillations with negligible transfer for the used asymmetric DCF without control pulse. c) show the best performance that we obtained using a control pulse of 550 pJ d) situation when compensating control pulse has too high intensity.*

be rather low, as shown in panel (d). Hence, optimization has to be performed for suitable delays between signal and control and for suitable lengths of the fiber. In figure 4.4 we show, not related to our particular experiment, that optimization is also possible for longer fibers. In the absence of mismatch, they would accommodate several oscillations, and, when using an appropriate energy of the control pulse, quite effective switching can be achieved.

4.2.3 The effect of delay and control energy

Naturally, the total energy, $E_1(z) + E_2(z)$, stays constant in the course of the oscillations between the cores. To further characterize the quality of the switching performance, we investigated how the output extinction ratio, defined as $ER = 10 \cdot \log(E_1/E_2)$, depends on the delay between signal and control pulses and how it depends on the power of the control pulse. In Fig. 4.6a and 4.6b we report the experimental result and simulation of delay dependences of *ER*, showing that its minimal value at larger delays with increasing control pulse energy. It is in correspondence with the asymmetry compensation principle because at higher control energies the signal pulse experiences the same refractive index change already at larger delays on the falling edge of the control pulse. The simulations predict the possibility of reaching *ER* minima at the level of -10 dB at energies in the range of 280 – 300 pJ and around delays of 75 fs. Taking into consideration the 150 fs walk-off determined by the 14 mm fiber length, such conditions are related to signal pulse moving in the peak area of the control one. However, the experimental results did not reveal such low *ER* most probably due to the nonlinear distortions of the control pulse - not included in our model - which are significant just around the pulse peak. On the other hand, the delay dependence at 340 pJ fits the obtained experimental curve (inset) both in terms of *ER* minima level and range of delays where *ER* has a negative sign. It is worth mentioning that the experimental curve was obtained at 600 pJ control energy, which is another signature of further loss processes affecting the control pulse and preventing reaching the compensation effect at lower pulse energies.

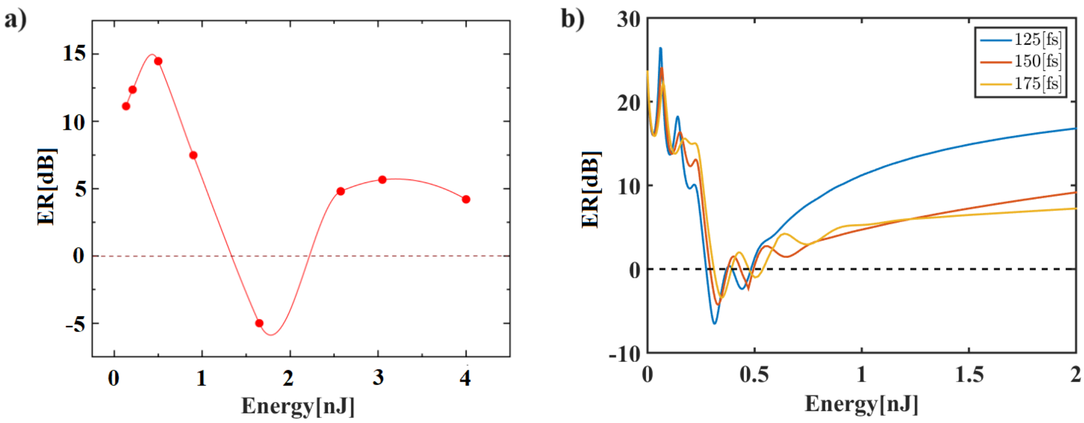

Fig. 4.5: *ER dependence as a function of 1030 nm, 270 fs control pulse energy under excitation with various delay times in the case of DCF with 14 mm length. Panel a) shows the experimental results corresponding to the simulation ones in panel b).*

In the following experiment we keep the delay time constant and change the control energy, then calculate the output extinction ratio. The result is shown in figure 4.5b. Our simulation result is presented in figure 4.5b, where we plot the control energy dependence of *ER* for different delays between signal and control pulses in the range of 125 - 175 fs. Those curves confirm again that the experimentally accessible *ER* minima is supported at 150 fs delay, which is an essential outcome due to the lack of absolute delay scale identification during the experimental study. Furthermore, such a large delay applied to get the best experimental results suggests the improvement potential of our approach which contributes to suppressing the walk-off. Taking into consideration the complex study of control pulse energy and delay dependencies, we conclude that there is a quite wide range of both delay times and energies where the effective high contrast switching occurs and that this phenomenon is robust. In addition to the study above, we examine the effect of asymmetry on switching performance by assuming that the asymmetry is smaller than that in the experiment. In this case, we use the same set of parameters except for

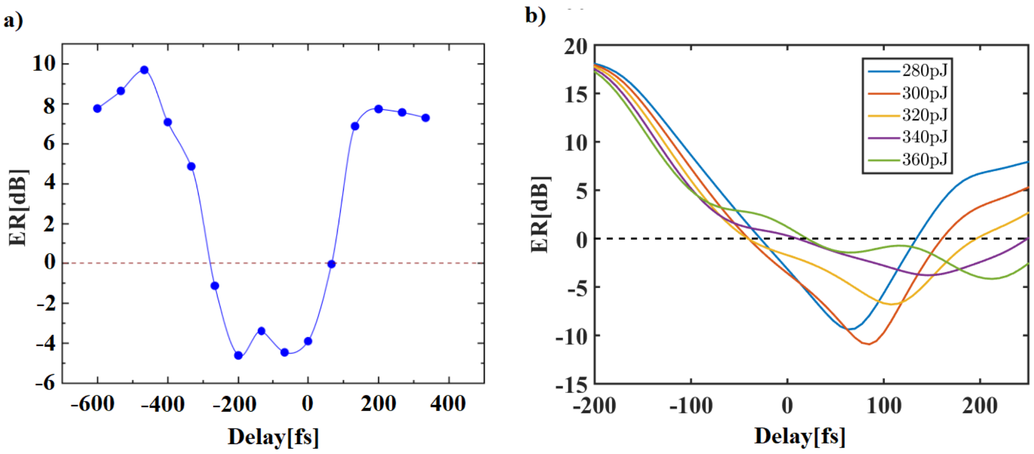

Fig. 4.6: *ER dependence as a function of delay of the signal pulse from the control one in the case of DCF with 14 mm length and under excitation with various energies of 1030 nm, 270 fs control pulses. Panel a) shows the experimental results corresponding to the simulation one in panel b) when the control pulse energy is 490 pJ.*

asymmetry in which $\sigma = 2$ and vary the control energy in the same fashion in the previous simulation. The result is shown in Fig. 4.7. When the control pulse energy is low, especially 61 pJ, the extinction ratio curves have one minimum at $ER \approx -6$[dB]. When the energy of control increases to 76 pJ, the minimum decreases and reaches the lowest values at $ER \approx -17$[dB]; this is where switching performance is optimized. However, if we increase the control energy even further, two minima of the extinction ratio emerge, with one having a slightly lower ER than the other. The switching performance now becomes less effective as the minima of the ER curve increases. Due to low asymmetry, the energy of the control pulse required to compensate for asymmetry is low. The control pulse shape then does not expand as much as shown in Fig4.2b through propagation. Thus, in the case of a single minimum, the cross-phase modulation and asymmetry are well balanced at a single point in which the signal pulse passes through the peak of the control pulse. In the case of two minima, the cross-phase modulation and asymmetry are well balanced when the signal pulse passes through either the trailing edge or leading edges of the control pulse where asymmetry and control pulse are. Overall, compared with the simulation result from the real structure, switching is slightly improved with a smaller ER in a more symmetrical DCF. However, the range of delay that switching takes place is smaller in this case, around 50 fs if it is optimized.

Another parameter that can affect the switching performance is dispersive coupling. In Fig.4.8, we show ER-dependent on delay, with various values of ϵ, especially $\epsilon = 0.05, 0.1, 0.15, 0.2$ and 0.25. The energy of control in this case is 320 pJ. If $\epsilon = 0.05$, there are two local minima in

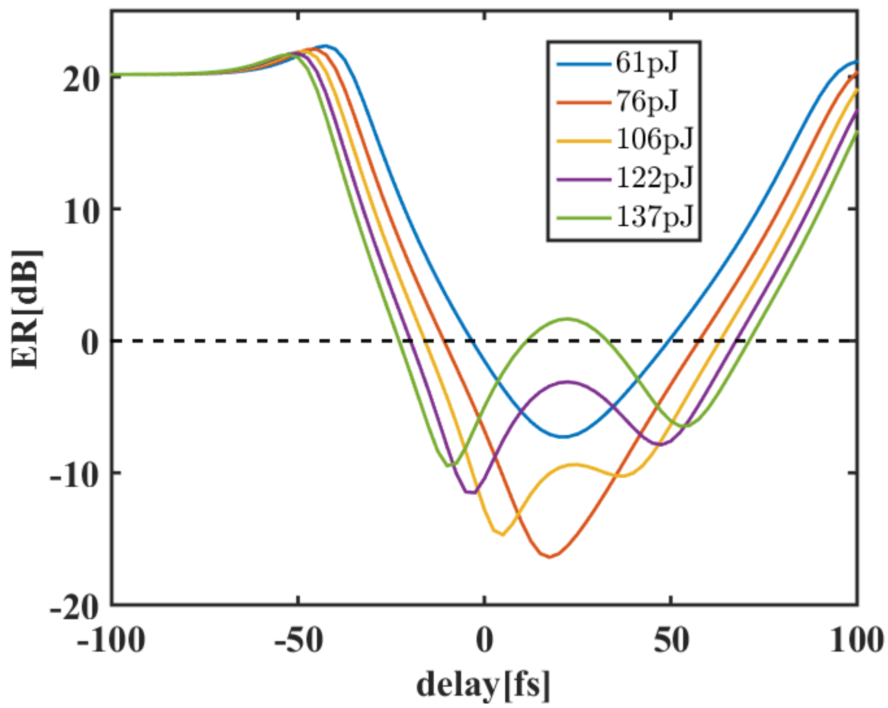

Fig. 4.7: *ER dependence as a function of delay of the signal pulse from the control one in the case of DCF with 14 mm length and under excitation with various energies of 1030 nm, 270 fs control pulses asymmetry coefficient* $\sigma = 2$.

the ER curve with one responding to a positive delay (between 100 to 150 fs) having a smaller ER and one responding to a positive delay (between -50 to 0 fs) has a larger ER. As ϵ increase, the higher minimum become less distinct and when $\epsilon = 0.2$, it completely disappears. The lower minimum meanwhile only slightly decreases and it is comparable with the $\epsilon = 0.3$, which is rescaled from Eq. (4.2). Despite that, the dramatic change from two minimum features to one minimum makes the dispersive coupling could not be ignored in our model.

4.2.4 Effect on signal spectrum

Finally, we performed several simulations varying delay for $\sigma = 7.03252$, $\alpha = 3.5$, and energy $E = 320$ pJ for the fiber length 14 mm and analyzed the spectral shape of the output signal pulses. The results of the simulation are shown in Fig. 4.9, where we also present in panel a) experimental results. From these simulations, which are in qualitative agreement with the experiment, we obtained that for positive delay spectrum of the signal pulse at the output is red-shifted and slightly broadened. In the case of the negative delay, when the center of the control is proceeding that of the signal we observe blue shift and spectral narrowing.

We conducted a detailed analysis of the dual-wavelength switching of 1560 nm, 75 fs pulses

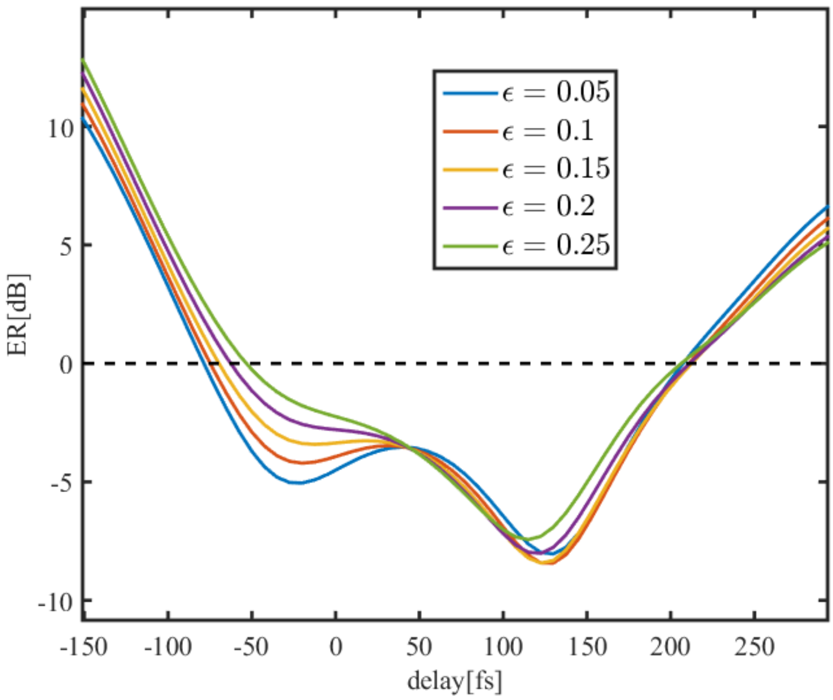

Fig. 4.8: *ER dependence as a function of delay of the signal pulse from the control one in the case of DCF with 14 mm length and under excitation with various values dispersive coupling. The control energy is 320 pJ*

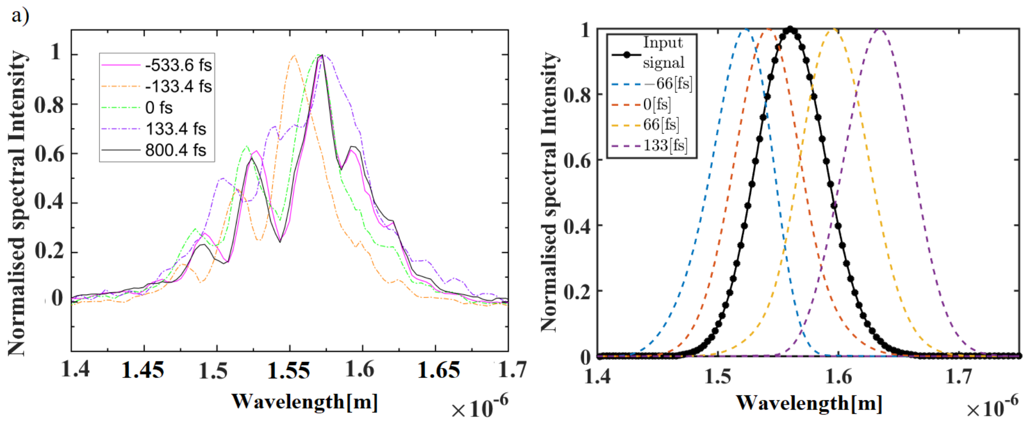

Fig. 4.9: *Normalized spectral shapes of the signal pulse for different delays at the output of the excited core (dashed lines) or non-excited core (solid lines): a) Experimental results where fiber length and energy of control are 14 mm and 600 pJ, respectively. b) Simulation results where fiber length and energy of control pulse are 17 mm and 320 pJ, respectively. Other parameters are* $\alpha = -3.5$, $\epsilon = 0.3$ *and* $\sigma = 7.03252$. *The corresponding experimental values of group velocity difference, dispersive coupling, and mismatch are* $\beta_{1} - \beta_{10} = 11.102 \cdot 10^{-11}$ *s/m,* $\delta = 865$ *1/m,* $\kappa_0 = 123.24347$ *1/mm.*

(labeled *signal*) using 1030 nm, 270 fs pulses (labeled *control*) through a dual-core fiber, including the effects of fiber length, control pulse energy, and time delay between the control and signal pulses on the switching performance. We found that the highest switching contrast of 41.5 dB was achieved at a fiber length of 14 mm, with a broadband character in the spectral range of 1450-1650 nm.

The theoretical simulations revealed the role of the asymmetry of the effective refractive index and walk-off between the control and signal pulses confirming our preliminary switching concept: the nonlinear balancing of such asymmetry. Moreover, the numerical outcomes revealed the simultaneous effect of the pulse energy and delay on the dual-core extinction ratio. One of the key advantages of our approach is the moderate nonlinear interaction between the control and signal pulses, which only slightly transforms the signal field. The numerical results also support this concept, predicting moderate transformations of the signal spectra and revealing a non-trivial dependence on the pulse delay.

One of the key advantages of our approach is the moderate nonlinear interaction between the control and signal pulses, which only slightly transforms the signal field. The numerical results also support this concept, predicting moderate transformations of the signal spectra and revealing a non-trivial dependence on the pulse delay. On the other hand, the control pulses experience more complex nonlinear transformations than expected in our model; therefore, the numerical results predict better switching performance than the obtained experimental results. However, in the region of moderate nonlinear interaction - i.e. the falling edge of the control pulse – we found a convincing correspondence between the experimental and numerical results. In summary, our study provides a comprehensive analysis of dual-wavelength switching using a specially developed dual-core fiber. Our experimental and theoretical findings shed light on the physical mechanisms behind this process and highlight the advantages of our approach, which offers moderate nonlinear interactions and only slight transformations of the signal field. In the frame of the current experiment, the alignment and the synchronization of the two beams were improved thanks to fewer reflections imposed by mirrors along the optical paths and better alignment between the signal and control beams. Thanks to these precautions, the energies at which the switching performance takes place are about 10 times lower than the ones identified in the optimal case in [48]. The sub-nanojoule, high switching contrast results presented in this paper show an interesting application potential in the field of all-optical signal processing. Finally, the numerical calculations reveal the possibility for further improvement both in terms of switching contrast and energy eliminating the walkoff between the control and signal pulses.

Chapter 5

PT-symmetry in dual-core photonic crystal fibers

$\mathcal{PT}$-symmetry is a theoretical concept elaborated by Bender et al. in 1998 [51]. It is based on the possibility of treating a Hermitian quantum system as a combination of two non-Hermitian non-isolated subsystems [52]. Both of them are characterized by a nonzero flux of probability, positive and negative respectively, across their boundaries; however, the non-isolated combined system has no net flux of probability, i.e. it could exhibit real spectra or equivalently real eigenvalues [53]. This concept finds application in several fields of science, such as atomic systems [54], mechanics [55] and electronics [56].

In this chapter, we investigate the properties of a soft glass dual-core fiber for application in multicore waveguiding with balanced gain and loss. Its base material is a phosphate glass in a P_2O_5-Al_2O_3-Yb_2O_3-BaO-ZnO-MgO-Na_2O oxide system. The separated gain and loss channels are realized with two cores with ytterbium and copper doping of the base phosphate glass. The ytterbium-doped core supports a laser (gain) activity under excitation with a pump at 1000 nm wavelength, while the copper-doped is responsible for strong attenuation at the same wavelength. We establish conditions for an exact balance between gain and loss and investigate pulse propagation by solving a system of coupled generalized nonlinear Schrödinger equations. We predict two states of light under excitation with hyperbolic secant pulses centered at 1000 nm; 1) linear oscillation of the pulse energy between gain and loss channel ($\mathcal{PT}$-symmetry state), with strong power attenuation; 2) retention of the pulse in the excited gain channel (broken $\mathcal{PT}$-symmetry), with very modest attenuation. The optimal pulse energy levels were identified to be 100 pJ (first state) and 430 pJ (second state).

5.1 General concept of PT symmetry

5.1.1 The Parity-Time Reversal Operator

The time evolution of a physical system is determined by equations derived from the Hamiltonian. In conventional quantum mechanics, physical systems evolve according to a Hermitian Hamiltonian. We refer to such systems as closed or isolated systems. We use the term Hermitian Hamiltonian to mean that if the Hamiltonian H is in matrix form, then H remains invariant under the combined operations of matrix transposition and complex conjugation. The eigenvalues of a Hermitian Hamiltonian are always real, thus, it conserves probability (the norm of a state).

In a non-isolated system, there is an energy exchange with the external environment. Here, we are only interested in the ones that have no net flux of probability. Such a system can be constructed by coupling two exact copies of a non-isolated system but with the opposite net flux of probability. Thus, the new total physical system consists of two subsystems: (i) the original non-isolated physical system, which has a nonzero net probability flux across the boundary, and (ii) the time-reversed system, which has the opposite flux of probability. Together, these two subsystems demonstrate an equilibrium in probability exchange since any gain (or loss) in the original system is exactly countered by a loss (or gain) in the time-reversed system. Hence, the composite system experiences no net gain or loss. The composite loss-gain system exhibits a symmetry called PT symmetry.

We can easily prove that PT symmetry Halmitonians also have real eigenvalue. Let symbol $\mathcal{P}$ represent the parity operator (space-reflection) operator which flips the sign of spatial coordinates

$$\mathcal{P} : \mathbf{r} \rightarrow -\mathbf{r},$$

while the time operator $\mathcal{T}$ represents the operation of time reversal, and it has the effect of turning a system with gain into a system with loss (and vice versa). Mathematically, it changes the sign of time:

$$\mathcal{T} : \mathbf{t} \rightarrow -\mathbf{t}.$$

In terms of the position and momentum operators $\hat{x}$ and $\mathcal{P}$,

$$\begin{aligned} \mathcal{P} &: x \to -x, p \to -p, \\ \mathcal{T} &: x \to x, p \to -p. \end{aligned} \tag{5.1}$$

P and T are characterized by the following

$$\begin{aligned} \mathcal{P}^2 = \mathcal{T}^2 &= \mathbf{I}, \\ [\mathcal{P}, \mathcal{T}] &= 0. \end{aligned} \tag{5.2}$$

Let $|\Psi\rangle$ and λ be an eigenstate and eigenvalue of $\mathcal{PTT}$. Then, using Eqs. (5.1)-(5.2), we can write

$$\mathcal{PTPT}\,|\psi\rangle = \mathcal{PT}\lambda\,|\psi\rangle \implies |\psi\rangle = \lambda^*\lambda\,|\psi\rangle \implies |\lambda| = 1. \tag{5.3}$$

An operator $\hat{A}$ is $\mathcal{P} - \mathcal{T}$ symmetric if $[\hat{A}, \mathcal{PT}] = 0$. Thus the eigenvalues of the $\mathcal{PT}$ operator are of the form $\lambda = e^{i\theta}$ for some $\theta \in [0, 2\pi)$. H and $\mathcal{PT}$ commute, so if H has eigenstate $|\Psi\rangle$ and eigenvalue E, we have

$$H\,|\psi\rangle = E\,|\psi\rangle \tag{5.4}$$

$$H(\mathcal{PT}\,|\psi\rangle) = \mathcal{PT}H\,|\psi\rangle = \mathcal{PT}E\,|\psi\rangle = E^*(\mathcal{PT}\,|\psi\rangle).$$

Thus, E^* is also an eigenvalue of H, corresponding to the eigenstate $\mathcal{PT}\,|\psi\rangle$. This property of PT symmetry guarantees that all eigenvalues appear in complex-conjugate pairs. PT symmetry is considered to be spontaneously broken when H and $\mathcal{PT}$ are no longer simultaneously diagonalizable. An operator H has unbroken PT symmetry if H and $\mathcal{PT}$ can be diagonalized by the same eigenstates. In other words, if $|\psi\rangle$ is an eigenstate of H with E as its corresponding eigenvalue, then there exists a λ such that $\mathcal{PT}\,|\psi\rangle = \lambda\,|\psi\rangle$. We can prove that unbroken PT symmetry is sufficient for real energy spectra. Let non-Hermitian operator H have unbroken PT symmetry. Then, H and $\mathcal{PT}$ can be simultaneously diagonalized by the eigenstate $|\psi\rangle$ of H

$$H\,|\psi\rangle = E\,|\psi\rangle \tag{5.5}$$

$$\mathcal{PT}\,|\psi\rangle = \lambda\,|\psi\rangle = e^{i\theta}\,|\psi\rangle\,.$$

Operating PT on the first equation:

$$\mathcal{PT}H\,|\psi\rangle = \mathcal{PT}E\,|T\rangle = E^*\mathcal{PT}\,|\psi\rangle = E^*e^{i\theta}\,|\psi\rangle\,. \tag{5.6}$$

Since H and $\mathcal{PT}$ commute, $\mathcal{PT}H\,|\psi\rangle = H\mathcal{PT}\,|\psi\rangle = E\mathcal{PT}\,|\psi\rangle = Ee^{i\theta}\,|\psi\rangle$. Hence, $E = E^*$ and the spectrum of H is real

5.1.2 Exceptional point

Consider a minimal example of non-Hermitian, PT-symmetric systems, given by

$$H = \begin{pmatrix} i\alpha & \kappa \\ \kappa & -i\alpha \end{pmatrix} = \kappa\sigma_1 + i\alpha\sigma_2. \tag{5.7}$$

where $g, \kappa \in \mathbb{R}$, $g, \kappa > 0$, and we have used σ_J, $J = 1, 2, 3$ to denote the Pauli matrices

$$\sigma_1 = \begin{pmatrix} 0 & 1 \\ 1 & 0 \end{pmatrix}, \quad \sigma_2 = \begin{pmatrix} 0 & -i \\ i & 0 \end{pmatrix}, \quad \sigma_3 = \begin{pmatrix} 1 & 0 \\ 0 & -1 \end{pmatrix}. \tag{5.8}$$

The eigenvalues and eigenvectors of H are given by

$$E_\pm = \pm\sqrt{\kappa^2 - \alpha^2}, |\psi\rangle_\pm = \begin{pmatrix} ig \pm \sqrt{\kappa^2 - \alpha^2} \\ \kappa \end{pmatrix}, \tag{5.9}$$

for $\kappa \geq \alpha$ the spectrum of H is purely real. For $\kappa < g$ the spectrum of H is purely real. PT symmetry is spontaneously broken at $\kappa = \alpha$. As $\alpha \to \kappa$ from both sides, both pairs of eigenvalues (real and imaginary) coalesce to a single eigenvalue at $E = 0$, and the eigenvectors of H become parallel. At this point, the single eigenstate of H does not span.

These symmetry-breaking points in parameter space of the form κ, g in this case have been dubbed exceptional points (EPs). They are the boundaries between regions of unbroken PT symmetry, where a Hamiltonian H has all real eigenvalues, and regions of broken PT symmetry where H has at least one pair of complex conjugate eigenvalues.

Exceptional point physics lends itself well to understanding gain/loss systems, which are especially prevalent in optics and photonics. Experimentalists discovered that PT symmetry could be readily established in coupled resonators with spatially balanced gain (amplification of optical power) and loss elements [57]. Their setups allowed for direct control over the energy exchange process via dene-tuning the coupling between the resonators [58].

In reference to our simple model presented in Equation (5.7), let's consider α as the parameter representing the optical gain or loss of one of two identical coupled optical components, such as waveguides or resonators. Parity P interchanges the gain and loss elements, while time reversal T converts gain to loss and vice-versa ($\alpha \leftrightarrow -\alpha$). The strength of interaction of these two elements is given by their coupling constant κ, describing the rate of signal transfer between the two elements - more coupling (higher values of κ) means less loss of signal (photons). When $\alpha \ll \kappa$, the coupling between the optical devices is much larger than their energy interchange with the external environment, resulting in a PT-symmetric system. When $\alpha \gg \kappa$, the rate of perturbation from the external environment dominates over the rate of probability transfer between the gain and loss components. As a result, a qualitatively different set of eigenstates emerges. In our example, these would be the states corresponding with the purely imaginary spectrum of the Hamiltonian given in (Eq. 5.9), i.e. exponentially growing and decaying modes. In the case where $\alpha = \kappa$, as before, corresponds to an EP where some eigenmodes of the system coalesce. As mentioned previously, the eigenstates of the system no longer form a complete basis at this point, making certain modes inaccessible.

5.2 PT-symmetry breaking in dual-core phosphate-glass optical fibers

In the field of optics and the paraxial propagation regime, the condition on complex potential translates into the one on the real and imaginary part of the refractive index, which should be symmetric and anti-symmetric, respectively [59], i.e.

$$n(x, y) = n^*(-x, y). \tag{5.10}$$

This means that the two refractive index profiles should be symmetric with respect to the central symmetry point and should have the same absolute values [60, 61] If this condition is not satisfied, the eigenvalues of the system cease to be real and the parity-time symmetry breaks down (it is referred as $\mathcal{PT}$-symmetry breaking), leading to complex spectra [62]. Theoretical works predicted such scenario in several optical systems [59, 63, 64], and also experimental verifications were achieved in periodic structures [65], photonics lattices [66], semiconductor-based dual microring laser resonators [67], plasmonic systems [68] and - recently - in high power large-area lasers [69].

One of the simplest realizations of $\mathcal{PT}$-symmetric optical system is a coupled waveguide, with one subjected to gain (active waveguide) and the other one to loss (dissipative waveguide) [70, 71] Moreover, it is possible to benefit the optical properties of gain/loss waveguides even in the nonlinear regime, i.e. studying $\mathcal{PT}$-symmetry in nonlinear directional couplers [72]. In these systems, the non-Hermitian eigenvectors formally maintain the same structural form of the corresponding linear one [60, 73, 74] It has been demonstrated that such systems are beneficial for all-optical switching in the nonlinear regime because of the possibility to lower the required switching power [75], achieve faster transition [76] and support stable switching states due to the possibility to support solitons [77, 78] The exact analytical formalism describing the switching dynamics in nonlinear $\mathcal{PT}$-symmetric couplers has been presented in [79]. In the last decades, dual-core [80, 81] and multicore optical fibers [82], which are one of the possible implementations of the nonlinear directional coupler, have attracted significant interest in the implementation of nonlinear $\mathcal{PT}$-symmetric systems due to their possible application in all-optical signal processing. In particular, dual-core fibers (DCFs) consist of two parallel channels throughout their whole length: one of the channels should provide gain for the guided light along propagation (gain channel), while the other one should cause losses to the propagating light (loss channel). To satisfy Eq.(5.10), the amount of provided gain and loss should be equal.

In the following sections, we will present a proof of concept, a possible implementation of a $\mathcal{PT}$-symmetric optical system in the form of DCF. The base material of the fiber is phosphate glass in a P_2O_5-Al_2O_3-Yb_2O_3-BaO-ZnO-MgO-Na_2O oxide system [83]. Gain and loss channels are implemented by ytterbium-based and copper-based doping, respectively. The fiber is suitable for fabrication with the stack-and-draw method [84]. We present the numerical studies of nonlinear phenomena in such optical $\mathcal{PT}$-symmetric systems, first evaluating effective parameters and then showing the predictions of pulse propagation in such systems using a simple model. These considerations can be also viewed as an interesting perspective of the all-optical switching using fiber-based devices.

5.3 Materials and design

The implementation of $\mathcal{PT}$-symmetric DCF requires first of all the gain channel. We propose to take advantage of the Yb-doped phosphate glass photonic crystal fiber laser fabricated by our group [85]. Fig.5.1a presents the SEM images of the cross-section of the fabricated fiber with different magnifications. The core material is phosphate glass doped with 6% mol of Yb_2O_3 ($15.69 \cdot 10^{20}$ Yb^{3+} cm^{-3}). In the frame of this study, a laser generation is demonstrated at the central wavelength of approximately 1 µm with more than 400 dB m^{-1} of pump absorption and the highest generation power of 150 W m^{-1}. The pump is a laser diode with a wavelength of 973.5 nm and 3 nm bandwidth. The threshold power for laser activity is 8.7 W, while the maximum pump power could reach the value of 35 W. The maximum output laser power in the CW regime is 9 W. The slope efficiency, which indicates the power conversion between the pump and the laser beam – i.e. power pump/laser gain– could be as high as 36.2%. For our purpose, we consider this value as the target value of gain.

Next, we focus on the loss channel. In order to respect the balance between gain and loss, we need to use in the loss channel a glass that realizes a 36.2% power attenuation – or equivalently 73.8% transmission – at 1 µm and the same length of 6 cm. In order to estimate the loss coefficient for the loss channel α, we use the standard Beer-Lambert law, $P(z) = P_0 e^{-i\alpha z}$, where P_0 is the input power and z is the propagation distance. Considering that $P(z = 6 \text{ cm})/P_0$ should be $\approx$ 73.8%, the absorption coefficient resulted in the value of $\alpha = 7.49$ m^{-1}. Here we propose CuO-doped glass for the loss channel. As the phosphate glass has a much higher attenuation than silica (0.46 vs 0.001 m^{-1}) [83], the estimated required percentage of copper doping should be rather low, at the level of 0.015% CuO.

Fig.5.1 a report the refractive index profile of the phosphate glass (blue curve) and Yb-doped one (red curve) in the spectral range 430-1490 nm, while Fig.5.1b shows the difference between the two refractive indices in the same spectral range. The difference between the refractive indices is rather low, reaching a maximum value of approximately $1.4 \cdot 10$m^{-3} at 1490 nm. At 1 µm, the difference is $1.04 \cdot 10$ m^{-3}. The nonlinear refractive index n_2 of phosphate glass is 0.99 $\cdot$ 10^{-19} m^2/W at 1064 nm [43], approximately 4 times higher than the fused silica one (0.246 $\cdot$ 10^{-19} m^2/W [86]).

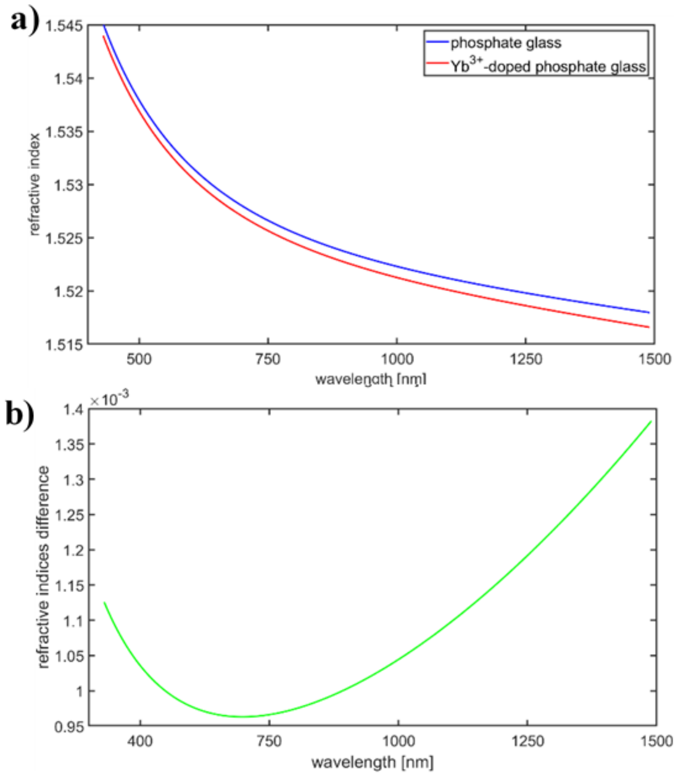

Fig. 5.1: *(a) Refractive index profiles of the undoped phosphate glass (blue curve) and Yb-doped one (red curve) in the spectral range 430-1490 nm. (b) Difference of the refractive indices between undoped and Yb-doped phosphate glasses in the same spectral range.*

5.4 Finding optical properties

For the particular design of the fiber (including geometry and the material), we can find the optical properties of the setup using numerical tools, for instant commercial LUMERICAL software. We started with the design shown in Fig.5.2a (schematic plot of the proposed fiber). This seemed to be a natural choice. Notice that due to the small refractive index difference between Yb-doped and undoped phosphate glass (see Fig.5.1b), we need to introduce a photonic lattice of air holes in the undoped phosphate glass in order to support the fundamental modes and improve the coupling efficiency between the cores [32]. Still, the concentration of copper doping in the loss channel is much lower than the ytterbium one in the gain channel (0.015% mol of CuO vs 6% mol of Yb_2O_3, respectively) and further studies are required to get more experience with this kind of glass. Therefore, we decided to postpone the study of this particular setup until we examine it thoroughly, both theoretically and in real experiments. Therefore we decided to postpone the study of this particular setup until we examine it thoroughly, both theoretically and in real experiments.

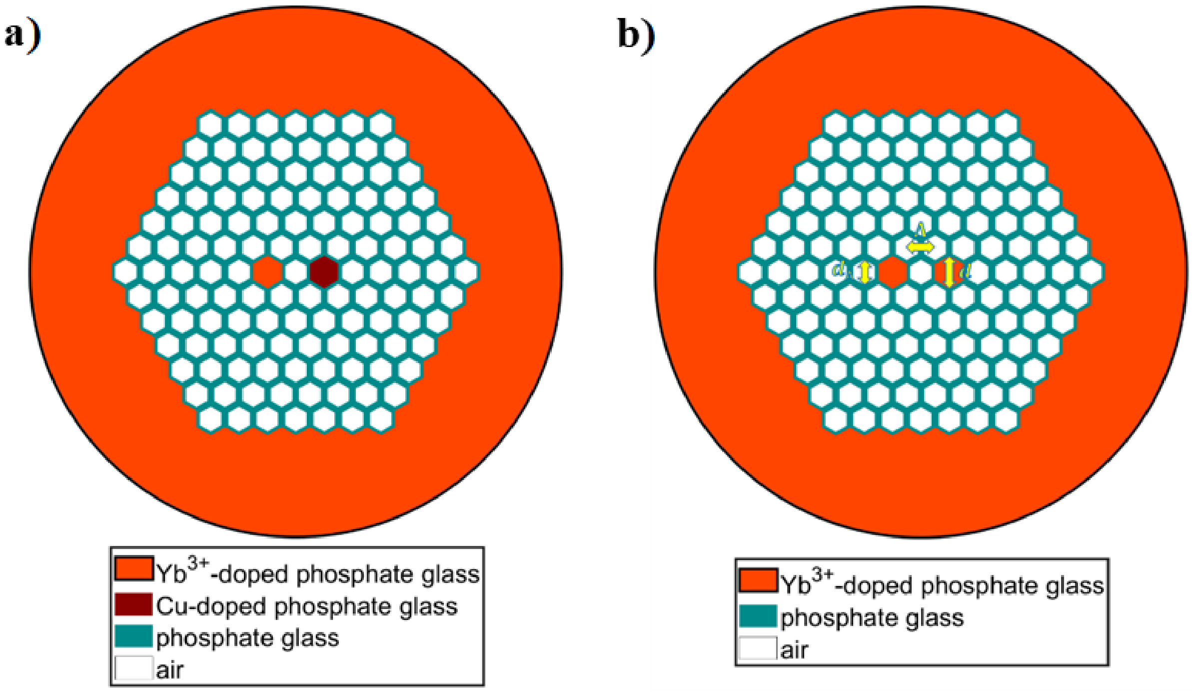

Fig. 5.2: *(a) Structure of the designed DCF laser: Yb-doped phosphate glass for the gain channel, Cu-doped one for the loss channel, and undoped phosphate glass for the cladding. An extra photonic lattice of air holes is introduced to support the coupling between the cores. (b) Fiber structure used for the simulation phase: the material of the loss channel has been substituted from Cu-doped phosphate glass to Yb-doped phosphate glass.*

Here we consider the structure in Fig.5.2b, where we replace the Cu-doped core with another Yb-doped one. The core diameter d and the lattice pitch Λ (marked with yellow arrows in Fig.5.2b) were the same as the optimized soft glass DCF presented in [35]. We used the same structure with $d = 1.85$ μm and $\Lambda = 1.6$ μm and added an extra photonic lattice of air holes with diameter $d_A = 1.4$ μm surrounding the two Yb-doped cores. The distance between centers of the cores is then $2\Lambda = 3.2$ μm, as in the fiber structure in [34].

Subsequently, the new structure was characterized in the context of optical field propagation in the linear regime. The commercial Mode Solution software from Lumerical was used to calculate the spectral dependences of the field mode profile, the corresponding effective index, and the waveguide losses for each fundamental mode. All the relevant quantities were acquired in the spectral window between 500 and 2400 nm, which sufficiently covers the wavelength of our interest (1000 nm).

Fig.5.3 shows the dispersion profiles of the fundamental supermodes, with horizontal polarization direction (along X-axis) and dual-core symmetric state. The dispersion is normal ($D < 0$) in the wavelength range of 800-1200 nm. We calculated another important linear pa-

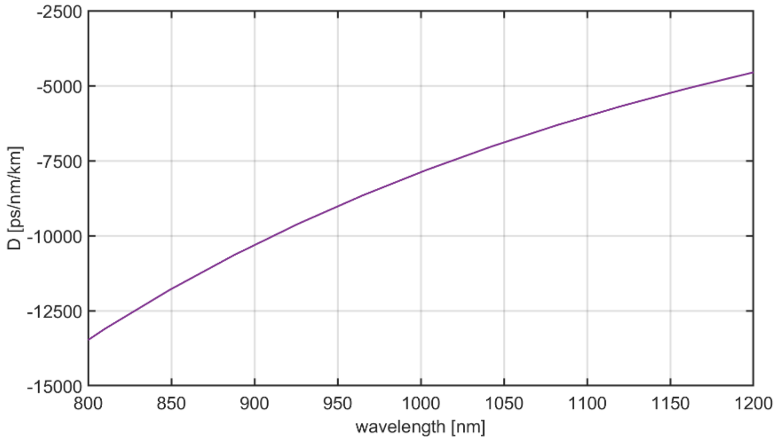

Fig. 5.3: *Simulated dispersion curves of the fundamental Symmetric-X supermode of the dual-core structure in Fig.5.3b. The fiber shows normal dispersion in the whole range of 800-1200 nm.*

rameter, the coupling length L_c. From the theory of nonlinear directional couplers, we know that, in the DCFs, the input radiation coupled in one of the two cores experiences (in the linear regime) periodic oscillations between cores with a period equal to L_c, defined as

$$L_c = \frac{\pi}{|\beta_S - \beta_A|} \tag{5.11}$$

where β_S and β_A are the propagation constants of symmetric and antisymmetric supermodes of the fiber, respectively [1, 34].

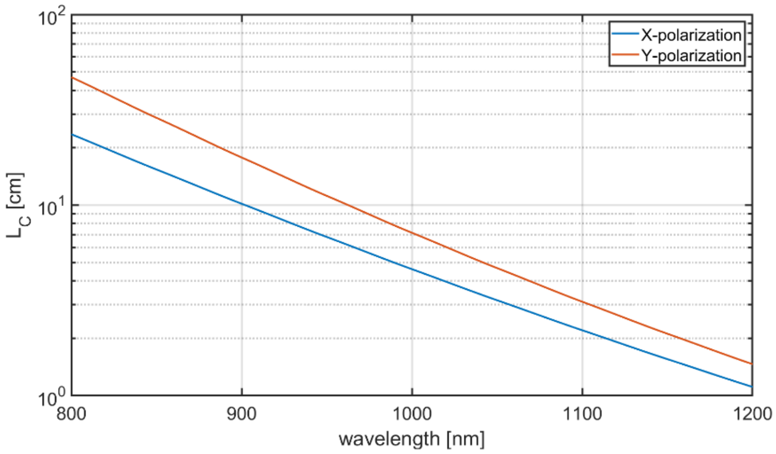

Fig. 5.4: *Simulated coupling length L_c spectral characteristics for fundamental X- and Y-polarized modes of the DCF in Fig.5.3b. The values are calculated using Eq.(5.11).*

Fig.5.4 reports the coupling length characteristics of the two fundamental supermodes, with horizontal and vertical polarization direction (X and Y-polarization, respectively) in the same wavelength range of Fig.5.3 (800-1200 nm). At 1000 nm, the values of L_c are 4.7 and 7.3 cm, respectively.

We calculated other linear and nonlinear parameters at the wavelength of interest 1000 nm, which were used for the numerical simulations. They include the effective refractive indices of the cores n_{eff}, the propagation constants β_0, β_1, β_2, the coupling coefficient κ and the nonlinear parameter γ. All the values except κ were calculated for a single core structure, that was obtained by filling one of the cores with undoped phosphate glass with diameter $d = 1.85$ µm and including one air hole with diameter $d_A = 1.4$ µm. We calculate the dispersion profile of the single-core fibers (left and right core separately) using Mode Solution software from Lumerical, including the spectral dependences of the field mode profile, the corresponding effective index, and the waveguide losses for each fundamental mode. The dispersion profiles of the single-mode fibers are reported in Fig.5.5. As the fiber structure is symmetric, the profiles of the two cores are identical and show a value of -780 ps/nm/km at 1000 nm. We also calculated the coupling coefficient between the two single-core modes based on the overlap integrals [1].

5.5 Numerical simulations of pulse propagation: method and results

In this section, we develop numerical methods to study pt-symmetric dynamics in our system. The goal of this part of the investigation is twofold. First, we identify the most important parameters (eliminating the others) and then we study the role of chromatic dispersion of the crucial characteristics: pulse dispersion, inter-channel coupling, and gain/loss coefficient.

5.5.1 Generalized Nonlinear Schrodinger Equation

In order to have a complete view of the system dynamics, the CGNLSE were solved numerically, including effects like coupling coefficient dispersion, self-steepening nonlinearity, and its spectral dependence, stimulated Raman contribution, cross-phase modulation, and waveguide losses. The resulting mathematical model is a system of two equations expressed in the following set of equations (r=1,2)

$$\frac{\partial A_{(r)}(z,t)}{\partial z} = (-1)^{r+1}\left(-i\delta_0 A_{(r)}(z,t) - \delta_1 \frac{\partial A_{(r)}(z,t)}{\partial t}\right) + \sum_l \frac{i^l}{l!}\alpha_l^{(r)} \frac{\partial^l A_{(r)}(z,t)}{\partial t^l} +$$
$$+\frac{1}{2}\sum_m \frac{i^{m+1}}{m!}\beta_m^{(r)} \frac{\partial^m A_{(r)}(z,t)}{\partial t^m} + \sum_n \frac{i^{n+1}}{n!}\kappa_n^{(r)} \frac{\partial^n A_{(3-r)}(z,t)}{\partial t^n} +$$
$$+ i\gamma^{(r)}\left[\left(1 + i\tau_{\text{shk}}{}^{(r)}\frac{\partial}{\partial t}\right)\int_{-\infty}^{\infty} R(\tau)\left|A_{(r)}(z,t-\tau)\right|^2 d\tau + \sigma^{(r)}|A_{(3-r)}(z,t)|^2\right] A_{(r)}(z,t) \tag{5.12}$$

where $r = 1, 2$ denotes the number of the core (1 – gain channel, 2 – loss channel), A_r is the corresponding electric field amplitude and quantities $\delta_0 = (\beta_0^{(r)} - \beta_0^{(3-r)})$ and $\delta_1 = (\beta_1^{(r)} - \beta_1^{(3-r)})$ represent the difference between the phase and group velocities respectively. Furthermore, $\alpha_k^{(r)}$, $\beta_k^{(r)}$ and $\kappa_k^{(r)}$ are the k-th order of Taylor expansion coefficients around the central frequency of gain/loss coefficient, propagation constant (dispersion) and coupling coefficient, respectively. Finally, $\gamma^{(r)}$ is the nonlinear parameter, $\tau_{\text{shk}}{}^{(r)}$ is the characteristic time of shock wave formation, R is the Raman response function, and $\sigma^{(r)}$ is the overlap integral between the single core modes defining for the cross-phase modulation effect in the r-th core. Both experimentally determined instantaneous Kerr and delayed Raman response of the guiding PBG-08 glass are included in the material nonlinear response function.

Moreover, we introduced the gain and loss coefficient in the CGNLSE by modeling the function of the loss coefficient $\alpha^{(r)}(\lambda)$. We modeled $\alpha^{(r)}(\lambda)$ to have a Gaussian-like profile in the wavelength domain as follows:

$$\alpha^{(r)}(\lambda) = (-1)^r \alpha_p \cdot \exp\left[\frac{(\lambda - \lambda_0)^2}{2\sigma_\lambda^2}\right], \tag{5.13}$$

where $\lambda_0 = 1000$ nm, which corresponds to the frequency $\omega_0 = (2\pi c)/\lambda_0 = 1.8837 \cdot 10^{15}$ rad $\cdot$ s^{-1}, $\sigma_\lambda = 100$ nm is the standard deviation of the Gaussian and $\alpha_p = 7.49$ m^{-1} is the peak amplitude.

The CGNLSE in Eq.(5.12) was solved numerically by the split-step Fourier method with 160,000 steps [34]. After every 400 calculation step, the field arrays were saved and then used to plot the output propagation maps; this means that the whole propagation distance is divided into 400 intervals. This approach represents a good compromise between the calculation time and the resolution of the propagation distance (fiber length). We considered a fiber length of 30 cm, which is 10 times larger than the estimated coupling length at 1000 nm (see Fig.5.4).

Using the split-step method, we considered the whole spectral behavior of loss and gain and applied them always at the frequency step. The input pulse shape was approximated by the sech^2 function, which is a good approximation for ultrafast oscillators. The power envelope of the pulse is expressed as:

$$P(t) = \frac{0.88 \cdot E}{T_{\text{FWHM}}} \text{sech}^2 \left(\frac{t}{T_{\text{FWHM}}} 1.763 \right) \tag{5.14}$$

At each of the 200 propagation steps, we integrated the pulse envelopes in each channel to observe the trend of the energy transfer along propagation. Fig.5.5 shows the propagation maps in case of 1000 nm wavelength, 1 ps pulse width hyperbolic secant pulse excitation with energy 100 pJ (top row) and 445 pJ (bottom row). We checked that the $\mathcal{PT}$-symmetry breaking takes place at 430 pJ: an energy increase through the fiber length is predicted in the gain channel, with some low-input features after 20 cm.

5.5.2 Simplified theoretical model

To simplify the model in Eq.(5.12), we set $\sigma = 0$ (no cross-phase modulation), $t_{\text{shk}} = 0$ (no shock wave formation), and $\int_{-\infty}^{\infty} R(\tau) d\tau = 1$ (impulsive Raman response). Moreover, we limit the dispersive terms to the second-order $\beta_2^{(r)}$, and only linear coupling. Due to the sensitivity of the system to the change of gain and loss, we keep the gain/loss coefficient with the full spectral dependence. We consider symmetric fiber structure, therefore $\kappa_0^{(1,2)} = \kappa_0^{(2,1)} = \kappa_0$, $\beta_2^{(1)} = \beta_2^{(2)} = \beta_2$,$\gamma^{(1)} = \gamma^{(2)} = \gamma$. Eq.(5.12) takes the form as follows

$$\frac{\partial A_{(r)}(z,t)}{\partial z} = -\frac{i\beta_2}{2}\frac{\partial^2 A_{(r)}(z,t)}{dt^2} + i\kappa_0 A_{(3-r)}(z,t) + \left(\widetilde{\alpha^{(r)}} * A_{(r)}\right)(z,t) + i\gamma \left|A_{(r)}(z,t)\right|^2 A_{(r)}(z,t) \tag{5.15}$$

where ($r = 1, 2$). Since the function $\alpha^{(r)}$ is defined in the frequency domain ($\alpha^{(r)} = \alpha^{(r)}(\omega)$) it is crucial to apply convolution according to the following property of Fourier transform $\widetilde{(f \cdot g)}(t) = (\tilde{f} * \tilde{g})(t)$. In our case, it is given by: $(\widetilde{\alpha^{(r)} \cdot \tilde{A}_{(r)}})(z,t) = (\widetilde{\alpha^{(r)}} * A_{(r)})(z,t)$.

For the simulation study using the simplified model, we used the optical parameters calculated at 1000 nm central wavelength reported in Table 5.1. All the parameters are the same for both cores. The estimated value for the gain/loss coefficients (7.49 m^{-1}) was included in the

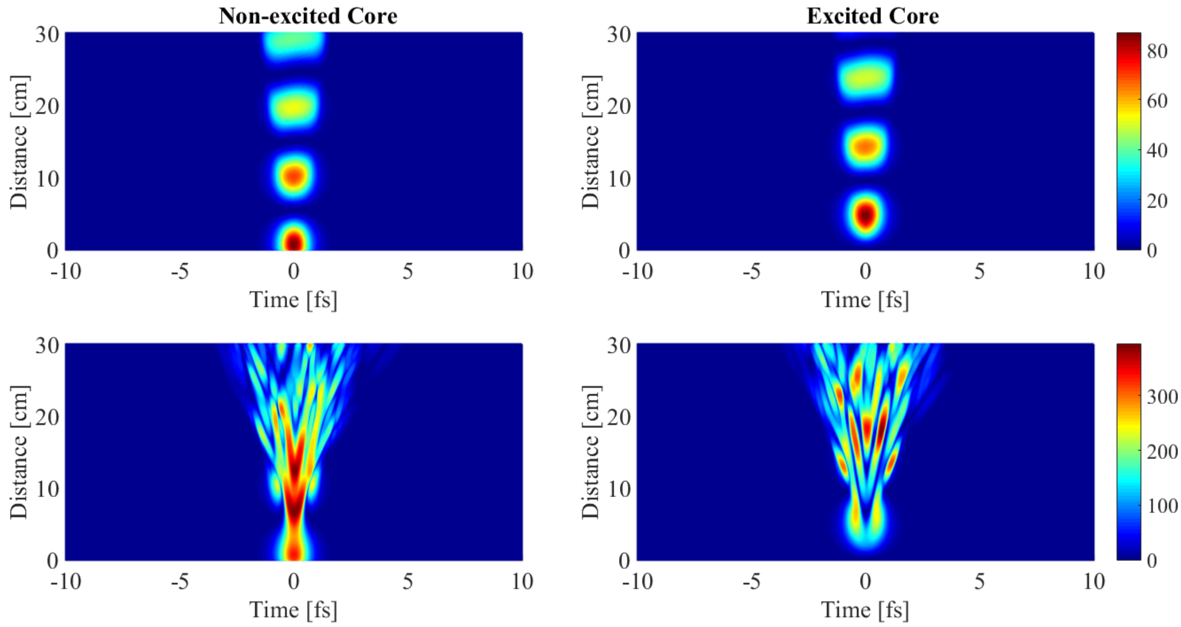

Fig. 5.5: *Time domain evolution of the field intensity in the excited (left) and non-excited (right) core under excitation by 1000 nm central wavelength and 1 ps width pulses with 100 pJ (top) and 430 pJ (bottom) energies, in the case of the gain channel (left) excitation of a 30 cm length fiber with structure as in Fig.5.2b.*

parameter α_0: it has a positive sign for losses, indicating power attenuation, while a negative one for gain, indicating power increase.

We generated, with our simplified model, 2D time-domain evolution plots with parameters corresponding to those used in Fig.5.5 and the difference was hard to notice. Therefore, in order to trace subtle differences we looked at the pulse shapes in the time domain at 4 specific fiber lengths for the two cases above. The result is shown in Fig.5.6 for input energies 100 pJ and 430 pJ, respectively. Solid lines present the results of the simulation obtained using the full

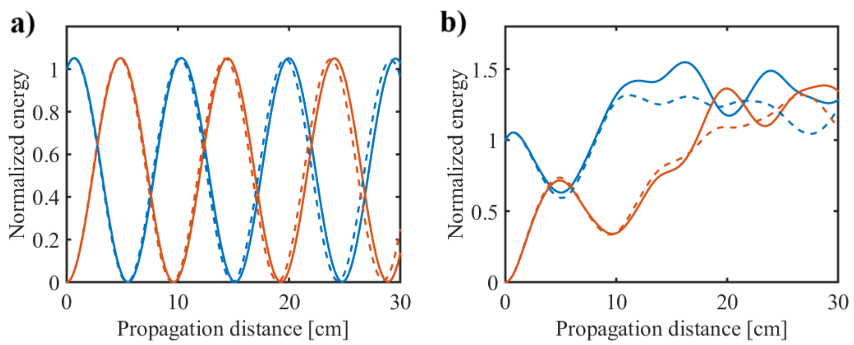

Fig. 5.6: *Normalized integrated energies in the corresponding channels at the corresponding energy levels of (a) 100 pJ and (b) 430 pJ for full (solid blue lines: gain channel, solid red lines: loss channel) and simplified model (dashed blue lines: gain channel, dashed red lines: loss channel).*

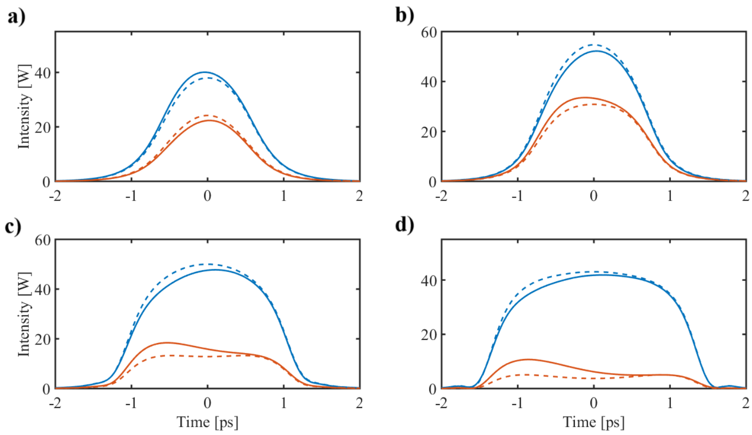

Fig. 5.7: *Snapshot of 100pJ pulses corresponding channels simulated in full model (solid blue lines: gain channel, solid red lines: gain channel) and simplified model (dashed blue lines: gain channel, dashed red lines: loss channel) at different propagation distances: a) 8 cm, b) 12 cm, c) 21 cm and d) 30 cm.*

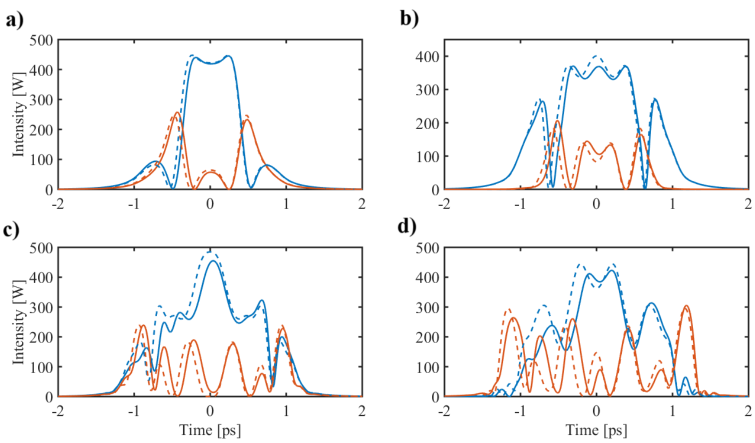

Fig. 5.8: *Snapshot of 430 pJ pulses corresponding channels simulated in full model (solid blue lines-gain channel, solid red lines-gain channel) and simplified model (dashed blue lines: gain channel, dashed red lines: loss channel) at different propagation distances: a) 8 cm, b) 10 cm, c) 12 cm and d) 14 cm.*

model (red: unexcited, loss channel; blue: excited, gain channel), while dashed lines present the ones obtained using the simplified model. In Fig.5.7, we compare pulse shapes generated by both methods; the four panels refer to lengths: (a) 8 cm, (b) 12 cm, (c) 21 cm, and (d) 30 cm. We observe that there is a close correspondence between the two models in each reported case. A small discrepancy between the two models is observed only on the rising edge of the pulse in the loss channel at 21 and 30 cm (i.e. between solid and dashed red lines of Fig.5.7c and d for t in the range -1.0 to 1.0). In Fig.5.8, which was calculated in the unstable regime, the four panels refer to lengths: (a) 8 cm, (b) 10 cm, (c) 12 cm, and (d) 14 cm. In this case, as observed in Fig.5.8c and d, the two models give significantly different results after 12 cm:

Table 5.1: *Optical linear and nonlinear parameters of the DCF in Fig.5.3b.*

λ_0 = 1000 nm	1st core	2nd core
β_2	$4.21 \cdot 10^{-25}$	
γ	0.3	
α_0	-7.49	7.49
κ_0	33.74153	

the solid and dashed curves significantly differ from each other. It is not a great surprise that in an unstable regime, propagation is sensitive to the fiber parameters used in the extended and simplified models. However, the good news is, that the position of the exceptional point, the border between stable and unstable regimes, in both models is very close. In conclusion, the simplified model *can be used* for finding critical intensity in the nonlinear regime.

5.5.3 The role of dispersion

In this section, we investigate the role of the dispersion of crucial parameters: intra-channel coupling, and gain/loss coefficient, on the stability of pulse propagation in a waveguide with two coupled channels. We restrict the analysis to the linear regime and study the dynamics described by the equation

$$\frac{\partial A_{(r)}}{\partial z} = -i\beta_2 \frac{\partial^2 A_{(r)}}{\partial t^2} + i\widetilde{\kappa} * A_{(3-r)} + \widetilde{\alpha} * A_{(r)}. \tag{5.16}$$

Note that we have two terms on the right-hand side of the equation (5.16) in the form of a convolution. Each of the functions κ and α are functions of frequency ω. For the current study, we have chosen Gaussian functions for all dispersion profiles and each of them is characterized by three parameters: width σ, central frequency ω_0, and maximum; for example, the inter-core coupling will be equal to

$$\kappa(\omega) = \kappa_0 \exp\left[(\omega - \omega_0)^2/\sigma_\kappa^2\right]. \tag{5.17}$$

The dispersion in the gain/loss coefficient $\alpha(\omega)$ is introduced by analogy. We have checked that our conclusions are the same if we use Lorenzian functions instead of Gaussians. In this formulation, the constant coefficient corresponds to the Gaussian function, which is a very broad function of frequency. In each of the studies reported below, we looked for the exceptional point that lies on the boundary between stable and unstable propagation regions. Unstable propagation is characterized by the exponential growth of the signal in the gain channel, while in the lossy channel, the pulse decays rapidly to zero.

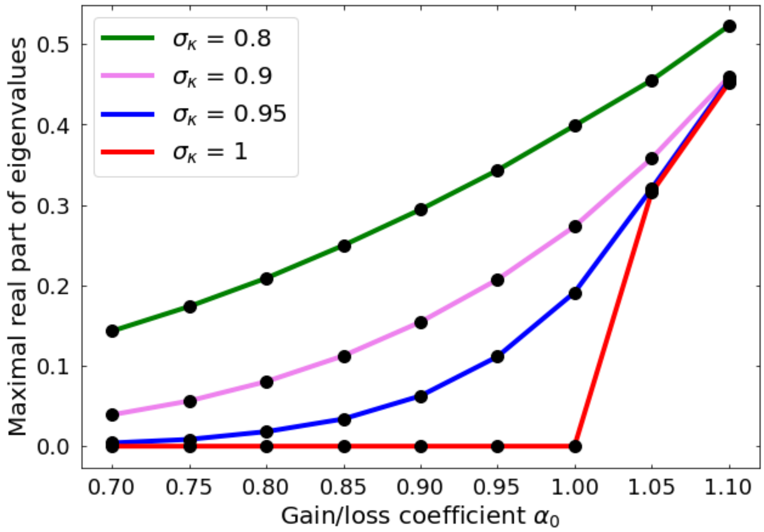

Fig. 5.9: *Maximum value of the real part of the eigenvalues for different amplitudes of the coupling coefficient. The width of the gain/loss coefficient is arbitrarily set equal to one, and the widths of the coupling coefficients as a function of ω are given in the inset. Note that in all cases where the width of the coupling is smaller than the width of the gain/loss coefficient, we do not observe stable propagation.*

In the case of linear propagation considered here, it is sufficient to examine the maximal real part of the eigenvalue $\mathrm{Re}(\lambda)_{\max}$ of the characteristic equation derived from Eq. (5.16). It is worth noting, that this result remains consistent regardless of the shape of intensity of the input pulse. In the nonlinear scenario, however, our approach becomes ineffective. Then, in order to predict the dynamics of the system and to identify the specific exceptional points, we must resort to direct simulations. The ability to find these exceptional points depends on various parameters associated with the channels, and this requires a different methodology compared to the linear case.

First, we considered the case where all coefficients are constant. In this case, the system becomes unstable when the magnitude of α is greater than the interchannel coupling κ, regardless of the value of the dispersion β_2, which is a well-known result. We then introduced the dispersion to κ and α in the manner described above. A summary of this study is shown in Fig. (5.9). We clearly observe that as long as the width of the coupling is greater than the gain/loss profile, we have a region of stable dynamics as long as $\kappa_0 > \alpha_0$. In the opposite case, when the width of the gain/loss function exceeds the width of the coupling function, $\mathrm{Re}(\lambda)_{\max}$ is always positive and tends to linear growth (with increasing value of α_0) as the gain/loss profiles become more and more narrow. This gives us a clue about the possible components of our system. If we include a small nonlinearity, we expect essentially the same characteristics, with the shift of the exceptional point.

Finally, we investigated, whether the center frequency for the gain/loss and coupling profiles need not be the same. To do this, we introduced the shift $\Delta = |\omega_{0,\alpha} - \omega_{0,\kappa}|$ between the two profiles and set the width of the inter-channel coupling to be several times greater than the width of the gain/loss parameter ($\sigma_\kappa = 6$ and $\sigma_\alpha = 1$). As illustrated in Fig. (5.10), so long as the shift between these two profiles remains smaller than the coupling width of the coupling (note that we arbitrarily choose the value of the gain/loss profile to be equal to one), an exceptional point appears. We have carried out thorough studies, including various coupling widths and shifts, to establish that the features shown in Fig. 5.10 are representative of a wide range of parameters, including the proposed configuration. The main insight from our simulations is that, for practical implementation, we should look for setups with consistent coupling and carefully study how the relative shifts of the resonances, in both κ and α coefficients, vary with frequency.

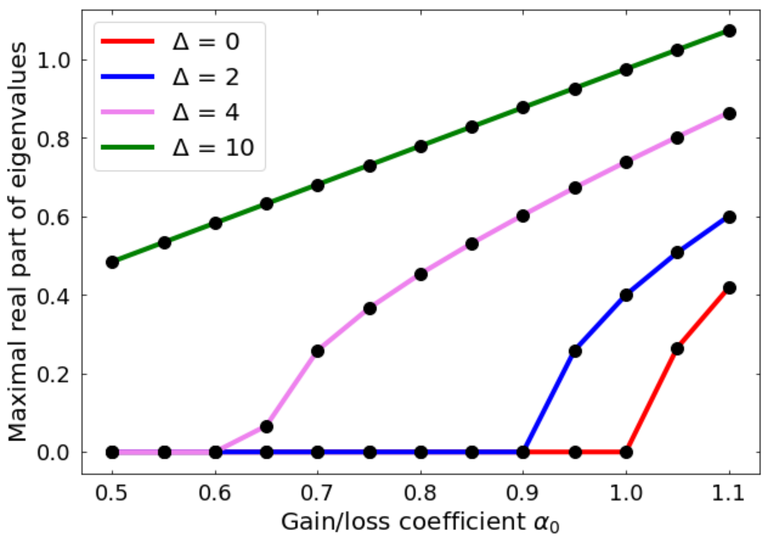

Fig. 5.10: *Maximal real part of eigenvalues in the case when gain/loss and interchannel coefficients are centered at frequencies shifted by Δ, as indicated in the inset. Other parameters are: $\sigma_\omega = 1$, $\sigma_\kappa = 6$ and $\kappa_0 = 1$.*

5.6 Conclusion

We predicted $\mathcal{PT}$-symmetry breaking in a dual-core photonic crystal fiber made of phosphate glasses synthesized in-house. The fiber cores are made of phosphate glasses with 6% mol ytterbium (gain channel) and 0.015% mol copper doping (loss channels) and have the following structural parameters: core diameters of 1.85 μm, lattice pitch of 1.6 μm, and extra photonic lattice of air holes with diameter 1.4 μm. The fiber exhibits normal dispersion of the fundamental supermodes in the range of 500-2000 nm and coupling length in the order of 5 cm at 1000 nm. We investigated the stability of the $\mathcal{PT}$-symmetric DCF system by simulating the propagation of hyperbolic secant pulses with a width of 10 ps and 1 ps: the system is stable considering both temporal widths and values of gain-loss/coupling coefficients ratio $\alpha/\kappa \leq 0.25$. The designed fiber resulted in a α/κ value of 0.22. Then, we solved the system of CGNLSE with the Split-Step method, considering excitation pulses with a wavelength of 1000 nm and width of 1 ps. We predicted two regimes of light propagation through the designed fiber: 1) linear oscillations of the pulse energy between the gain and loss channel ($\mathcal{PT}$-symmetry state); 2) unstable dynamics with strong enhancement in both channels (broken $\mathcal{PT}$-symmetry). Initial input energies were 100 pJ, and 430 pJ, respectively. The same scenarios were predicted considering pulses with the same input energy and using a simplified theoretical model, which only includes second-order dispersion term, linear coupling, first-order nonlinearity, and dispersive gain/loss coefficient. We carried out an extensive investigation of the influence of dispersion on both the gain/loss and the coupling. Our investigation led us to understand that stable dynamics prevail when the coupling width (σ_κ) exceeds the gain/loss profile width ($\sigma_\kappa > \sigma_\alpha$), while a linear growth of intensity is predicted in the opposite case. These predictions hold even when the relative frequency shift between the gain/loss and coupling profiles is taken into account. The results presented here represent a very promising prediction of $\mathcal{PT}$-symmetric breaking using a manufacturable dual-core optical fiber. This breakthrough has significant potential for several applications, including all-optical switching and the development of robust high-power lasers.

Conclusions

In this thesis, we presented the results of our study on all-optical switching of ultrashort soliton-like pulses using soft-glass DCFs. In particular, we investigated the coupling, asymmetrical, and nonlinear characteristics of the fiber using a simple theoretical model. Our goal was to provide valuable insight into the switching and self-trapping behavior, along with predicting the set of parameters that yield efficient switching performance. The numerical results were compared with experimental data to analyze the advantages and limits of the simple model for DCFs.

In the first part of the study, we started from the simplest case of a linear coupled system, which was analytically solved, to show the effect of asymmetry on the coupler. Subsequently, we study the effect of high nonlinearity on a symmetrical system by modeling the high nonlinear symmetrical soft-glass DCF. This attempt effectively demonstrated that the simple model was capable of capturing both the qualitative and quantitative aspects of symmetrical DCF.

In the next part, we proceeded to examine the combined effect of both asymmetry and nonlinearity within one coupled system, that is, highly nonlinear asymmetrical DCFs made of the same material. In this context, our theoretical model, while showing reasonable quantitative agreement with experimental data, also revealed the system's remarkable sensitivity to even slight variations in either asymmetry or nonlinearity parameters.

In addition to this, we conducted a thorough numerical investigation of different approaches aimed at enhancing switching performance, utilizing dual-wavelength configurations within asymmetrical DCFs. This investigation not only explained the switching mechanism and the observed spectral broadening effect in experimental setups but also yielded optimized parameter values for enhanced energy transfer.

Lastly, we introduced a feasible fiber structure grounded in the concept of PT symmetry, employing a simplified model. By identifying the exceptional points within the PT symmetry system, we derived the stability limits for the fiber design. This study on PT-symmetrical fibers lays the groundwork for future endeavors in fiber fabrication and experimental exploration.

Appendix A

The Split-Step Fourier method

The Split-Step Fourier method is a powerful pseudo-spectral numerical method used to solve nonlinear partial differential equations, such as the nonlinear Schrodinger equation. This method derives its name from two key features: the computation of solutions in small steps, where the linear and nonlinear steps are treated separately, and the requirement to Fourier transform back and forth since the linear step is taken in the frequency domain and the nonlinear step is taken in the time domain.

Compared to other methods, the Split-Step Fourier method offers high accuracy and fast computational speed. In this thesis, we introduce the Split-Step Fourier method for the solution of a single nonlinear Schrodinger equation, and then extend the approach to the more complex case of coupled nonlinear Schrodinger equations.

By employing this method, we can obtain accurate numerical solutions for a wide range of nonlinear partial differential equations, making it an invaluable tool for researchers across multiple scientific fields.

A.1 Time differentiation property of Fourier transform

The Split-Step Fourier method takes advantage of the time differentiation property of the Fourier transform. It is much more accurate with other methods of differentiation, for instance, the finite difference method, with giving time of computation. Let us define the Fourier transform of a continuous-time function $A(t)$ as:

$$\tilde{A}(\omega) = \int_{-\infty}^{\infty} A(t) e^{-i\omega t} dt. \tag{A.1}$$

The inverse Fourier transform is defined as:

$$A(t) = \frac{1}{2\pi} \int_{-\infty}^{\infty} \tilde{A}(\omega) e^{i\omega t} d\omega. \tag{A.2}$$

Then, the differentiation of a function in the time domain is equivalent to the multiplication of its Fourier transform by a factor $i\omega$ in the frequency domain:

$$\frac{\partial^n A(t)}{\partial t^n} = \frac{1}{2\pi} \int_{-\infty}^{\infty} \tilde{A}(\omega) \frac{\partial^n}{\partial t^n} [e^{i\omega t}] d\omega = \frac{1}{2\pi} \int_{-\infty}^{\infty} \tilde{A}(\omega) i\omega e^{i\omega t} d\omega. \tag{A.3}$$

In numerical simulations, the Fast Fourier Transform (FFT) algorithm is commonly used to facilitate the transformation of data between the time and frequency domains.

$$\frac{\partial^n A}{\partial t^n} = \mathcal{F}^{-1}\{(i\omega)^n \mathcal{F}[A(\omega)]\}. \tag{A.4}$$

A.2 The Split-Step Fourier method for nonlinear Schrodinger equation

Consider the NLSE in single core:

$$i\frac{\partial A}{\partial z} = -\frac{\beta_2}{2} \frac{\partial^2 A}{\partial \tau^2} - \gamma |A|^2 A. \tag{A.5}$$

Here, the retarded time $\tau = t - \beta_1 z$ is used to keep the pulse in the defined temporal window. We define operators $\hat{D}$ and $\hat{N}$ from above equation as

$$\hat{D} = -\frac{\beta_2}{2} \frac{\partial^2 A}{\partial \tau^2}, \tag{A.6}$$

$$\hat{N} = -\gamma |A|^2. \tag{A.7}$$

The equation (A.5) becomes:

$$i\frac{\partial A}{\partial z} = \hat{D}A + \hat{N}A. \tag{A.8}$$

If the step size Δz along the propagation direction z is sufficiently small, $\hat{N}$ can be considered constant and the exact solution of this equation at the next step along the propagation direction can be formally written as

$$A(\tau, \Delta z) = e^{-i\Delta z(\hat{D}+\hat{N})} A(\tau, 0). \tag{A.9}$$

Applying both operators at once is not possible during numerical integration. The idea of the split-step method is to approximate $e^{i\Delta z(\hat{D}+\hat{N})}$ by a sequence of split operators as:

$$e^{-i\Delta z(\hat{D}+\hat{N})} \approx e^{-ib_n\hat{N}} e^{-ia_n\Delta z\hat{D}} ... e^{-ib_1\Delta z\hat{N}} e^{-ia_1\Delta z\hat{D}}, \tag{A.10}$$

where coefficients a_j and b_j are constants. The simplest split-step scheme is when we take $a_1 = b_1 = 1$ and other coefficients to be zero. In this case, we get

$$e^{-i\Delta z(\hat{D}+\hat{N})} \approx e^{-i\Delta z\hat{D}} e^{-i\Delta z\hat{N}}. \tag{A.11}$$

This splitting scheme is first-order accurate in time. First, the linear half-step is calculated in the spectral domain. Then, the partial solution is transferred to the time domain using the FFT algorithm and the nonlinear step is calculated. In the end, the solution is transferred back to the spectral domain, and the first linear half-step is applied. The solution takes this form:

$$A(z_0 + \Delta z) = \mathcal{F}^{-1}\{e^{-i\Delta\omega^2 z\beta_2/2}\mathcal{F}[A(z_0)e^{-i\Delta z\gamma|A(z,\tau)|^2}]\}. \tag{A.12}$$

A.3 The Split-Step Fourier method for coupled NLSEs

Consider the coupled NLSE

$$\begin{aligned} i\frac{\partial A_1}{\partial z} &= -\frac{\beta_2}{2}\frac{\partial^2 A_1}{\partial \tau^2} - \gamma|A_1|^2 A_1 - \kappa A_2, \\ i\frac{\partial A_2}{\partial z} &= -\frac{\beta_2}{2}\frac{\partial^2 A_2}{\partial \tau^2} - \gamma|A_2|^2 A_2 - \kappa A_1. \end{aligned} \tag{A.13}$$

The coupled nonlinear Schrodinger equation can be written in the operator form as follows:

$$i\frac{\partial A(z,\tau)}{\partial z} = \hat{M} A(z,\tau), \tag{A.14}$$

where $A(z,\tau)$ is the total field in the coupler defined as a column vector of two fields in the two channel:

$$A(z,\tau) = \begin{bmatrix} A_1(z,\tau) \\ A_2(z,\tau) \end{bmatrix} \tag{A.15}$$

and $\hat{M}$ is a matrix operator defined as

$$\hat{M} = \hat{L} + \hat{N} = \begin{bmatrix} \hat{D_1} & \hat{C_1} \\ \hat{C_2} & \hat{D_2} \end{bmatrix} + \begin{bmatrix} \hat{N_1} & 0 \\ 0 & \hat{N_2} \end{bmatrix}. \tag{A.16}$$

The dispersion $\hat{D_m}$ and nonlinear $\hat{N_m}$ operators for m-th fiber core are defined as same as in the case of a single core. The coupling $\hat{C_m}$ operator in symmetrical coupler is defined as:

$$\hat{C_m} = \kappa. \tag{A.17}$$

The composition of the one-step solution is performed for the dual-core case using the second-order Split-Step scheme written as

$$A(z_0 + \Delta z, \tau) = e^{-i\Delta z \hat{M}} A(z_0,\tau) \approx e^{-i\Delta z \hat{N}} e^{-i\Delta z \hat{L}} A(z_0,\tau). \tag{A.18}$$

Exponential of $\hat{L}$ and $\hat{N}$ in matrix form respectively are:

$$\begin{aligned} e^{\Delta z \hat{L}} &= \exp\left\{ \Delta z \begin{bmatrix} \hat{D_1} & \hat{C_1} \\ \hat{C_2} & \hat{D_2} \end{bmatrix} \right\} = \begin{bmatrix} e^{-i\Delta z \omega^2 \beta_2/2} & 0 \\ 0 & e^{-i\Delta z \omega^2 \beta_2/2} \end{bmatrix} \times \\ &\times \begin{bmatrix} \cos \Delta z \kappa & i \sin \Delta z \kappa \\ i \sin \Delta z \kappa & \cos \Delta z \kappa \end{bmatrix} \end{aligned} \tag{A.19}$$

$$e^{\Delta z \hat{N}} = \exp\left\{ \Delta z \begin{bmatrix} \hat{N_1} & 0 \\ 0 & \hat{N_2} \end{bmatrix} \right\} = \begin{bmatrix} e^{-i\Delta z \gamma |A|^2} & 0 \\ 0 & e^{-i\Delta z \gamma |A|^2} \end{bmatrix}. \tag{A.20}$$

Here, we consider the coupling as a constant, which is equivalent to the zeroth order term of Taylor's expansion of coupling function $\kappa(\omega)$. If the higher-order coupling is taken into account, the matrix calculation above can also be used. In the case of higher order coupling, the matrix elements in (A.18) will consist of cos and sin of $\kappa_0 + \omega\kappa_1 + \omega^2\kappa_2 + ...$ When the full function

$\kappa(\omega)$ is considered, we just simply replace κ with $\kappa(\omega)$ everywhere in the matrix element. Put the resulting matrices at (A.18) and (A.19) together, we obtain the solution of $A(z_0 + \Delta z)$ in first order spit-step scheme as

$$\begin{aligned} A(z_0 + \Delta z) =& \mathcal{F}^{-1}\left\{ \begin{bmatrix} e^{-i\Delta z\omega^2/2} & 0 \\ 0 & e^{-i\Delta z\omega^2/2} \end{bmatrix} \mathcal{F}\left[\begin{bmatrix} \cos\Delta z\kappa & i\sin\Delta z\kappa \\ i\sin\Delta z\kappa & \cos\Delta z\kappa \end{bmatrix} \times \right.\right. \\ & \left.\left. \times \begin{bmatrix} e^{i\Delta z|A|^2} & 0 \\ 0 & e^{i\Delta z|A|^2} \end{bmatrix} \begin{bmatrix} A_1(z,\tau) \\ A_2(z,\tau) \end{bmatrix} \right]\right\}. \end{aligned} \tag{A.21}$$

A.4 Numerical Stability of Split-Step Methods

Solving equations (A.5) using the split-step method could be very accurate and fast with relatively large time and distance steps in comparison with other well-known methods. However, this does not mean the split-step method is unconditionally stable. In fact, the derived scheme above could lose it accuracy if we use it with large Δz for a very long propagation distance (such as to $z = 200$). In such cases, high-frequency Fourier modes will become prominent creating numerical instability. Below we will extend that analysis to derive stability conditions for the first-order split-step methods on the NLSE Let us consider split-step methods as applied to the NLSE (A.5). The NLSE (A.5) admits an exact x-independent solution

$$A(z,\tau) = ae^{2i|a|^2 z}, \tag{A.22}$$

where a is a constant. Since the NLSE is phase invariant, we take a to be a real number. When this solution is perturbed to

$$A(z,\tau) = e^{2ia^2 z}[a + \delta A(z,\tau)], \quad \delta A(z,\tau) \ll 1. \tag{A.23}$$

We now analyze how the perturbation $\delta A(z,\tau)$ evolves under the split-step scheme $e^{-i\Delta z\hat{M}}$. Substituting (A.23) into (A.12) and neglecting terms of $\delta A(z,\tau)$ and higher, we obtain the iteration equation for the perturbation as

$$\Psi(z_0 + \Delta z) = e^{-i\Delta z\hat{M}}\Psi(z_0) = e^{\Delta z\hat{D}}e^{\Delta z\hat{N}}\Psi(z_0), \tag{A.24}$$

where $\Psi(z_0) = \mathcal{F}[\delta A(z_0), \delta A(z_0)^*]^T$ and

$$e^{\Delta z \hat{D}} = \begin{bmatrix} e^{-i\omega^2 \Delta z/2} & 0 \\ 0 & e^{-i\omega^2 \Delta z/2} \end{bmatrix}, \quad e^{\Delta z \hat{N}} = \begin{bmatrix} 1 + 2ia^2\Delta z & 2ia^2\Delta z \\ 2ia^2\Delta z & 1 + 2ia^2\Delta z \end{bmatrix}. \tag{A.25}$$

The $e^{\Delta z \hat{D}}$ and the $e^{\Delta z \hat{N}}$ matrices respectively give the perturbation iteration after the linear step and the nonlinear step of the method. Therefore, eigenvalues of the iteration matrix $e^{-i\Delta z \hat{M}}$ determine if the perturbations will grow or not. Since $\det\left(e^{-i\Delta z \hat{M}}\right) = 1$, eigenvalues of $e^{-i\Delta z \hat{M}}$ are

$$\lambda = \rho \pm \sqrt{\rho^2 - 1}, \tag{A.26}$$

where

$$\rho = \frac{1}{2}\operatorname{Tr}\left(e^{-i\Delta z \hat{M}}\right) = \cos\left(\omega^2 \Delta z\right) + 2a^2 \Delta z \sin\left(\omega^2 \Delta z\right). \tag{A.27}$$

Perturbations will grow if $|\lambda| > 1$, i.e., when $|\rho| > 1$. Rewriting ρ as [87]

$$\rho = r \cos\left(\omega^2 \Delta z - \theta\right), \tag{A.28}$$

where

$$r = \sqrt{1 + 4a^4 \Delta z^2}, \quad \operatorname{tg}\theta = 2a^2\Delta z, \quad 0 < \theta < \frac{1}{2}\pi. \tag{A.29}$$

Unstable Fourier modes are associated with frequencies in the intervals [87]

$$0 < \text{mod}(\omega^2 \Delta z, \pi) < 2\theta. \tag{A.30}$$

The largest growth occurs at frequency where $\text{mod}(\omega^2 \Delta z, \pi) = \theta$, which can be written as:

$$|\lambda|_{max} = \sqrt{1 + 4a^4 \Delta z^2} + 2a^2 \Delta. \tag{A.31}$$

It is important to note that, the first interval of unstable modes

$$0 < \omega^2 \Delta z < 2\theta \tag{A.32}$$

is not induced by numerical instability. Rather it is caused by modulation instability of the constant solution (A.22) in the NLS equation (A.5). The other intervals

$$\omega^2 \Delta z \in (\pi, \pi + 2\theta), (2\pi, 2\pi + 2\theta), ... \tag{A.33}$$

are true intervals of numerical instability. In the numerical implementation of the split-step method in A.12, the Fourier frequency is discrete:

$$\omega = 0, \pm\omega_0, \pm 2\omega_0, ..., \pm\frac{1}{N}\omega_0, \tag{A.34}$$

where $\omega_0 = 2\pi/T$ is the frequency separation, T is the length of the computational interval, and N is the number of temporal grid points. Thus, to avoid numerical instability occurring during calculation, it is necessary and sufficient to keep none of these discrete Fourier frequencies (A.34 falls in the numerical-instability intervals (A.33). Note that the largest discrete Fourier frequency in A.34 is [87]

$$|\omega|_{max} = \frac{N\omega_0}{2} = \frac{\pi}{\Delta t}. \tag{A.35}$$

Thus a sufficient condition for numerical stability of split-step methods is $|\omega|^2_{max}\Delta z = \pi$ i.e. [87]

$$\frac{\Delta t}{\Delta z^2} \leq \frac{1}{\pi}. \tag{A.36}$$

If the time-step condition (A.36) is not met, some of the discrete Fourier frequencies (A.33) may fall in the unstable intervals (A.32), causing numerical instability.

List of acronyms

CGNLSE Coupled generalized nonlinear Schrödinger equation. 117

CW Continuous wave. 48

DCF Dual-core fiber. 74, 77, 85, 87, 127

DFG Difference frequency generation. 20

FFT Fast Fourier transform. 13, 131

FWHM Full width at half-maximum. 63, 77, 81, 98

FWM Four-wave mixing. 26

GVD Group velocity dispersion. 39, 42, 47, 48, 57, 62, 63, 70

NIR Near-infrared. 59

NLSE Nonlinear Schrödinger equation. 13, 61, 62, 64, 70, 73, 133

PCF Photonic crystal fiber. 5

SEM Scanning electron microscope. 113

SFG Sum frequency generation. 20

SPM Self-phase modulation. 29

SVEA Slowly-varying envelope aproximation. 27

XPM	Cross-phase modulation. 29

List of Figures

List of Tables

Bibliography

[1] Chapter 2 - fiber couplers. In Govind P. Agrawal, editor, *Applications of Nonlinear Fiber Optics (Second Edition)*, pages 54–99. Academic Press, Burlington, second edition edition, 2008.

[2] Junkichi Satsuma and Nobuo Yajima. B. Initial Value Problems of One-Dimensional Self-Modulation of Nonlinear Waves in Dispersive Media. *Progress of Theoretical Physics Supplement*, 55:284–306, 01 1974.

[3] G. P. Agrawal. Chapter 5 - optical solitons. In Govind Agrawal, editor, *Nonlinear Fiber Optics (Fifth Edition)*, Optics and Photonics, pages 129 – 191. Academic Press, Boston, fifth edition edition, 2013.

[4] *Basics of photonic crystal fibers*, pages 7–52. Springer Netherlands, Dordrecht, 2007.

[5] Ryszard Buczynski. Photonic crystal fibers. *Acta Physica Polonica Series a*, 106, 08 2004.

[6] J. C. Knight, T. A. Birks, P. St. J. Russell, and D. M. Atkin. All-silica single-mode optical fiber with photonic crystal cladding. *Opt. Lett.*, 21(19):1547–1549, Oct 1996.

[7] John M. Dudley, Goëry Genty, and Stéphane Coen. Supercontinuum generation in photonic crystal fiber. *Rev. Mod. Phys.*, 78:1135–1184, Oct 2006.

[8] Peiguang Yan, Gelin Zhang, Huifeng Wei, Deqin Ouyang, Shisheng Huang, Junqing Zhao, Kangkang Chen, Jie Luo, and Shuangchen Ruan. Double cladding seven-core photonic crystal fibers with different gvd properties and fundamental supermode output. *Lightwave Technology, Journal of*, 31:3658–3662, 12 2013.

[9] Philip St.J. Russell. Photonic-crystal fibers. *J. Lightwave Technol.*, 24(12):4729–4749, Dec 2006.

[10] Kentaro Kaneshima, Yoshinori Namihira, Nianyu Zou, Hiroki Higa, and Yasunori Nagata. Numerical investigation of octagonal photonic crystal fibers with strong confinement field. *IEICE Trans. Electron.*, 89-C:830–837, 2006.

[11] Huseyin Ademgil and Shyqyri Haxha. Design and optimisation of photonic crystal fibres for applications in communication systems. In *World Congress on Engineering*, 2007.

[12] Ana M.R. Pinto and Manuel Lopez-Amo. All-fiber lasers through photonic crystal fibers. *Nanophotonics*, 2(5-6):355–368, 2013.

[13] S. Tripathy and Jsn Achary. Nonlinear rectangular photonic crystal fiber (pcf) for optical communication exclusively super continuum generation. *Journal of Lasers, Optics & Photonics*, 02, 01 2015.

[14] P. Russell, Ramin Beravat, and Gordon Wong. Helically twisted photonic crystal fibres. *Philosophical Transactions of The Royal Society A Mathematical Physical and Engineering Sciences*, 375:20150440, 02 2017.

[15] Arati Shah and Rajesh Kumar. *A Review on Photonic Crystal Fibers*, pages 1241–1249. 01 2020.

[16] Govind Agrawal. Chapter 1 - introduction. In Govind Agrawal, editor, *Nonlinear Fiber Optics (Fifth Edition)*, Optics and Photonics, pages 1–25. Academic Press, Boston, fifth edition edition, 2013.

[17] S. Jensen. The nonlinear coherent coupler. *IEEE Journal of Quantum Electronics*, 18(10):1580–1583, 1982.

[18] A A Maĭer. Optical transistors and bistable devices utilizing nonlinear transmission of light in systems with undirectional coupled waves. *Soviet Journal of Quantum Electronics*, 12(11):1490, nov 1982.

[19] Rongqing Hui. Chapter 6 - passive optical components. In Rongqing Hui, editor, *Introduction to Fiber-Optic Communications*, pages 209–297. Academic Press, 2020.

[20] S. R. Friberg, A. M. Weiner, Y. Silberberg, B. G. Sfez, and P. S. Smith. Femotosecond switching in a dual-core-fiber nonlinear coupler. *Opt. Lett.*, 13(10):904–906, Oct 1988.

[21] George I. Stegeman and Alan Miller. Chapter 5 - physics of all-optical switching devices. In John E. Midwinter, editor, *Photonics in Switching*, pages 81–145. Academic Press, San Diego, 1993.

[22] S. Trillo, S. Wabnitz, E. M. Wright, and G. I. Stegeman. Soliton switching in fiber nonlinear directional couplers. *Opt. Lett.*, 13(8):672–674, Aug 1988.

[23] M. Romagnoli, S. Trillo, and S. Wabnitz. Soliton switching in nonlinear couplers. *Optical and Quantum Electronics*, 24(11):S1237–S1267, nov 1992.

[24] Yuri S. Kivshar. Switching dynamics of solitons in fiber directional couplers. *Opt. Lett.*, 18(1):7–9, Jan 1993.

[25] Pak L. Chu, Yuri S. Kivshar, Boris A. Malomed, Gang-Ding Peng, and Manuel L. Quiroga-Teixeiro. Soliton controlling, switching, and splitting in nonlinear fused-fiber couplers. *J. Opt. Soc. Am. B*, 12(5):898–903, May 1995.

[26] Kin S. Chiang. Intermodal dispersion in two-core optical fibers. *Opt. Lett.*, 20(9):997–999, May 1995.

[27] I. M. Uzunov, R. Muschall, M. Gölles, Yuri S. Kivshar, B. A. Malomed, and F. Lederer. Pulse switching in nonlinear fiber directional couplers. *Phys. Rev. E*, 51:2527–2537, Mar 1995.

[28] Rodislav Driben and Boris A. Malomed. Stability of solitons in parity-time-symmetric couplers. *Opt. Lett.*, 36(22):4323–4325, Nov 2011.

[29] A. Betlej, S. Suntsov, K. G. Makris, L. Jankovic, D. N. Christodoulides, G. I. Stegeman, J. Fini, R. T. Bise, and D. J. DiGiovanni. All-optical switching and multifrequency generation in a dual-core photonic crystal fiber. *Opt. Lett.*, 31(10):1480–1482, May 2006.

[30] Pavol Stajanca, Dariusz Pysz, Giedrius Andriukaitis, Tadas Balciunas, Guangyu Fan, Andrius Baltuska, and Ignac Bugar. Ultrafast multi-wavelength switch based on dynamics of spectrally-shifted solitons in a dual-core photonic crystal fiber. *Opt. Express*, 22(25):31092–31101, Dec 2014.

[31] J. Herrmann, U. Griebner, N. Zhavoronkov, A. Husakou, D. Nickel, J. C. Knight, W. J. Wadsworth, P. St. J. Russell, and G. Korn. Experimental evidence for supercontinuum generation by fission of higher-order solitons in photonic fibers. *Phys. Rev. Lett.*, 88:173901, Apr 2002.

[32] P Stajanca and I Bugar. Nonlinear ultrafast switching based on soliton self-trapping in dual-core photonic crystal fibre. *Laser Physics Letters*, 13(11):116201, sep 2016.

[33] S. Minardi, F. Eilenberger, Y. V. Kartashov, A. Szameit, U. Röpke, J. Kobelke, K. Schuster, H. Bartelt, S. Nolte, L. Torner, F. Lederer, A. Tünnermann, and T. Pertsch. Three-dimensional light bullets in arrays of waveguides. *Phys. Rev. Lett.*, 105:263901, Dec 2010.

[34] M. Longobucco, J. Cimek, L. Čurilla, D. Pysz, R. Buczyński, and I. Bugár. All-optical switching based on soliton self-trapping in dual-core high-contrast optical fibre. *Optical Fiber Technology*, 51:48–58, 2019.

[35] M Longobucco, P Stajanča, L Čurilla, R Buczyński, and I Bugár. Applicable ultrafast all-optical switching by soliton self-trapping in high index contrast dual-core fibre. *Laser Physics Letters*, 17(2):025102, jan 2020.

[36] L. Curilla, I. Astrauskas, A. Pugzlys, P. Stajanca, D. Pysz, F. Uherek, A. Baltuska, and I. Bugar. Nonlinear performance of asymmetric coupler based on dual-core photonic crystal fiber: Towards sub-nanojoule solitonic ultrafast all-optical switching. *Optical Fiber Technology*, 42:39–49, 2018.

[37] Jarosław Cimek, Ryszard Stępień, Grzegorz Stępniewski, Bartłomiej Siwicki, Paulina Stafiej, Mariusz Klimczak, Dariusz Pysz, and Ryszard Buczyński. High contrast glasses for all-solid fibers fabrication. *Optical Materials*, 62:159–163, 2016.

[38] M. Longobucco, I. Astrauskas, A. Pugžlys, D. Pysz, F. Uherek, A. Baltuška, R. Buczyński, and I. Bugár. Broadband self-switching of femtosecond pulses in highly nonlinear high index contrast dual-core fibre. *Optics Communications*, 472:126043, 2020.

[39] M. Liu and K. S. Chiang. Propagation of ultrashort pulses in a nonlinear two-core photonic crystal fiber. *Applied Physics B*, 98(4):815–820, dec 2009.

[40] Jiaqi Zhao, Zhi Wang, Yange Liu, and Bo Liu. Switchable-multi-wavelength fiber laser based on dual-core all-solid photonic bandgap fiber. *Frontiers of Optoelectronics in China*, 3(3):283–288, jul 2010.

[41] Jin Hua Li, Kin Seng Chiang, and Kwok Wing Chow. Switching of ultrashort pulses in nonlinear high-birefringence two-core optical fibers. *Optics Communications*, 318:11–16, 2014.

[42] Gang-Ding Peng, editor. *Handbook of Optical Fibers*. Springer Singapore, 2019.

[43] Jaroslaw Cimek, Nikos Liaros, Stelios Couris, Ryszard Stępień, Mariusz Klimczak, and Ryszard Buczyński. Experimental investigation of the nonlinear refractive index of various soft glasses dedicated for development of nonlinear photonic crystal fibers. *Opt. Mater. Express*, 7(10):3471–3483, Oct 2017.

[44] Viet Hung Nguyen, Le Xuan The Tai, Ignac Bugar, Mattia Longobucco, Ryszard Buczyński, Boris A. Malomed, and Marek Trippenbach. Reversible ultrafast soliton switching in dual-core highly nonlinear optical fibers. *Opt. Lett.*, 45(18):5221–5224, Sep 2020.

[45] Mattia Longobucco, Ignas Astrauskas, Audrius Pugžlys, Nhat Thai Dang, Dariusz Pysz, František Uherek, Andrius Baltuška, Ryszard Buczyński, and Ignác Bugár. Complex study of solitonic ultrafast self-switching in slightly asymmetric dual-core fibers. *Appl. Opt.*, 60(32):10191–10198, Nov 2021.

[46] M. Longobucco, J. Cimek, D. Pysz, R. Buczyński, and I. Bugár. All-optical switching of ultrafast solitons at 1560 nm in dual-core fibers with high contrast of refractive index. *Optical Fiber Technology*, 63:102514, 2021.

[47] Govind P. Agrawal. Chapter 6 - pulse compression. In Govind P. Agrawal, editor, *Applications of Nonlinear Fiber Optics*, pages 263–318. Academic Press, San Diego, 2001.

[48] Mattia Longobucco, Ignas Astrauskas, Audrius Pugžlys, Dariusz Pysz, František Uherek, Andrius Baltuška, Ryszard Buczyński, and Ignác Bugár. High contrast all-optical dual wavelength switching of femtosecond pulses in soft glass dual-core optical fiber. *Journal of Lightwave Technology*, 39(15):5111–5117, 2021.

[49] Viet Hung Nguyen, Le Xuan The Tai, Mattia Longobucco, Ryszard Buczyński, Ignac Bugar, Ignas Astrauskas, Audrius Pugzlys, Andrius Baltuska, and Marek Trippenbach Boris Malomed. Self-trapping and switching of solitonic pulses in mismatched dual-core highly nonlinear fibers. *Chaos, Solitons and Fractals*, 167:113045, feb 2023.

[50] Mattia Longobucco, Ignas Astrauskas, Audrius Pugžlys, Nhat Thai Dang, Dariusz Pysz, František Uherek, Andrius Baltuška, Ryszard Buczyński, and Ignác Bugár. Two all-optical switching schemes of 1560 nm femtosecond pulses using soft glass asymmetric dual-core fibers. In Shibin Jiang and Michel J. F. Digonnet, editors, *Optical Components and Materials XIX*, volume 11997, page 119970N. International Society for Optics and Photonics, SPIE, 2022.

[51] Carl M. Bender and Stefan Boettcher. Real spectra in non-hermitian hamiltonians having pt symmetry. *Physical Review Letters*, 80:5243–5246, 1997.

[52] Ali Mostafazadeh. Exact $\mathcal{PT}$-symmetry is equivalent to hermiticity. *Journal of Physics A: Mathematical and General*, 36(25):7081, jun 2003.

[53] C. M. Bender, P. E. Dorey, A. Fring C. Dunning, D. W. Hook, H. F. Jones, S. Kuzhel, G. Lévai, and R. Tateo. *Basics of $\mathcal{PT}$ Symmetry*, chapter Chapter 1, pages 3–38. World Scientific, jun 2019.

[54] Chao Hang, Guoxiang Huang, and V. Konotop. Pt symmetry with a system of three-level atoms. *Physical review letters*, 110:083604, 02 2013.

[55] Carl M. Bender, Bjorn K. Berntson, David Parker, and E. Samuel. Observation of pt phase transition in a simple mechanical system. *AMERICAN JOURNAL OF PHYSICS*, 81(3):173–179, February 2013.

[56] Joseph Schindler, Ang Li, Mei C. Zheng, F. M. Ellis, and Tsampikos Kottos. Experimental study of active lrc circuits with $\mathcal{PT}$ symmetries. *Phys. Rev. A*, 84:040101, Oct 2011.

[57] Hossein Hodaei, Mohammad-Ali Miri, Matthias Heinrich, Demetrios Christodoulides, and Mercedeh Khajavikhan. Parity-time-symmetric microring lasers. *Science (New York, N.Y.)*, 346:975–8, 11 2014.

[58] Hossein Hodaei, Absar Hassan, Steffen Wittek, Hipolito Garcia-Gracia, Ramy Elganainy, Demetrios Christodoulides, and Mercedeh Khajavikhan. Enhanced sensitivity at higher-order exceptional points. *Nature*, 548:187–191, 08 2017.

[59] Vladimir V. Konotop, Jianke Yang, and Dmitry A. Zezyulin. Nonlinear waves in $\mathcal{PT}$-symmetric systems. *Rev. Mod. Phys.*, 88:035002, Jul 2016.

[60] A Ruschhaupt, F. Delgado, and J. Muga. Physical realization of pt-symmetric potential scattering in a planar slab waveguide. *Journal of Physics A: Mathematical and General*, 38:L171, 02 2005.

[61] Liyou Luo, Jie Luo, Hongchen Chu, and Yun Lai. Pseudo-hermitian systems constructed by transformation optics with robustly balanced loss and gain. *Advanced Photonics Research*, 2(2):2000081, 2021.

[62] Ali Mostafazadeh. Pseudo-hermiticity versus pt symmetry: The necessary condition for the reality of the spectrum of a non-hermitian hamiltonian. *J. Math. Phys.*, 43(1):205–214, Jan 2002.

[63] A A Zyablovsky, A P Vinogradov, A A Pukhov, A V Dorofeenko, and A A Lisyansky. Pt-symmetry in optics. *Physics-Uspekhi*, 57(11):1063, nov 2014.

[64] K. Li, D. A. Zezyulin, P. G. Kevrekidis, V. V. Konotop, and F. Kh. Abdullaev. $\mathcal{PT}$-symmetric coupler with $\chi^{(2)}$ nonlinearity. *Phys. Rev. A*, 88:053820, Nov 2013.

[65] Zin Lin, Hamidreza Ramezani, Toni Eichelkraut, Tsampikos Kottos, Hui Cao, and Demetrios N. Christodoulides. Unidirectional invisibility induced by $\mathcal{PT}$-symmetric periodic structures. *Phys. Rev. Lett.*, 106:213901, May 2011.

[66] A. Regensburger, C Bersch, MA. Miri, Georgy Onishchukov, Demetrios N. Christodoulides, and Ulf Peschel. Parity–time synthetic photonic lattices. *Nature*, 488:167–171, Aug 2012.

[67] Absar U. Hassan, Hossein Hodaei, Mohammad-Ali Miri, Mercedeh Khajavikhan, and Demetrios N. Christodoulides. Nonlinear reversal of the $\mathcal{PT}$-symmetric phase transition in a system of coupled semiconductor microring resonators. *Phys. Rev. A*, 92:063807, Dec 2015.

[68] Henri Benisty, Aloyse Degiron, Anatole Lupu, André De Lustrac, Sébastien Chénais, Sébastien Forget, Mondher Besbes, Grégory Barbillon, Aurélien Bruyant, Sylvain Blaize, and Gilles Lérondel. Implementation of pt symmetric devices using plasmonics: principle and applications. *Opt. Express*, 19(19):18004–18019, Sep 2011.

[69] Enes Şeker, Babak Olyaeefar, Khalil Dadashi, Serdar Şengül, Mohammad Hosain Teimourpour, Ramy El-Ganainy, and Abdullah Demir. Single-mode quasi pt-symmetric laser with high power emission. *Light: Science and Applications*, 12:149, Jun 2023.

[70] A. Guo, G. J. Salamo, D. Duchesne, R. Morandotti, M. Volatier-Ravat, V. Aimez, G. A. Siviloglou, and D. N. Christodoulides. Observation of $\mathcal{PT}$-symmetry breaking in complex optical potentials. *Phys. Rev. Lett.*, 103:093902, Aug 2009.

[71] Christian E. Rüter, Konstantinos G. Makris, Ramy El-Ganainy, Demetrios N. Christodoulides, Mordechai Segev, and Detlef Kip. Observation of parity–time symmetry in optics. *Nature Physics*, 6:192–195, Jan 2010.

[72] Andrey A. Sukhorukov, Zhiyong Xu, and Yuri S. Kivshar. Nonlinear suppression of time reversals in $\mathcal{PT}$-symmetric optical couplers. *Phys. Rev. A*, 82:043818, Oct 2010.

[73] R. El-Ganainy, K. G. Makris, D. N. Christodoulides, and Ziad H. Musslimani. Theory of coupled optical $\mathcal{PT}$-symmetric structures. *Opt. Lett.*, 32(17):2632–2634, Sep 2007.

[74] Shachar Klaiman, Uwe Günther, and Nimrod Moiseyev. Visualization of branch points in $\mathcal{PT}$-symmetric waveguides. *Phys. Rev. Lett.*, 101:080402, Aug 2008.

[75] A. Govindarajan, Amarendra K. Sarma, and M. Lakshmanan. Tailoring $\mathcal{PT}$-symmetric soliton switch. *Opt. Lett.*, 44(3):663–666, Feb 2019.

[76] Y. Chen, A.W. Snyder, and D.N. Payne. Twin core nonlinear couplers with gain and loss. *IEEE Journal of Quantum Electronics*, 28(1):239–245, 1992.

[77] N. V. Alexeeva, I. V. Barashenkov, Andrey A. Sukhorukov, and Yuri S. Kivshar. Optical solitons in $\mathcal{PT}$-symmetric nonlinear couplers with gain and loss. *Phys. Rev. A*, 85:063837, Jun 2012.

[78] Yu. V. Bludov, V. V. Konotop, and B. A. Malomed. Stable dark solitons in $\mathcal{PT}$-symmetric dual-core waveguides. *Phys. Rev. A*, 87:013816, Jan 2013.

[79] Hamidreza Ramezani, Tsampikos Kottos, Ramy El-Ganainy, and Demetrios N. Christodoulides. Unidirectional nonlinear $\mathcal{PT}$-symmetric optical structures. *Phys. Rev. A*, 82:043803, Oct 2010.

[80] Ambaresh Sahoo, Dipti Kanika Mahato, A. Govindarajan, and Amarendra K. Sarma. Bistable soliton switching dynamics in a $\mathcal{PT}$-symmetric coupler with saturable nonlinearity. *Phys. Rev. A*, 105:063503, Jun 2022.

[81] Ambaresh Sahoo, Dipti Kanika Mahato, A. Govindarajan, and Amarendra K. Sarma. Switching dynamics of femtosecond solitons in parity-time-symmetric coupled optical waveguides. *Phys. Rev. A*, 106:043502, Oct 2022.

[82] X. Zhang, V. A. Vysloukh, Y. V. Kartashov, X. Chen, F. Ye, and M. R. Belić. $\mathcal{PT}$ symmetry in nonlinear twisted multicore fibers. *Opt. Lett.*, 42(15):2972–2975, Aug 2017.

[83] Ryszard Stępień, Marcin Franczyk, Dariusz Pysz, Ireneusz Kujawa, Mariusz Klimczak, and Ryszard Buczyński. Ytterbium-phosphate glass for microstructured fiber laser. *Materials*, 7(6):4723–4738, 2014.

[84] Marcin Franczyk, Dariusz Pysz, Piotr Pucko, Damian Michalik, Marek Biduś, Michał Dłubek, and Ryszard Buczyński. Yb^{3+} doped silica nanostructured core fiber laser. *Opt. Express*, 27(24):35108–35119, Nov 2019.

[85] M Franczyk, R Stepien, D Pysz, I Kujawa, and R Buczynski. Phosphate Yb^{3+} photonic crystal fiber single-mode laser with enormous high pump absorption. *Laser Physics Letters*, 11(8):085104, jun 2014.

[86] Robert Adair, L. L. Chase, and Stephen A. Payne. Nonlinear refractive index of optical crystals. *Phys. Rev. B*, 39:3337–3350, Feb 1989.

[87] Jianke Yang. *Nonlinear Waves in Integrable and Nonintegrable Systems*, chapter 7, pages 327–403.